University of Stavanger

Faculty of Science and Technology

MASTER'S THESIS

Study program: Industriell Økonomi ***Specialization(s):*** *Materials Technology and Project Management*	**Spring semester, 2015** Open access
Author: André Ruså-Lie	…… (Writer's signature)

Faculty supervisor:
Vidar Hansen

External supervisor(s) at NOMAC – Norwegian Material Center of Expertise AS:
Håkon Jørgensen
Technical Manager/Chief Metallurgist

Odd Reidar Barka
Materials Engineer

NOMAC

Thesis title:

The effects of varying soaking times at two hardening temperatures on material properties and morphology for the martensitic ferritic steel S165M

Credits (ECTS): 30

Key words/tags: S165M, w. nr. 1.4418, martensitic ferritic stainless steel, hardening, quenching, tempering, material properties, morphology, tensile stress, hardness, impact energy, SEM, EDS, EBSD	**Pages:** 74 **+ Appendix:** 29 **Stavanger, 11.06.2015**

This page has intentionally been left blank

Abstract

The purpose of the thesis was to examine if the material properties and/or the morphology of a martensitic ferritic stainless steel were altered if exposed to varying soaking times at two distinct hardening temperatures. The background for the thesis was the need to analyze and verify the optimality of the hardening processes currently performed at NOMAC – Norwegian Material Center of Expertise AS. The analyzed steel was hot-forged S165M (W. nr. 1.4418, X4CrNiMo 16-5-1). The two hardening temperatures were 1000 °C and 1030 °C. The soaking times analyzed were 1, 2, 5, 10 and 20 hours, for both temperatures. Both as-quenched and tempered samples were examined.

Standardized mechanical testing was performed, and included tensile stress testing, hardness Vickers testing and Charpy-V impact testing. The mechanical properties remained statistically consistent. Neither the as-quenched nor the tempered samples showed any indication that the soaking times directly altered said properties. The two different temperatures produced statistically equivalent results. The majority of the observed differences in properties between as-quenched and tempered samples were as expected. The gathered impact energy values did not differentiate between as-quenched/tempered samples, leading to a debate regarding their validity. The general conclusion is that the mechanical properties are not correlated with longer/shorter soaking times.

The material morphology was analyzed using optical light microscopy, and SEM (including EDS and EBSD analysis). The use of different temperatures had little to no effect on the final microstructure. Morphologically, the material experienced substantial changes when exposed to longer soaking times. Longer soaking times introduced the growth of the average martensitic (i.e. prior austenitic) grain diameters, where the growth exceeded 80 % after a soaking time of 20 hours. The longer soaking times also caused a reduced ferrite fraction for samples hardened at 1000 °C (the fraction of ferrite was 0.19 in sample soaked for 1 hour, 0.11 in samples soaked for 20 hours). This caused a subsequent increase in the martensite fraction. The general ferritic grain shapes were also affected with longer soaking times, transforming from lacy/vermicular grain shapes into globular grains. With regards to material properties, several of these changes counteract each other. It is therefore believed that the combination of the martensitic grain growth and the reduction of ferrite content yields approximately constant mechanical properties. How these morphological changes alter the mechanical properties when occurring individually is not examined.

The results of the thesis indicate that S165M is a remarkably resistant alloy, producing consistent qualities regardless of the soaking time and/or the hardening temperature.

This page has intentionally been left blank

Acknowledgements

This thesis is a result of my specialization in Materials Technology, in relation to my M.Sc. in Industrial Economics (Industriell Økonomi, INDØK) at the University of Stavanger during the spring of 2015. The idea of the thesis was first developed by Technical Manager/Chief Metallurgist Håkon Jørgensen and Materials Engineer Odd Reidar Barka, both from NOMAC – Norwegian Material Center of Expertise AS.

There are several people I would like to thank for their help and insight with my thesis. I would like to direct thanks to Håkon Jørgensen and Odd Reidar Barka for highly constructive and knowledgeable input in relation to my results discussion. I would also like to thank my faculty advisor, Professor Vidar Hansen at the Institute of Construction and Materials Technology at the University of Stavanger. My SEM results could not have been put forth without the help of Ingunn Cecilie Oddsen, Senior engineer at the ICMT Laboratory. I would also like to thank Senior Engineer Ahmad Yaaseen Amith, Department engineers Tor Gulliksen and Jan Magne Nygård for their help using equipment in the workshop.

In the end I would like to dedicate a special thanks to my wife, Charlotte, who has shown me a tremendous amount of support. Never underestimate the power of encouragement.

"Any fool can know. The point is to understand."

- Albert Einstein

André Ruså-Lie

Stavanger, June 2015

This page has intentionally been left blank

Table of Contents

Symbols and abbreviations

Symbols	Translation	Meaning of symbol in thesis
α	Alpha	Ferrite (α-iron)
β	Beta	Ferrite (β-iron)
γ	Gamma	Austenite (γ-iron)
δ	Delta	Ferrite (δ-ferrite/ δ-iron)
π	Pi	i.e. mathematical constant 3.1415
σ	Sigma	i.e. standard deviation

Abbreviations

BCC	Body Centered Cubic (i.e. lattice structure)
BCT	Body Centered Tetragonal (i.e. lattice structure)
CNC	Computer Numerical Control
E	Young's modulus of elasticity (Elastic modulus)
EBSD	Electron Backscatter Diffraction
EDS	Energy-dispersive X-ray Spectroscopy
FCC	Face Centered Cubic (i.e. lattice structure)
$HV_{10\ kg}$	Hardness Vickers with applied load of 10 kg
HB	Hardness Brinell
J	Joule [kgm/s^2]
M_S	Martensite start temperature
M_F	Martensite finish temperature
OES	Optical Emission Spectroscopy
Pa	Pascal, [N/m^2]
SEM	Scanning Electron Microscope

SI prefixes/suffixes

n	Nano, 10^{-9}
µ	Micro, 10^{-6}
m	Milli, 10^{-3}
k	Kilo, 10^{3}
M	Mega, 10^{6}
G	Giga, 10^{9}

List of Tables

List of Figures

List of Formulas

This page has intentionally been left blank

1. Introduction

Norwegian Material Center of Expertise AS (NOMAC), formerly known as Scana Steel Stavanger AS, is a steel mill focusing on high alloyed forgings as well as low- and high-alloyed castings. The plant is located in Jørpeland, and has been an integral part of the community for over 100 years. High demands are set in terms of production execution, product documentation and quality.

S165M (W. nr. 1.4418, X4CrNiMo 16-5-1) is one of the stainless steel alloys produced at NOMAC. It is a martensitic ferritic stainless steel, with excellent mechanical properties. Due to the high material strength and toughness, it is often used for the manufacturing of propellers, bolts and shafts. The steel displays excellent qualities and properties even at low temperatures. The weldability is good, due to the low carbon content.

The alloy is – due to its martensitic structure – hardened and tempered before being manufactured into products or components. S165M is normally soaked at its hardening temperature (i.e. 1000 °C) for 1 hour, once a stable core temperature is reached. For NOMAC, this duration is not always the most feasible alternative due to logistics, and the alloy is therefore often hardened for longer durations. In addition, the choice of 1000 °C as the standard hardening temperature is based on empirical data. Its validity as the optimal hardening temperature has been brought into question.

NOMAC wished to examine if the alloy is subject to mechanical and morphological changes if the soaking time at two hardening temperatures varied from the normally used 1 hour at 1000 °C. The different soaking times examined in this thesis were 1, 2, 5, 10 and 20 hours. The hardening temperatures examined were 1000 °C and 1030 °C. Thus, the thesis question is summarized as:

How does a variation in soaking time at two different hardening temperatures affect the mechanical properties and morphology for the martensitic, ferritic stainless steel S165M?

The thesis is clearly structured. There are separate sections for relevant theory, experimental methods, results, relevant discussion and conclusion. Sub-sections are applied where a more detailed description is necessary to fully enlighten the subject at hand.

2. Background theory

2.1 Characteristics of common stainless steels

Stainless steels have a wide array of applicable uses, from kitchenware such as knives, to structural components in corrosive environments. What separates stainless steels from common carbon steels is the formation of a chromium oxide layer on the material surface. This chromium oxide layer is a result of the chromium content in the alloy, which needs to be equal to or above 10.5 wt% in order to classify the steel as stainless (Callister & Rethwisch, 2011). The oxide layer is self-repairing, and prevents diffusion of oxygen to the surface of the steel – thus protecting from corrosion.

However, stainless steels are not resistant to all forms of corrosion in all environments. The corrosion resistance of stainless steel will not be reduced if the material is subject to damage, deflection or deformation. The diffusion of oxygen is reduced even during high degrees of plastic deformation. However, the chromium oxide layer does not alter the diffusion rate of chloride ions. Thus, stainless steels are susceptible to corrosion in chloride-rich environments (Bhadeshia & Honeycombe, 2006).

Examples of stainless steels include (but is not limited to) martensitic stainless steels, ferritic stainless steels, austenitic stainless steels and steels with a duplex structure (i.e. austenite and ferrite). Table 2.1 illustrates the common alloy element concentration intervals for typical stainless steel allotropes (in wt%). Combinations of these allotropes can be achieved by altering the chemical composition.

Table 2.1 – Concentration of alloy elements in common stainless steel allotropes

(Davis, J. R.; A.I.H. Committee, 1994)

Alloy type	C	Mn	Si	P	Cr	Ni	Mo	Others
Martensitic	0.10 - 1.10	1.0 – 1.25	0.50 – 1.00	0.04 – 0.06	11.0 – 18.0	0.00 – 2.50	0.00 – 0.75	Cu, N, S, V
Austenitic	0.03 – 0.15	2.0 – 19.0	1.00 – 4.50	0.06 – 0.20	16.0 – 21.0	3.50 – 38.0	0.00 – 4.00	Cu, N, Nb, S, Ti
Ferritic	0.08 – 0.20	1.00 – 2.50	1.00	0.04 – 0.06	10.5 – 27.0	0.00 – 1.00	0.00 – 2.50	Cu, N
Duplex	0.03 – 0.20	1.00 – 2.00	0.60 – 1.00	0.03 – 0.04	21.0 – 29.0	4.50 – 6.50	1.00 – 4.00	Al, B, Cu, N, V, W

2.2 Phase-estimations in S165M during and after solidification

The certificate for charge A19606 specifies the chemical composition of the delivered material (see Appendix B). The measured composition, along with the minimum and maximum allowable values, is presented in Table 2.2 below. The alloy element limits are found in the datasheet (see Appendix A). All values are in wt%.

Table 2.2 – Alloying limits of S165M and true chemical composition of charge A19606

	Alloy element								
	C	**Si**	**Mn**	**S**	**P**	**Cr**	**Ni**	**Mo**	**N**
Min. allowable value	-	-	-	-	-	*15.00*	*4.50*	*0.80*	*0.020*
True composition	**0.037**	**0.40**	**0.60**	**0.0001**	**0.024**	**16.11**	**4.94**	**0.97**	**0.033**
Max. allowable value	*0.050*	*1.00*	*1.50*	*0.025*	*0.035*	*17.00*	*6.00*	*1.50*	-

2.2.1 Schaeffler-diagram

In order to estimate the phases present in a steel alloy, one can utilize a Schaeffler-diagram. Such a diagram utilizes the concentration of alloy elements in order to estimate the phases present in the material. The Schaeffler-diagram was originally developed in order to analyze welds and weld beads. Therefore, the diagram attempts to describe the microstructure after melting and rapid cooling, i.e. equivalent to hardening and quenching (Callister & Rethwisch, 2011).

By using a standardized set of equations, one calculates the coordinates of the material in the corresponding diagram. These coordinates are referred to as nickel- and chrome-equivalents (Ni_{eq} and Cr_{eq}), respectively (Callister & Rethwisch, 2011):

$$Ni_{eq} = Ni + 30 \cdot C + 0.5 \cdot Mn \qquad \textbf{(1) } \mathbf{Ni_{Eq}}$$

$$Cr_{eq} = Cr + Mo + 1.5 \cdot Si + 0.5 \cdot Nb \qquad \textbf{(2) } \mathbf{Cr_{Eq}}$$

By utilizing the chemical composition presented of charge A19606 of S165M in Table 2.2, the coordinates can be calculated. From there, the diagram illustrates an estimate of the present phases.

Thus, using formulas (1) and (2)

$$Ni_{eq} = 4.94 + 30 \cdot 0.037 + 0.5 \cdot 0.60 = \mathbf{6.35}$$

$$Cr_{eq} = 16.11 + 0.97 + 1.5 \cdot 0.40 + 0.5 \cdot 0 = \mathbf{17.68}$$

When plotted in a Schaeffler-diagram, you obtain results as shown in Figure 2.1 below.

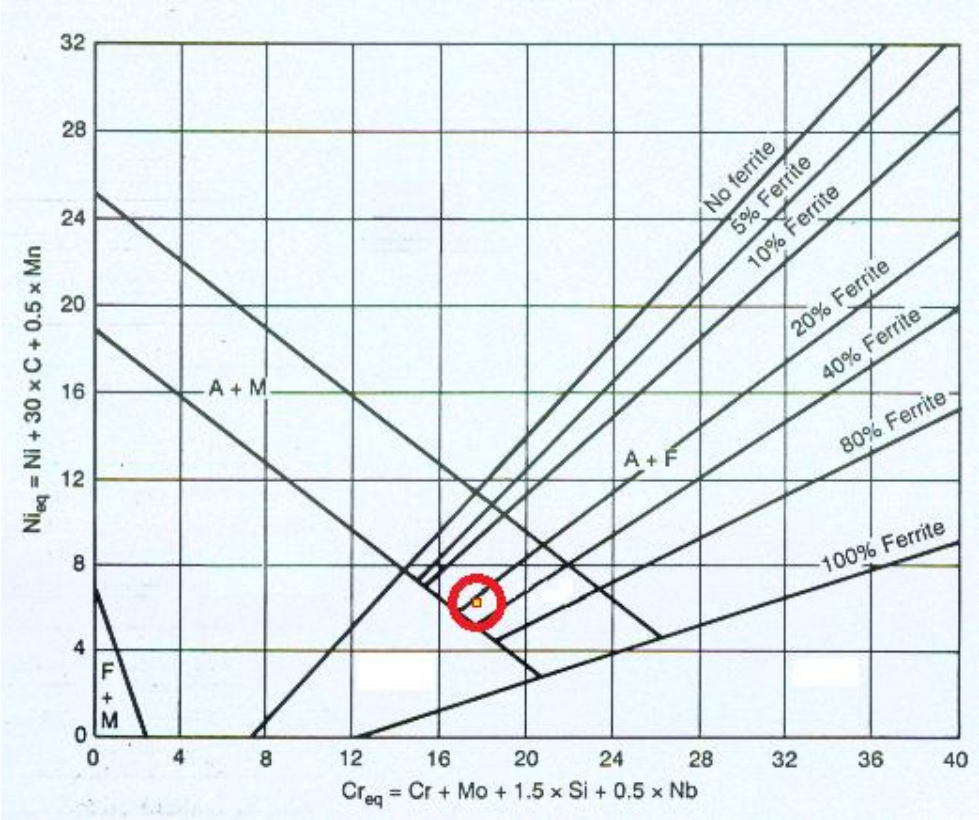

Figure 2.1 – Schaeffler diagram, with estimation of final microstructure (center of red circle) (Davis, J. R.; A.I.H. Committee, 1994)

From Figure 2.1, one can see that charge A19606 of S165M – given the chemical composition from the certificate – is estimated to be located in the austenitic + martensitic + ferritic region, with approximately 20 % ferrite. The austenite present in as-quenched samples is suspected to be retained austenite. The austenite in tempered steel is suspected to be primarily reversed austenite. This is due to the hardenability of the material, and theory describing the formation of reversed austenite during tempering of martensitic steels (Song, Rong, & Li, 2011). The presence and morphology of austenite in this material will be further analyzed through the use of EBSD, the principles of which are described in more detail in section 2.6.2.

2.2.2 Thermo-Calc computations (phase diagram and Scheil-Gulliver solidification simulation)

Using software such as Thermo-Calc, one can calculate estimations of phase diagrams using computational thermodynamics and diffusion-controlled simulations. As always, when evaluating phase diagrams, it is important to note that the diagrams are based on equilibrium reactions – i.e. extremely slow heating and/or cooling reactions. Since such reactions rarely occur in practice, one can never make draw definite conclusions of a material structure based on phase diagrams alone.

Figure 2.2 shows an excerpt of a phase diagram, calculated at NOMAC using Thermo-Calc. The basis for the calculation was the given chemical composition of charge A19606. In equilibrium, S165M is fully in its liquid phase when exposed to temperatures above ~1480 °C. Once solidification begins, the BCC-structured phase δ-ferrite starts to form. At approximately 1400 °C, the structure is fully ferritic. This structure is maintained until 1350 °C, where the material experiences a transformation into austenite at the expense of the ferritic phase. At approximately 1100 °C, the structure is fully austenitic, and remains as such until re-ferritization at ~775 °C. The pink line in the diagram is related to M23C6 carbides. However, these are not believed to actually form until very high soaking times are used.

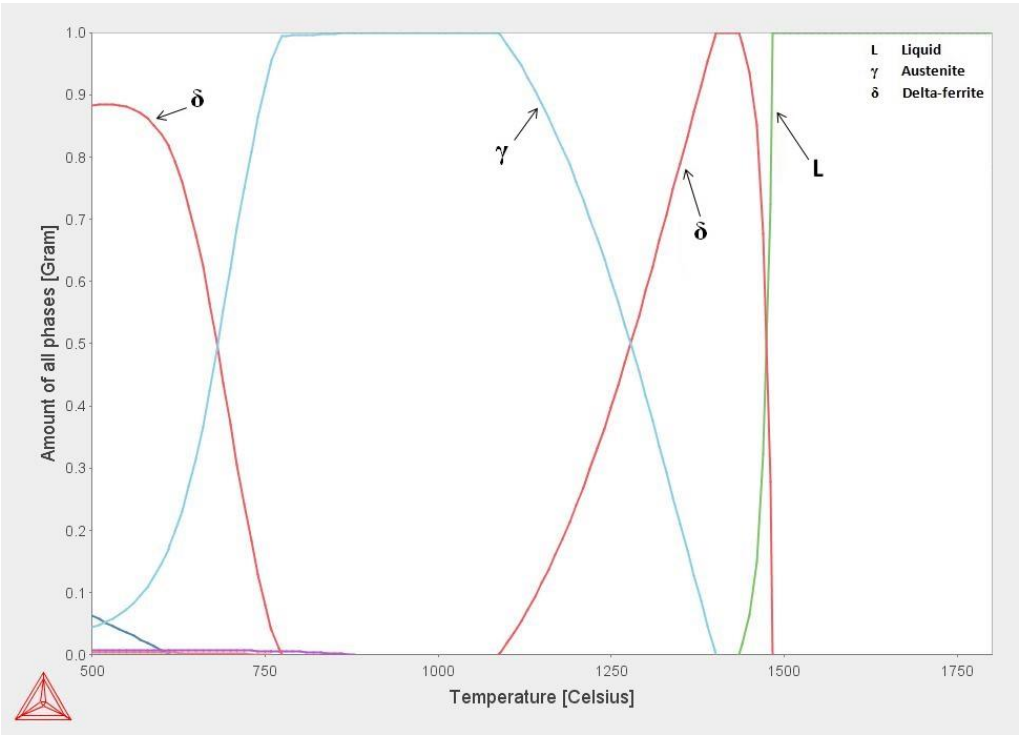

Figure 2.2 – Phase diagram, calculated using Thermo-Calc software (NOMAC v/ Håkon Jørgensen, 2015)

Phase diagrams are accurate at predicting microstructure if the cooling rate is low enough to maintain the principle of equilibrium, i.e. ensuring a slow cooling to enable all diffusion and transformation processes to complete fully. In practice, however, equilibrium is rarely maintained. The field of solidification is vast and complex, and includes several different mathematical and metallurgical models and hypotheses. These are not covered in detail in this thesis, with the exclusion of the Scheil diagram. When a material experiences a transition from liquid to solid states, the morphology that forms the basis for the material is established. One can use the Scheil-Gulliver equation (or Scheil equation) in order to describe the solute redistribution during the solidification of an alloy (Porter & Easterling, 1992). The resulting Scheil diagram takes many factors into account – incl. diffusion and segregation processes – and visually indicates the resulting microstructure that is formed when crossing from a fully liquid to a fully solid state (Scheil, 1942). The diagram is more reliable than a phase diagram. Figure 2.3 shows the Scheil-diagram for S165M, computed by NOMAC.

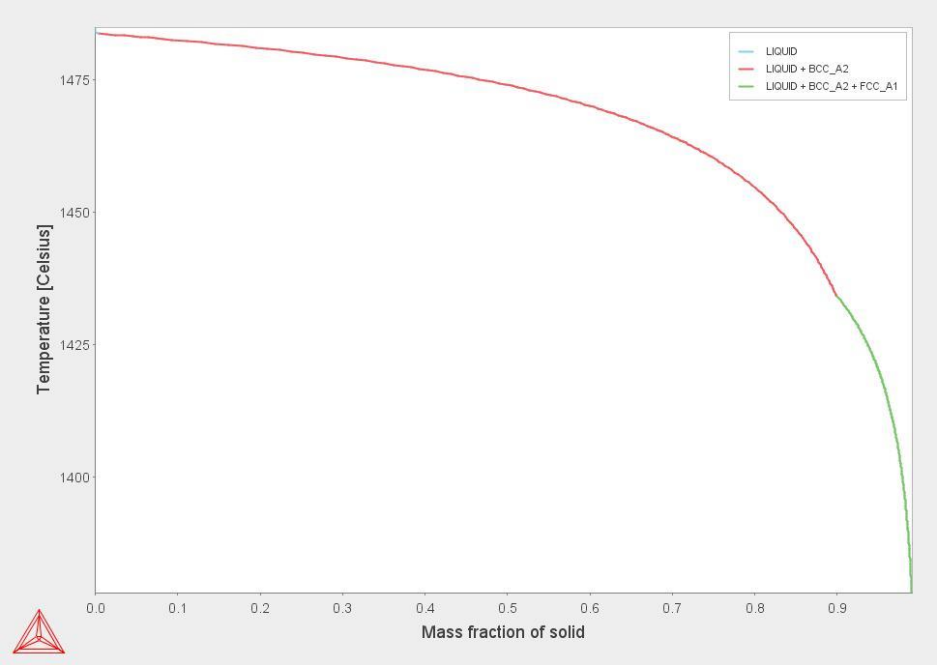

Figure 2.3 – Scheil diagram of S165M solidification (NOMAC, 2015)

The software yields equal diagram with or without diffusion in the solid phase. The Scheil diagram illustrates that the first 0.9 mass fraction of formed solid is pure δ-ferrite. The final 0.1 mass fraction before full solidification is a mix of δ-ferrite and austenite. The usual microstructure of S165M contains substantially smaller ferrite fractions. It is therefore believed that the solid phase cooling time is sufficient to establish quasi-equilibrium, thus transforming the solidified ferrite into austenite. Once cooled even further, below M_S, the austenite transforms into martensite. The resulting final microstructure is primarily martensitic, with varying levels of δ-ferrite.

2.2.3 Ferrite (α-iron)

Ferrite is an allotrope of iron, with a BCC (**B**ody **C**entered **C**ubic) lattice structure. See Figure 2.4 for an illustration of a BCC unit cell. The presence of this crystalline structure is what yields the magnetic properties found in steels and cast iron. It is thus a classic example of a ferromagnetic material.

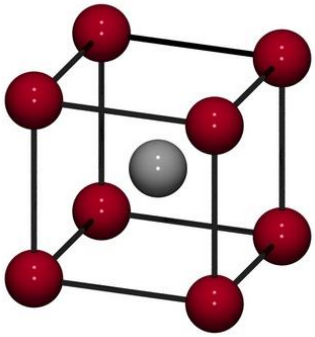

Figure 2.4 – BCC (Body Centered Cubic) unit cell (Callister & Rethwisch, 2011)

All Fe-C alloys will contain some amount of ferrite, given that the material is allowed to stabilize at room-temperature. In the pure Fe-C alloy, ferrite is a stable phase below 910 °C. Above this temperature, a different iron allotrope – austenite, see section 2.2.4 – is stable. For alloys with a carbon content of 0.68 wt% and below, one can in theory differentiate between α-iron and β-iron at the Curie temperature of 771 °C, where β-iron exists between the Curie temperature and 910 °C. Although α- and β-iron theoretically are distinct phases, the term β-iron is seldom used, due to their identical crystallography and contiguous phase fields (Callister & Rethwisch, 2011).

Carbon has a low solubility in α-iron, where the maximum solubility is approximately 0.02 wt% at 723 °C, and 0.005 wt% at 0 °C. The poor solubility is due to the fact that carbon dissolves interstitially in iron. The interstitial space in a BCC unit cell is approximately half of the carbon atom diameter. This causes a strong local strain field localized to the interstitial placement of the carbon atom. Carbon is more soluble at higher temperatures, due to the occurrence of lattice parameter expansion – i.e. expansion in width, length and height – during heat exposure to the material. This creates more room for interstitially dissolved carbon. The material properties for pure ferrite are varied, although these values normally are inferior to those of pure martensitic steels. Ferritic stainless steels are more sensitive to crack formation at lower temperatures, thus proving to be an unfavorable choice for structures exposed to cold climates (Bhadeshia & Honeycombe, 2006).

2.2.4 Austenite (γ-iron)

Austenite is a non-magnetic allotrope of iron. The lattice structure is a configuration of FCC (**F**ace **C**entered **C**ubic) unit cells. See Figure 2.5 for an illustration of an FCC unit cell. In plain carbon steels, austenite is stable between the eutectoid temperature of 738 °C and 1495 °C. Some variations occur as a result of carbon concentration in the alloy (Bhadeshia & Honeycombe, 2006).

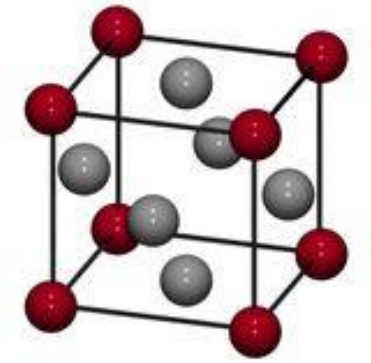

Figure 2.5 – FCC (Face Centered Cubic) unit cell (Callister & Rethwisch, 2011)

Austenite, like ferrite, is a soft and ductile iron allotrope. However, the solubility of carbon is far greater in austenite – up to 2.04 wt% at 1146 °C. This is due to the increased interstitial space found in the FCC unit cell, compared to the BCC unit cell (Callister & Rethwisch, 2011).

As austenite slowly cools from the eutectoid temperature of 738 °C, it often transforms into a mixture of ferrite and cementite as the carbon diffuses from the lattice structure. Depending on the alloy composition and rate of cooling, pearlite may also form. The prerequisite for these transformations is an incremental lowering of the temperature, ensuring equilibrium. If the stable austenite is exposed to a very rapid rate of cooling, the lattice structure may experience a severe distortion. This distortion will induce strains, causing formation of the far harder phase martensite. The formation of martensite is not an equilibrium reaction, and is covered in more detail in section 2.4.

2.2.5 Martensite

Martensite refers normally to the very hard crystalline structure where the lattice structure consists of BCT (**B**ody **C**entered **T**etragonal) unit cells. See Figure 2.6 for an illustration of how two adjacent FCC-cells transform into the martensitic BCT-structure. Martensite is not found on traditional phase diagrams, as it is a metastable phase, i.e. not stable at an equilibrium.

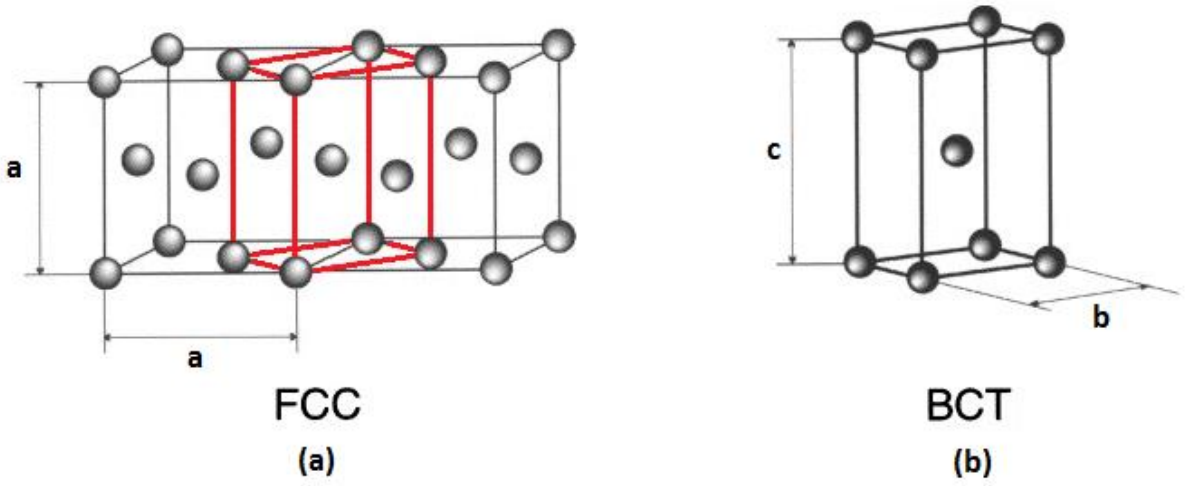

Figure 2.6 – (a) Adjacent FCC-cells; (b) the resulting BCT unit cell. Modeled after (Ahlers, 2004)

Depending on the alloy carbon content, the crystal grain structure of martensite is lath- or plate-shaped. The lath/plates stretch and cover the full area restricted by the pre-transformatic austenite grain boundaries. When the microstructure of a martensitic steel is viewed in a light-microscope, the structure is often incorrectly described as acicular, i.e. needle shaped. The acicular description stems from viewing a cross-section of very thin plates in tight formation. The resulting BCT cell is transformed from the adjacent FCC-cells, where the resulting highest lattice parameter is denoted c. The actual difference from the original FCC-parameter a is varying, but c is always > a.

Martensitic steels have been known to achieve hardness values up to 700 HB. As-quenched martensite tends to be very brittle. Tempering of martensitic alloys increase the toughness, while the hardness is somewhat decreased. Martensite forms when austenite is cooled at a rate too fast to form phases stable at equilibrium. The processes of martensitic transformation and tempering of martensite are intricate and complex, and is therefore described separately in more detail in sections 2.4 and 2.5.4.

2.2.6 δ-ferrite (δ-iron)

In traditional Fe-C alloys with a carbon content below approx. 0.10 wt%, δ-ferrite is the most stable iron allotrope from the temperature region 1390 °C up to the melting point of 1539 °C. Without the addition of other alloy elements, δ-ferrite is only present in a very small partition of the Fe-C phase diagram (see Figure 2.7).

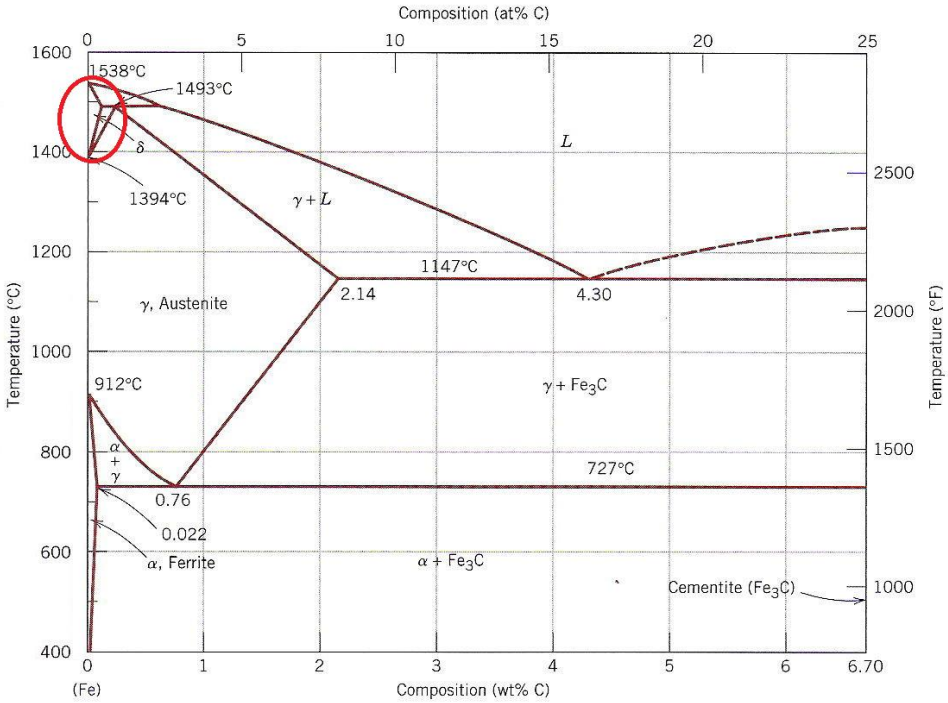

Figure 2.7 – Traditional Fe-C phase diagram, with the only occurrence of δ-ferrite circled in red (Callister & Rethwisch, 2011)

Morphologically, it is very difficult to differentiate between ordinary ferrite (α-ferrite) and δ-ferrite. They both exhibit a BCC-structure, and there are no known analysis techniques that have proven to display a morphological difference between the two. δ-ferrite has proven to be more susceptible to carbon saturation. Thus, it is implied that the two phases have a distinct chemical difference. This carbon saturation has proven to increase the relative global hardness of materials where the δ-ferrite content exceeds approx. 15 % (Wang, et al., 2014). It is worth to mention that no standardized benchmark formally differentiating the two phases on a chemical level has been internationally acknowledged. Metallurgists and material engineers at NOMAC validate that the ferrite present in S165M is primarily δ-ferritic.

2.3 The effects of alloying elements

Added alloying elements affect both the thermodynamic and the kinetic (i.e. mechanical) properties of steels. Due to the sheer magnitude of alloying elements available and utilized, this section will focus on explaining the resulting addition effects from the elements commonly found in S165M: carbon, chromium, nickel, manganese, silicon and molybdenum. In commercially available alloy steels, which are multicomponent systems, alloying elements can be found (i) in their free states; (ii) as intermetallic compounds with iron or each other; (iii) as oxides, sulphides and other non-metallic inclusions; (iv) in the form of carbides; or (v) as a solid solution in iron (Maalekian, 2007).

Carbon is the main alloying element in steels. The addition of carbon is done to ensure strengthening, as it prevents slip between the Fe-atoms in the lattice structure. Large additions of carbon to an alloy may have negative effects on the ductility and weldability of an material.

Chromium is the main alloying element in a stainless steel. This is due to the chromium-oxide layer produced by adding amounts equal to or above 10.5 wt% chromium to an alloy. Chromium is also added to enhance the hardenability of steels, and very hardenable steels are often found to have a high chromium content.

Nickel is a strong austenite former, thus ensuring that alloys with high levels often results in martensitic structures after quenching. Generally, the addition of nickel improves the properties of steels at low temperatures. A very high nickel content often suppresses the ferrite to such a degree that only austenite is formed. It is also an oxide-layer stabilizer, and is commonly found in stainless steels, along with *molybdenum*.

Silicon is primarily a ferrite former, and has to a degree a hardening effect. Along with *manganese*, it is often found in steels as remnants of the production process.

The combinations and quantities of alloying elements may produce other effects than what was intended. Several studies have been conducted in order to form a general baseline for the effects of alloy element combinations. For example, a level balance of carbide forming elements (i.e. Cr) and non-carbide forming elements (i.e. Ni) may produce microstructures with high amounts of precipitates, causing embrittlement (Maalekian, 2007). The optimal combination of element is often concluded on empirically.

2.4 Martensitic transformation in steels

The process of martensitic transformation is diffusionless, and such a transformation may also go by the names of *shear* or *displacive transformation*. Simplifications of the martensitic transformation theory are found in the curriculum of common materials courses. The general theory expands upon the premise that austenite rapidly cooled from higher temperatures experiences an unexpected structure rigidity. Carbon atoms are locked in their interstitial lattice positions, and the increase of strain energy in the structure aids in the increase of material hardness and toughness (Callister & Rethwisch, 2011). As elegant as it may be, such an explanation is too simplified to fully explain the kinetics of the transformation of austenite (FCC) into martensite (BCT).

The formation of martensite involves a complex and highly coordinated re-orientation of atoms in the lattice structure. Because austenite and martensite are intimately related phases, the martensitic transformation that occurs leads to an orientation relationship between the parent lattice and the product lattice, which is reproducible. The general transformation reaction is found to be virtually independent of any time factor. This is mathematically illustrated in the Koistinen and Marburger equation, shown below (Bhadeshia H. K., 2002):

(3) Martensite fraction $V_{\alpha'}$

$$1 - V_{\alpha'} = exp\{\beta(M_S - T)\} \qquad where \qquad \beta \cong -0.011$$

$V_{\alpha'}$ is the fraction of formed martensite, and T is a temperature equal to or below M_S, the martensite-start temperature. Note that time does not feature in this equation. This implies that the fraction of formed martensite is only dependent on the amount of undercooling that occurs below M_S. The time interval where the rapid nucleation and growth occurs is so small, that it can be viewed as negligible.

As illustrated in Figure 2.6, adjacent FCC unit cells forms the foundation of the martensite lattice, which has a morphologic consistency with BCT unit cells. The pattern in which the atoms in the parent crystal are arranged – i.e. FCC – is deformed through strain into that appropriate for martensite. The crystal experiencing deformation undergoes a corresponding macroscopic shape change. In the α'/γ (martensite/austenite) interface, we find the dislocations responsible for said

deformation. Here, there are Burgers vectors[1], so that the material experiences the change in crystal structure in addition to the deformation (Bhadeshia & Honeycombe, 2006). The transformation of austenite to martensite is a process that is dependent on the coherency in the transformation interface. The shape-change results in an invariant-line strain, where one line in the transformation interface is unrotated and undistorted.

Although the invariant-line strain is necessary to deform the general crystal structure, it is not solely responsible for the change in lattice structure from FCC to BCT. An alternative strain was originally proposed by Bain in 1924. Such a strain helps alter the lattice parameters, and is known as *Bain Strain* (Bhadeshia H. K., 2002).

Assume that two FCC-cells are adjacent; see Figure 2.6. Assume the lattice parameters are parallel to coordinate axes XYZ. During transformation into martensite, the adjacent FCC-cells combine into one BCT cell. In this scenario, the newly formed unit cell experiences a dynamic expansion along the Z-axis. The X- and Y-axises experience no expansion. The deformation describing this Bain Strain is thus given by the following expression, found in (Bhadeshia H. K., 2002):

(4) Bain Strain

$$B = \begin{pmatrix} \epsilon_X & 0 & 0 \\ 0 & \epsilon_Y & 0 \\ 0 & 0 & \epsilon_Z \end{pmatrix} \qquad where \qquad \begin{matrix} \epsilon_X = \epsilon_Y = 0 \\ \epsilon_Z > 0 \end{matrix}$$

This is only valid for this orientation of the parent crystal structure. Another orientation may yield uniaxial deformation along the other two axises. This phenomenon is what makes it difficult to differentiate between BCC and BCT using electron backscatter diffraction, since the lattice distortion seems to be of a variable nature. This yields a tight structure with BCT cells oriented randomly relative to each other. The result is a structure where the BCT cells are oriented in a seemingly random order, causing a global semi-equality with BCC cells. The implication this may have on crystallographic analysis is covered in section 2.6.2.

[1] From physics, a *Burgers vector* – often denoted **b** – is a vector that represents the magnitude and the direction of a lattice distortion resulting from a dislocation in a crystal lattice (Callister & Rethwisch, 2011)

2.5 Heat treatment of metallic alloys

Heat treatment is a collective term, covering industrial and metalworking processes. The goal of said processes is to alter the physical – and often even chemical – properties of a material. Metallurgy is the field where heat treatments are most commonly used, due to the versatility and obtainable results yielded by the process.

What type of heat treatment to utilize depends on what abilities one wants the treated material to exhibit. Processes such as hardening and quenching increases material hardness, while tempering increases ductility (ASM International, 2006). It is worth noting that while several industrial metalworking processes generate heat, the term *heat treatment* is reserved for those processes that intentionally heat and cool materials in order to alter its properties. This section only covers heat treatment processes relevant for S165M, i.e. forging, hardening and quenching, and tempering.

2.5.1 Forging

Forging is a manufacturing process, and is utilized for metallic materials. In the forging process, the material is shaped using localized compressive forces. The material may be forged in a hot or cold state, and is thus classified as hot- or cold-forged, respectively. Iron and steel are almost exclusively hot-forged. Forging is a process that has existed for millennia, and was traditionally used for kitchenware, tools and blade weapons. During the Industrial Revolution, it became more common to utilize forging when manufacturing components or mechanisms that needed a high level of strength.

The main advantage of forging is the production of a component that is stronger than when compared to an equivalent cast or machined part. When a part is forged, the internal grain structure deforms. The new grain structure becomes continuous, and follows the general shape of the part. Due to this continuous structure, the component normally exhibits improved material characteristics and strength. This continuous flow is not present in cast and/or machined parts (Callister & Rethwisch, 2011). See Figure 2.8 for an illustration of the grain structure in differently manufactured components.

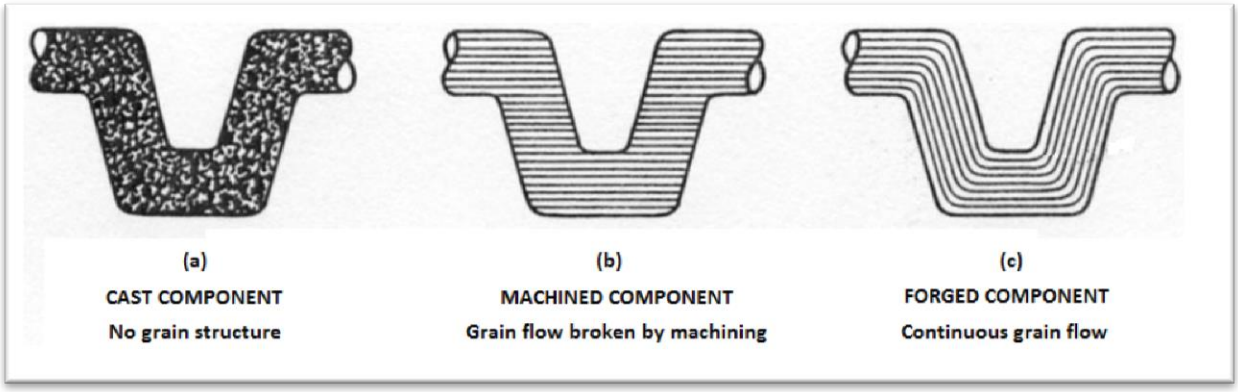

Figure 2.8 – Grain flow in (a) cast component; (b) machined component; and (c) forged component, courtesy of (SIFCO, 2012)

The material utilized in this thesis is hot-forged. Hot-forging is normally chosen for steels, as it diminishes – or completely eliminates – the presence of work-hardening that may arise in the cold-forging process. Most forging operations use metal-forming dies, which must fulfill a great number of characteristics. This includes being able to withstand the forging temperature, and changes to its shape due to the received residual thermal energy from the forged material.

2.5.2 Hardening and quenching

Hardening is a physical-chemical process where the intention is to increase the hardness of a material. Other mechanical properties, such as yield strength/tensile strength are normally increased as well. The general process of hardening consists of two primary phases (ASM International, 2006):

1. The material is slowly heated above its critical temperature, normally causing austenitizing of the steel. Said material is normally held for a sufficient amount of time, allowing precipitations to dissolve
2. The material temperature is rapidly lowered, usually by quenching it in water and/or oil

The rapid temperature decrease causes carbon atoms to be locked in interstitial positions in the lattice structure. As previously shown, this process causes martensite to form. The hardness – i.e. the material's ability to resist plastic deformation – increases during this process (Bhadeshia & Honeycombe, 2006). Pure hardened steels are – while very hard – normally too brittle. Therefore, hardened steels are normally tempered before used for commercial purposes. See section 2.5.3 for a general introduction to the tempering process.

2.5.3 Tempering – General introduction

Tempering is the process where a material is re-heated after hardening and quenching. The temperature used in this process is normally far below the critical temperature. The goal is not to repeat the hardening process, but to relieve stresses in the lattice structure, while simultaneously increasing the toughness and ductility of the material in question (Callister & Rethwisch, 2011). The tempering process will normally decrease the hardness of the material. Tempering usually consists of heating the material to a specified temperature, holding it at said temperature for a specified amount of time, and allowing it to fully cool in air to ambient temperature. The exact temperature used determines the resulting decrease in hardness, and depends on the desired properties of the finished product. As an example, machining tools are usually tempered at very low temperatures, while springs are tempered at much higher temperatures (Hibbeler, 2008).

It is empirically proven that the tempering temperature and the duration of the tempering process have direct effects on mechanical properties such as hardness. First described in 1945, the most statistically proven relation between tempering temperature and resulting effects is known as the Hollomon-Jaffe Parameter (Hollomon & Jaffe, 1947):

(5) Hollomon-Jaffe parameter

$$H_p = \frac{T \cdot [c + \log(t)]}{1000}$$

where T = Temperature in Kelvin, c = Constant depending on alloy composition and t = tempering time in hours

The material utilized in this thesis has a composition yielding a constant equal to c = 19.8 (Shlyakman, Tampolskii, & Ratushev, 2010). Thus for a tempering temperature of 560 °C over 8 hours – parameters which are not varied throughout this thesis – the Hollomon-Jaffe parameter equals 17.25. An alteration of these parameters could yield far different material properties. Note that the tempering temperature has a more substantial impact than the time parameter.

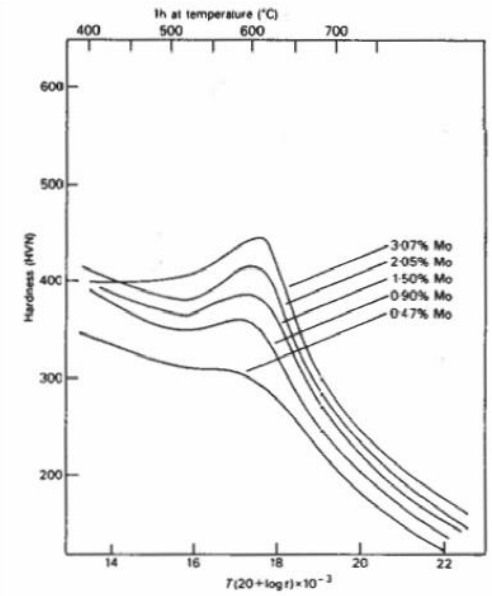

Figure 2.9 - The effect of tempering temperature and time on the hardness values (HV) of as-quenched 0.1 wt% steel (Irving & Pickering, 1960)

2.5.4 Tempering of martensite

As shown, martensite in steels can be very hard, but at the same time very brittle. It is therefore often necessary to temper the martensite, in order improve its usability in structural and mechanical components. Tempered martensite provides one of the best combinations of strength and toughness obtainable in low carbon steels. The tempering process allows the microstructure to move incrementally towards an equilibrium, under the influence of thermal activation. Thus, the tempering ability of a material depends on the distance the microstructure has from its equilibrium state.

Certain structures contain higher levers of stored free energy than others do. For example, for a typical alloy steel with a composition of Fe-0.2C-1.5Mn wt%, the reference (zero energy) state contains an equilibrium mix of ferrite, graphite and cementite. With a very miniscule increase in stored energy (70 J mol^{-1}), the graphite is no longer present. The alloy steel has a phase mixture consisting of supersaturated ferrite at 1414 J mol^{-1}, and pure martensite at 1714 J mol^{-1}. Tempering a pure martensitic steel with said alloy composition can thus eventually alter the microstructure by releasing the free energy stored in it (Bhadeshia & Honeycombe, 2006).

For pure martensitic steels, the tempering of martensite normally includes the diffusion of interstitially locked carbon. However, the substitutional solutes do not diffuse during this stage. If held at the tempering temperature for a sufficient amount of time, the structure can evolve into a dispersion of coarse carbides in a ferritic matrix, which bears little resemblance to the original martensitic structure. For martensitic ferritic steels, however, the quenching process yields a fully martensitic/ferritic structure. There is no indication that tempering induces the development of further ferritic content, or cementite. If tempering at temperatures above 550 °C, one can expect to see a development of austenite, finely dispersed in the martensitic structure (Song, Rong, & Li, 2011). This austenite is commonly referred to as reversed austenite, as it reverts to its pre-quenched form due to the reception of thermal energy. The effect this reversed austenite has on mechanical properties is proportional with ΔT (where ΔT is the difference in temperature between 550 °C and the actual temperature used in the tempering process).

2.6 Mathematical morphology analysis methods

The word morphology has differing definitions, but the following definition is applied in this thesis:

Morphology (noun), (môr-fŏl'ə-jē)	The study and the analysis of geometrical structures, based on set theory, lattice theory, topology and random functions

Thus, the morphology of a material equals a sum of the information regarding its structure. There are several methods available – that with a high degree of accuracy – describe the morphology of a material. In the field of materials science, one is often interested in defining parameters of a material, such as lattice structure, dislocation density, grain size, chemical composition and crystallographic orientation.

Information about the material morphology may aid in explaining why a certain material is exhibiting certain material properties. For example, the use of crystallographic orientation analysis has discovered that there is a correlation between the grain orientation and the pitting corrosion resistance in AISI 304L austenitic stainless steel, where the close-packed [101] direction proved most resistant to pitting corrosion (Krishnan, Dumbre, Bhatt, Akinlabi, & Ramalingam, 2013).

The list of available analysis methods is long and complicated. Therefore, this thesis only focuses on describing the methods utilized to obtain usable results. This thesis used SEM – Scanning Electron Microscopy – to gauge the chemical composition and lattice structure of a selection of heat treated samples. The analysis methods used (and the intended goal of said analysis) is listed below:

- EDS — *Energy-dispersive X-ray Spectroscopy*, to identify chemical composition of phases
- EBSD — *Electron Backscatter Diffraction*, to visually identify the lattice structures of phase fields, using multi-color coding and image analysis

The following section will briefly explain the physical principles that govern these analysis methods.

2.6.1 EDS (Energy-dispersive X-ray Spectroscopy)

EDS is an analytical technique that is often used to define the chemical characterization of a sample. It relies on the physical principle that an X-ray excitation interacts with said sample, and that all elements have a unique atomic structure that allows unique set of peaks to appear on its X-ray emission spectrum.

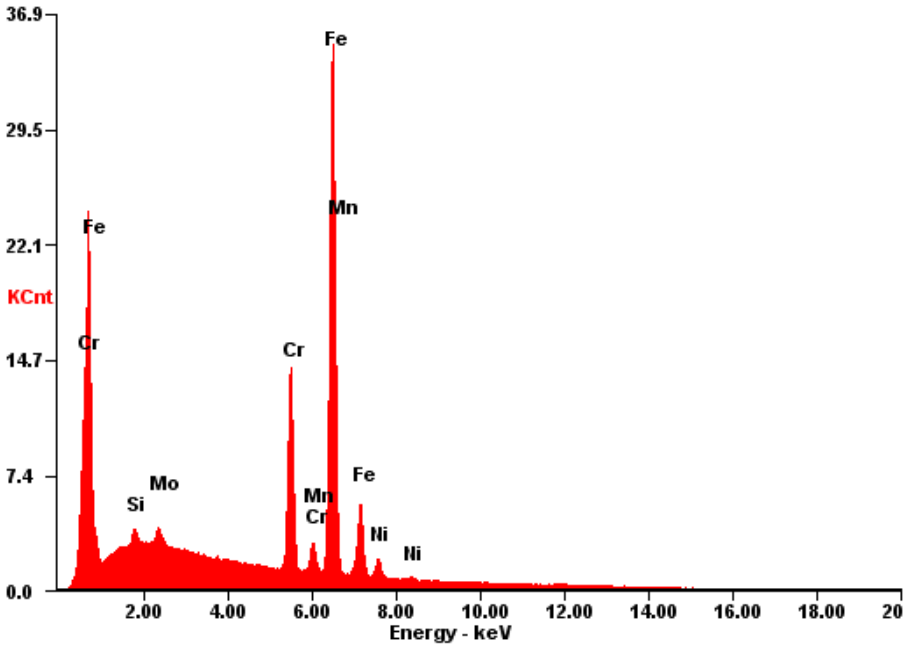

Figure 2.10 – An example of an EDS spectrum from S165M, illustrating the chemical composition of a sample (UiS v/ Ingunn Oddsen, 2015)

A high-energy beam of charged particles – such as electrons – is focused into the sample being studied. The beam may excite an electron in an inner shell of an element, ejecting it from the shell and thus creating an electron hole. An electron from an outer, higher-energy shell then fills said hole, and the difference in energy between the higher and lower energy shells may be released in the form of an X-ray (Russ, 1984).

The frequency of and the energy of the emitted X-rays are measured using an energy-dispersive spectrometer. Since the energies of the X-rays are characteristic for each element, and the number of X-rays an indicator of the amount of the element present, one can use EDS to chart the elemental composition of the sample (Russ, 1984). The different peaks in the EDS spectrum differentiate between the elements, and the height of the peaks is an indicator of the amount in the sample.

2.6.2 EBSD (Electron Backscatter Diffraction)

EBSD is a technique that gives crystallographic information about the microstructure of a sample. It is often used to identify crystal systems, and is therefore well suited for morphology studies. In order to perform an EBSD scan, one needs to have a flat/polished sample mounted at a highly titled angle (approximately 70 ° from the horizontal) towards a diffraction camera. The high angle is necessary to ensure a sufficient amount of contrast in the resulting backscatter diffraction pattern. A phosphorous screen is mounted at a 90 ° angle relative to the electron beam. A CCD camera focuses the image on the screen, caused by backscattered electrons (Palizdar, Cochrane, Brydson, Leary, & Scott, 2010).

Some of these backscattered electrons may exit the sample at the Bragg condition related to the spacing of the periodic atomic lattice planes of the crystalline structure and diffract. Some of these diffracted electrons may hit the phosphorous screen, causing it to fluoresce. An EBSP – Electron Backscatter Diffraction Pattern – is formed when many different planes in the sample diffract different electrons. This forms what is known as Kikuchi bands (Figure 2.11), which correspond to each of the lattice diffracting planes.

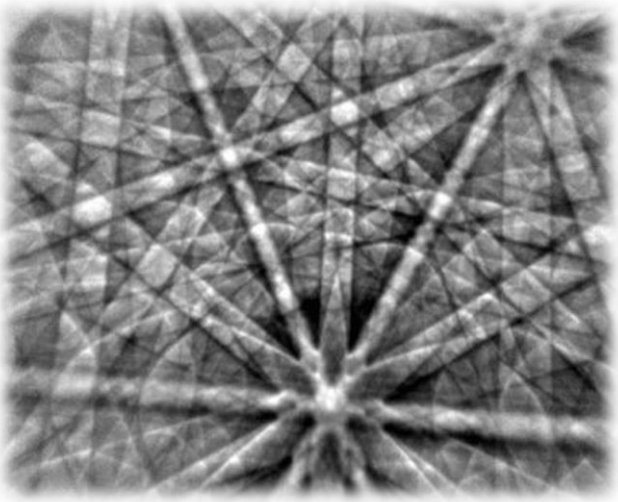

Figure 2.11 – Illustration of Kikuchi bands caused by diffracting electrons, courtesy of (Schwarzer, 2013)

Each of these bands can be indexed individually by the Miller indices[2] of the diffraction plane that formed it. For most materials, it is only necessary to have three intercepting bands in order to describe a unique solution to the crystallographic orientation. Modern software utilizes databases containing known geometry in order to index the elements faster.

[2] The integers *h, k* and *l* determining a family of lattice planes

Normally, a sample is indexed before the results can be processed and analyzed. Depending on the software controlling the set-up, one often selects an area to be scanned. A set of parameters are set for the scan, including the scan area and the scan step size. The selected area is then indexed based on known crystallographic data. Thus – given that anything but scan area is ceteris paribus[3] – a smaller area requires less scan time than a larger one (Palizdar, Cochrane, Brydson, Leary, & Scott, 2010).

Once a sample space is indexed, one can among other things identify the phases present in the material. It is worth to note that due to the very small difference in lattice parameters of BCC and BCT caused by martensitic transformation – more specifically Bain Strain, described in section 2.4 – most software can't differentiate between martensite and ferrite during such a scan. However, it can easily detect the difference between austenite (FCC) and ferrite/martensite (BCC/BCT). For martensitic ferritic steel such as S165M, the technology may be used in order to identify retained or reversed austenite, due to its crystallographic difference from martensite/ferrite.

[3] Ceteris paribus = *«Other things being equal or held constant»*

This page has intentionally been left blank

3. Experimental methods

The experimental work of the thesis consisted of 4 main phases:

1. Rough machining of material into appropriate heat treatment samples
2. Heat treatment (hardening, quenching and tempering)
3. Detailed machining of test specimens, according to the established standards utilized for mechanical testing at NOMAC (ASTM A370, 2014)
4. Mechanical testing and metallographic examination of said specimens, including:

    - Tensile stress testing
    - Charpy-V impact testing
    - Hardness testing
    - Microstructural analysis using optical light microscope
    - Chemical analysis of phases in SEM, using energy-dispersive X-ray spectroscopy (EDS)
    - Crystallographic verification of phases in SEM, using electron backscatter Kikuchi diffraction (EBSD)

The goal of said tests were to obtain information regarding the material yield strength, tensile strength, modulus of elasticity, area reduction, elongation, absorbed impact energy, hardness, macrostructure, microstructure and chemical composition of the observed phases.

This data were to form the foundation of further analysis.

3.1 Material specification

The material used in this thesis is S165M, forged by NOMAC. All of the material used in this thesis came from a single charge, A19606. The chemical composition of the delivered material was measured by a Spectrolab M-10 spectrograph based on OES (Optical Emission Spectroscopy). The measured chemical composition is illustrated in Table 2.2, first presented on page 3.

Reference material properties from charge A19606 is shown in Table 3.1 (collected from the material certificate, see Appendix B). Note that the properties are collected from transverse samples. This causes them to deviate from the experimental samples used in the thesis (as it is based on longitudinal samples). The properties were obtained after the material was hardened at 1000 °C, quenched in water and tempered at 560 °C for 6 hours. All tests were performed at 20 °C. Impact and hardness values are average values.

Table 3.1 – Mechanical reference properties of charge A19606

Material property	Value
Yield strength ($Rp_{0.2}$)	841 MPa
Tensile strength	996 MPa
Elongation	18 %
Reduction of area	45 %
Impact value (average)	115 J
Hardness Brinell (average)	293

3.2 Rough machining

The material delivered from NOMAC originated from a circular bar of Ø230 mm, with a forging ration of 5.9:1. Plates were cut in the longitudinal direction at ¼ of the thickness, also known as T/4. See Appendix H for the schematics of the test piece preparation.

Two (2) different plate types were delivered, with the dimensions 120 mm x 180 mm x 20 mm and 150 mm x 180 mm x 12 mm, respectively. The specimens had to be extracted from the center of the

plate and outwards, to ensure consistent mechanical properties. The specimens were to be prepared along the longitudinal axis. This is because transverse samples have a tendency to produce a larger scatter in ductility values. The use of longitudinal samples ensured a larger degree of consistency.

The rough cutting yielded:

- 40 large rods with a square cross-section (measuring approximately 20 mm x 20 mm x 180 mm). These rods would result in specimens used for tensile stress testing, hardness testing and examinations to the sample microstructure. 2 rods were used in each heat treatment set
- 20 small rods with a square cross-section (measuring approximately 12 mm x 12 mm x 180 mm). These rods would yield 3 Charpy-V impact test specimens each. 1 rod was used in each heat treatment set

Figure 3.1 illustrates a full set of specimens. All heat treatments were performed on sets as shown in illustration.

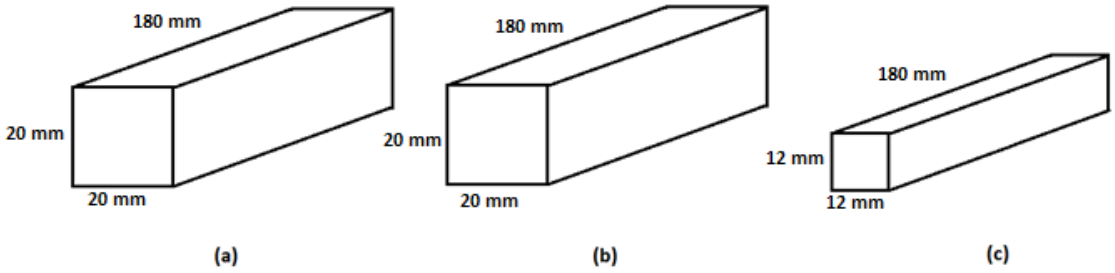

Figure 3.1 – Set of heat treatment samples, where the material yielded (a) and (b) tensile stress test/microscopy specimens; (c) Charpy-V impact specimens.

3.3 Heat treatments

The normally used hardening temperature and soaking time at NOMAC is 1000 °C and 1 hour, respectively. There was need to develop an experiment where said soaking time was the key variable. The analyzed hardening temperatures were 1000 °C and 1030 °C. The soaking times were 1, 2, 5, 10 and 20 hours, for both temperatures. Both as-quenched and tempered samples were prepared. The tempering temperature (560 °C) and duration (8 hours) remained constant. Table 3.2

illustrates the characteristics of the resulting 4 heat treatment groups. Every group yielded 5 sample sets, from soaking in 1, 2, 5, 10 and 20 hours (i.e. 20 sample sets in total).

Table 3.2 – Characteristics of heat treatment groups

Group no.	Characteristics
1 (denoted **A**)	Hardened at 1000 °C, quenched in water, not tempered
2 (denoted **AT**)	Hardened at 1000 °C, quenched in water, followed by tempering at 560 °C for 8 hours
3 (denoted **H**)	Hardened at 1030 °C, quenched in water, not tempered
4 (denoted **HT**)	Hardened at 1030 °C, quenched in water, followed by tempering at 560 °C for 8 hours

All heat treatments were performed in a programmable Nabertherm P300 furnace. All heat treatments were performed separately. The chamber temperature was monitored and controlled at all times. The specimens were consistently placed in the center of the furnace chamber, to reduce the effects of varying chamber temperatures. Prior to the insertion of specimens, the furnace was programmed to the needed temperature and allowed to stabilize for 24 hours. This was done for both the hardening and tempering treatments, yielding 30 heat treatments (i.e. 20 hardening processes and 10 tempering processes).

All heat treatments were performed in parallel with a core temperature control set, consisting of 1 large and 1 small rod, each with separate core-located thermocouples connected to temperature loggers. The core housing the thermocouple was air-sealed by spot welds. This was done to ensure the validity of the heating prior to the start of the actual hardening/tempering processes, and to quantify the time it took for the samples to reach a stable core temperature.

Figure 3.2 illustrates the coding system used for the different heat treatments. The treatment code in the figure (A10T) illustrates a sample hardened at 1000 °C for 10 hours, quenched in water and then tempered. This nomenclature will be domineering throughout the thesis, and is used to identify the different treatments.

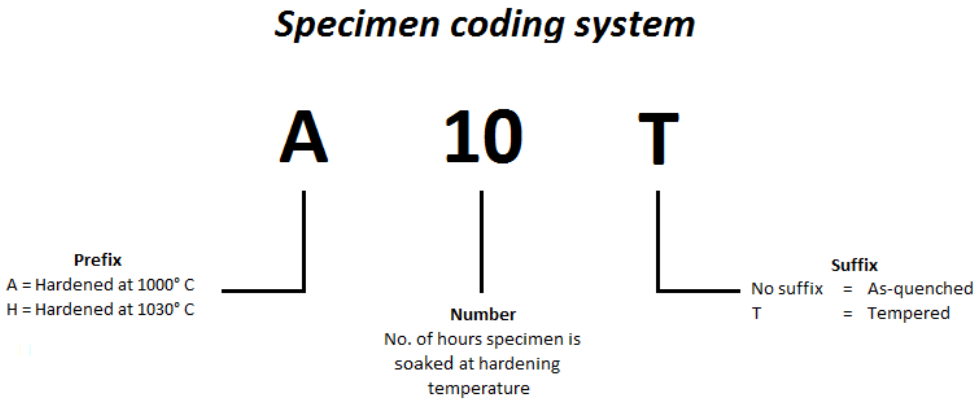

Figure 3.2 – Specimen coding system used for heat treatment identification

Table 3.3illustrates an overview of the total number of heat treatments.

Table 3.3 – Overview of performed heat treatments

Treatment code/Sample ID	Hardening temperature	Soaking time at hardening temperature	As-quenched/tempered
A1	1000 °C	1 hour	As-quenched
A2		2 hours	
A5		5 hours	
A10		10 hours	
A20		20 hours	
A1T	1000 °C	1 hour	Tempered
A2T		2 hours	
A5T		5 hours	
A10T		10 hours	
A20T		20 hours	
H1	1030 °C	1 hour	As-quenched
H2		2 hours	
H5		5 hours	
H10		10 hours	
H20		20 hours	
H1T	1030 °C	1 hour	Tempered
H2T		2 hours	
H5T		5 hours	
H10T		10 hours	
H20T		20 hours	

3.4 Machining and testing of specimens

All standardized specimen samples were machined according to standard ASTM A370. This standard specifies the necessary measurements, ratios and tolerances the test specimens must obtain in order to yield reliable results. Care was taken during machining to obtain as close to optimal measurements as possible.

3.4.1 Tensile stress testing

Post heat treatment, the total amount of base material to be used for tensile stress test specimens consisted of 40 rods, each measuring approximately 20 mm x 20 mm x 180 mm. These rods were machined into specimens with measurements and tolerances as illustrated in Figure 3.3.

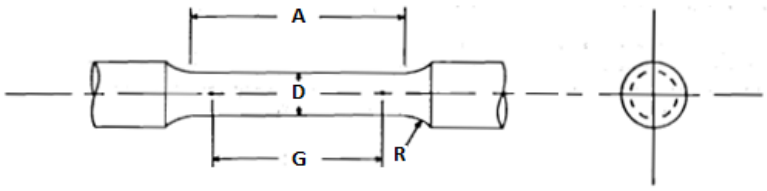

DIMENSIONS
Standard specimen

G (Gage length)	50.0 ± 0.10 mm
D (Diameter)	12.5 ± 0.25 mm
R (Radius of fillet, min)	10 mm
A (Length of reduced section, min)	60 mm

Figure 3.3 – Measurements and tolerances of tensile stress test specimens, machined according to standard (ASTM A370, 2014)

Figure 3.4 illustrates a model of a finished tensile stress test specimen, machined according to ASTM A370. In order to be fastened correctly in the tensile stress tester, the rod length had to be increased. A threaded M16 x 2 connection on one end of the specimens was used. The threaded connector had a diameter of 30 mm and a length of 125 mm, with a 45 mm deep M16 x 2 internal thread. This allowed the specimens to be mounted correctly in the tensile stress testing device. The diameter of the bottom of the threads exceeded the diameter of the reduced section of the specimen. Any

potential effect this threaded connection may have had on the results is discussed in more detail in Appendix F.2.

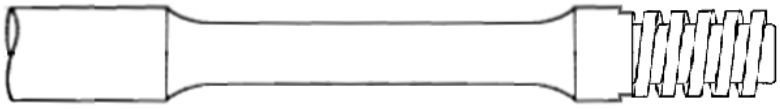

Figure 3.4 – Model of finished tensile stress test specimens (sans measurements)

The tensile stress test specimens were tested in an Instron KPX Tensile Stress Tester**.** The machine had a connected AutoX750 Automatic extensiometer, and provided live data output to a computer running Bluehill test software. The results presented in section 4 are based on calculations extracted from the raw data, not the automatically calculated results provided by the software (which turned out to be erroneous in nature).

3.4.2 Charpy-V impact testing

Post heat treatment, the total amount of base material to be used for Charpy-V impact test specimens consisted of 20 rods, each measuring approximately 12 mm x 12 mm x 180 mm. Each of these rods consisted of enough material to yield 3 impact specimens each, i.e. 60 in total. These rods were to be machined into specimens with measurements and tolerances as illustrated in Figure 3.5.

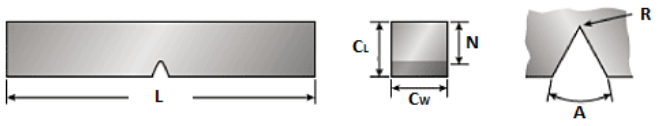

	Adjacent angles	90 deg ± 10
C_W / C_L	Cross section length/width	10 mm ± 0.025 mm
L	Length of specimen	55 mm + 0 / -2.5 mm
A	Angle of notch	45 deg ± 1 deg
R	Radius of notch	0.25 mm ± 0.025 mm
N	Dim. to bottom of notch	8 mm ± 0.025 mm
	Surface finish	1.6 µm max on notched and opposing side 3.2 µm max on other sides

Figure 3.5 – Measurements and tolerances of Charpy-V impact test specimens, machined according to standard (ASTM, 2014)

The specimens were cooled to a temperature of -20 °C prior to testing. The specimens were submerged in ethanol holding said temperature for a minimum duration of 20 minutes prior to testing. The temperature of the ethanol was verified using a calibrated digital thermometer. As per ASTM A370 standard, the specimens were broken within 5 seconds of being removed from the cooling medium (ASTM, 2014).

The impact testing was performed using a Charpy-V/Izod impact tester, which provided the measured value (i.e. absorbed impact energy) through a mechanical dial. The testing apparatus was connected to a calibrated digital readout, which allowed one to double check the result against the mechanical dial.

3.4.3 Hardness testing/Metallographic examination

The specimens used for hardness testing and metallographic examination were extracted from the end of the tensile stress test specimens. The specimens were therefore circular, with a diameter of approximately 18.5 mm. All heat treatments underwent these tests.

All samples were grinded and polished before hardness testing, to eliminate possible data fluctuations due to surface roughness. The specimens were re-grinded and polished after hardness testing, before being etched and metallographically examined in a light microscope. All grinding and polishing was done in sets of 6 or 7 specimens. Grinding and polishing was performed using a Struers Planopol Pedemax-2 rotary grinder. Table 3.4 illustrates the grinding and polishing parameters used in this thesis (durations are approximations).

Table 3.4 – Grinding and polishing parameters

Grinding/Polishing	Sheet type	Duration	Lubricant	Comments
Grinding	120 grit (*129 µm*)	3 – 7 min	Water	Until plane specimens
	220 grit (*69 µm*)	4 min		
	320 grit (*51 µm*)	4 min		
	500 grit (*29 µm*)	4 min		
	1000 grit (*19 µm*)	6 min		Longer duration (fine grinding)
	2400 grit (*9 µm*)	6 min		
	4000 grit (*5 µm*)	8 min		
Polishing	MD Mol (*3 µm*)	10 min	Struers DP-Blue	DiaDuo-2 diamond suspension was used in lieu of conventional pure diamond spray
	MD Nap (*1 µm*)	10 min		

The specimens were hardness tested using a Struers DuraScan hardness tester. The affixed testing head was a Vickers diamond pyramid. The applied load was 10 kg, which was held over 10 seconds. 20 measurements were taken from each sample, spanning a 4 x 5 grid in the center of the circular sample. All measurements had a minimum 1000 µm distance from one another, in order to reduce effects caused by microscopic work hardening. This grid is illustrated in Figure 3.6, and was utilized for all 20 heat treatments.

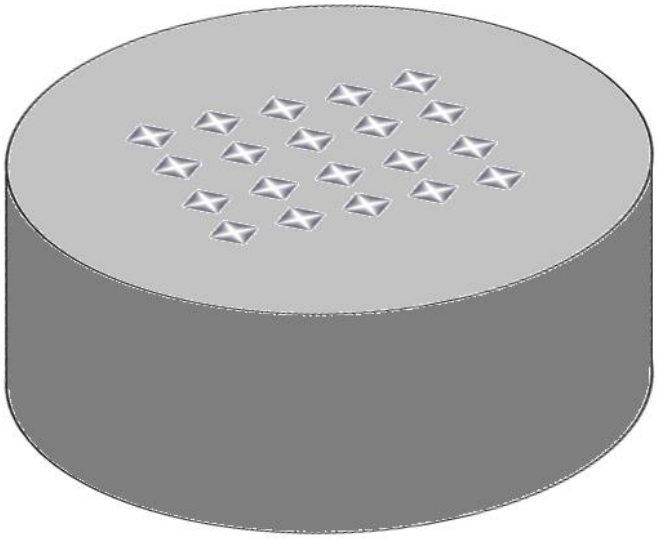

Figure 3.6 – Distribution of Hardness Vickers indentation points per sample. Hardness tested cross-section was re-grinded and used for microstructural analysis

Prior to metallographic examination, the polished samples were etched using Marble's etchant (consisting of 4 g $CuSO_4$, 20 ml 67 % HCl and 20 ml H_2O). The as-quenched specimens were etched for 30 seconds. The tempered specimens were etched for 10 – 15 seconds. The difference in etching durations was a direct consequence of the etching characteristics of as-quenched vs. tempered martensite. No voltage was applied during etching.

The specimens were viewed through a Reichert-Jung MeF3 optical light microscope, connected to a computer running ProgRes© CapturePro 2.8.8 from JENOPTIK. Pictures were taken at 10X, 20X and 50X magnification. Micrographs at 20X magnification are presented in section 4.2. Micrographs at 10X and 50X are presented in Appendix D.

3.4.5 Analysis using SEM (EDS and EBSD analysis)

The same specimens that were used in metallographic examination/hardness testing were used for SEM analysis. The specimens were re-grinded, following the protocol presented in Table 3.4. Both the EDS and the EBSD analysis were performed using a Zeiss Supra 35VP, with a backscatter detector mounted for the EBSD analysis.

EDS (Energy Dispersive Spectroscopy):

The samples A1, A20T, H1 and H20T were analyzed using EDS. For the EDS analysis, the specimens were analyzed directly following polishing. The EDS analysis provided data regarding the chemical composition of the different phases in the steel. The applied acceleration voltage was 15 kV, and samples were tested at working distances ranging from 24.4 – 25.6 mm. A total of three – 3 – different sections were analyzed using EDS, namely:

1. A general section, including all identifiable phases in the material
2. A section suspected to be δ-ferritic
3. A section suspected to be martensitic

EBSD (Electron Backscatter Diffraction):

The samples A1 and A20T were analyzed using EBSD. For the EBSD analysis, a thin wafer – approximately 2 mm thick – of the polished face was cut off. This polished wafer was then electropolished, using Struers A3 electrolyte (300 ml methanol, 180 ml 2n-butoxyethanol and 30 ml $HClO_4$). The applied voltage was 20 V, and the polishing duration was 120 seconds.

The EBSD analysis scanned a general section from both samples. The samples were scanned over an area measuring 300 µm by 300 µm. The step size was 0.20, with an accelerating voltage varying from 7.9 to 18.5 kV. These parameters gave the best scan results. Using a database of known Kikuchi bands, the analysis software generated an image where different unit cells were identified using a color code, i.e. green for identified FCC cells and pink for identified BCC cells. The fractional difference in lattice height between BCC and BCT unit cells made it impossible to differentiate between δ-ferrite and martensite in the analysis (discussed in more detail in sections 2.6.2 and 4.4.2).

4. Results

The results gathered in the experimental section consist of both qualitative and quantitative elements. The quantitative results are mainly the mechanical properties of the material, including but not limited to:

- Yield strength[4]
- Ultimate tensile strength
- Elongation at fracture
- Maximum contraction
- Modulus of elasticity (i.e. Young's modulus)
- Hardness
- Impact energy

The quantitative results presented in this thesis are all average values of two to twenty measurements, depending on the type of measurement in question. The results are presented with upper and lower standard deviation boundaries, in addition to the average values. Graphical representations of the quantitative values do not include the upper and lower standard deviation boundaries. The graphical results are scaled to clearly illustrate the spread of the measurement data.

The qualitative results mainly consist of microstructural and crystallographic analysis, stemming from the use of optical light microscopy and tests performed in the Scanning Electron Microscope (SEM). The SEM analysis included energy-dispersive X-ray spectroscopy (EDS) and electron backscatter Kikuchi diffraction (EBSD).

[4] The yield strengths presented in this thesis are based on the $Rp_{0.2\%}$ principle. The as-quenched samples produced stress/strain curves with a kink in the elastic region, occurring at approximately 650 MPa. There is no consensus at NOMAC if whether or not this is the actual yield point, seeing as the curve continues in a linear manner after this anomaly. This thesis presents yield strengths as calculated from the point of transition from linearity to non-linearity in the stress/strain curves, and does not take the kink in the curves into account when calculating the 0.2 % yield strength

4.1 Summary of quantitative results (numerical table)

All values are average values. All decimal values rounded to 3 significant figures, except those exceeding a factor of 10^3. Values are presented along with standard deviation values, where applicable. The data is presented graphically in later sections, along with correlation with soaking times.

Table 4.1 – Summary of quantitative results for all specimen groups

Treatment code	Hardness Vickers [$HV_{10\ kg}$]	Charpy-V impact energy [J]	Yield strength [MPa]	Ultimate tensile strength [MPa]	Young's modulus [GPa]	Elongation [%]	Contraction [%]
A1	346 ± 4	113 ± 9	1011 ± 4	1145 ± 6	197	18.6	60.1
A2	346 ± 4	120 ± 2	1046 ± 12	1136 ± 1	196	21.3	62.5
A5	346 ± 3	114 ± 4	1027 ± 6	1137 ± 1	197	22.1	65.9
A10	346 ± 4	121 ± 6	1007 ± 4	1136 ± 1	194	22.0	65.0
A20	350 ± 4	105 ± 5	1042 ± 5	1123 ± 2	192	21.8	64.0
A1T	327 ± 7	121 ± 3	876 ± 3	952 ± 5	180	28.6	68.6
A2T	328 ± 6	122 ± 4	880 ± 3	936 ± 2	181	29.5	69.5
A5T	329 ± 7	124 ± 5	845 ± 4	921 ± 4	181	29.6	69.7
A10T	321 ± 7	123 ± 7	865 ± 1	957 ± 5	182	28.5	68.2
A20T	317 ± 4	121 ± 5	870 ± 4	935 ± 2	180	28.4	67.7
H1	342 ± 3	125 ± 4	1026 ± 7	1141 ± 1	196	20.1	57.5
H2	349 ± 4	125 ± 5	1008 ± 8	1130 ± 1	195	21.5	64.5
H5	346 ± 5	127 ± 7	1002 ± 2	1151 ± 3	198	21.9	65.9
H10	354 ± 4	121 ± 7	1000 ± 1	1136 ± 3	199	21.3	64.2
H20	351 ± 4	132 ± 5	1042 ± 2	1130 ± 1	192	21.9	66.4
H1T	320 ± 5	123 ± 5	860 ± 9	930 ± 6	182	29.3	69.5
H2T	322 ± 6	127 ± 4	855 ± 8	931 ± 1	181	29.0	69.1
H5T	319 ± 5	122 ± 5	872 ± 5	930 ± 9	181	29.0	69.3
H10T	317 ± 4	121 ± 8	861 ± 4	930 ± 3	183	28.7	69.5
H20T	318 ± 5	128 ± 1	864 ± 4	918 ± 1	179	28.9	69.3

4.2 Microstructure in optical light microscope

The following section will present single, representative images from the microstructures of all 20 heat treatments. See figures 4.2 through 4.5. All images are shown at 20X magnification. A selection of images is discussed in more detail in section 5.3, in terms of general structure development and any potential difference between the longitudinal and the transverse microstructure.

The general coloring of the microstructure may appear to be fluctuating. However, this is a result of microscopy-images being collected at different times. The Reichert-Jung MeF3 optical light microscopy is adjustable in a number of ways, including filtering layers and aperture/contrast ratios. The adjustment that yielded the best resolution and contrast varied from sample to sample. This resulted in the varying degrees of blue/brown coloring. The images are presented in the original captured colors as opposed to black/white, due to the possibility of details going lost in the conversion. The coloring is therefore not a result of the microstructure, but the applied method.

All of the images were collected from the same area of all samples. The images were captured from a cross section of the tensile stress rods, approximately 15 mm from one end. See Figure 4.1 for an illustration.

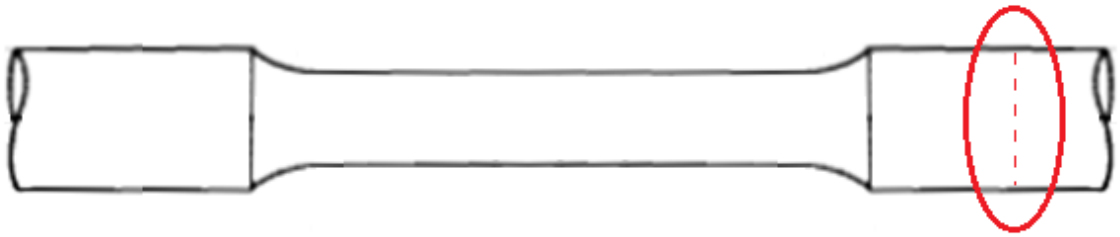

Figure 4.1 – Optical microscopy specimen extraction from tensile stress test specimens. Cross sectional area (circled in red) was analyzed

4.2.1 As-quenched A-samples (1000 °C, A1 – A20)

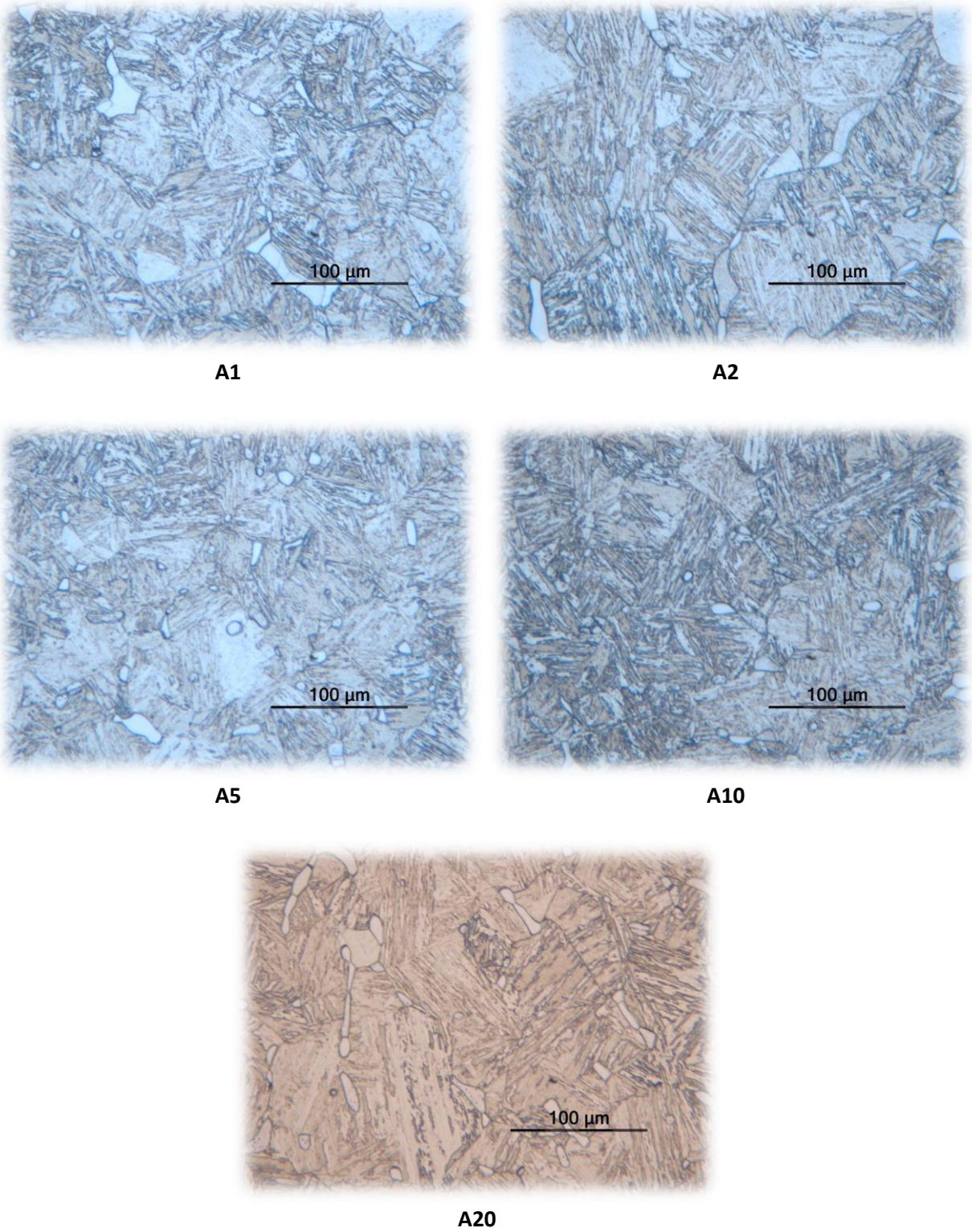

A1 A2

A5 A10

A20

Figure 4.2 – Microstructures of A-samples (20X magnification)

4.2.2 Tempered A-samples (1000 °C, A1T – A20T)

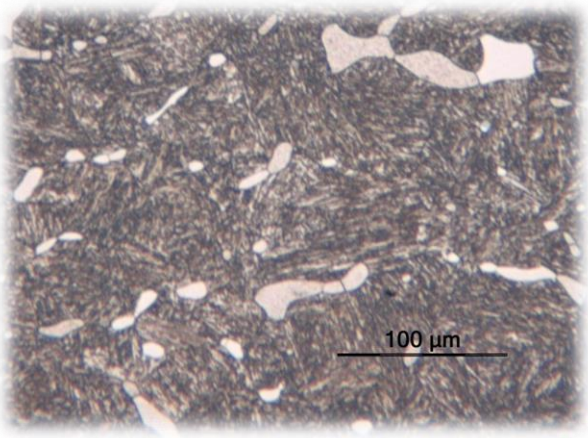

A1T

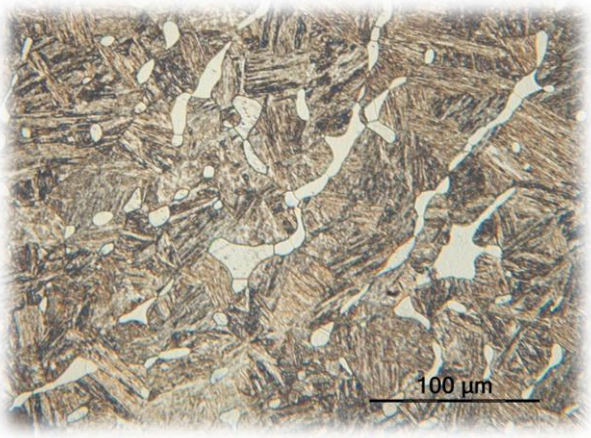

A2T

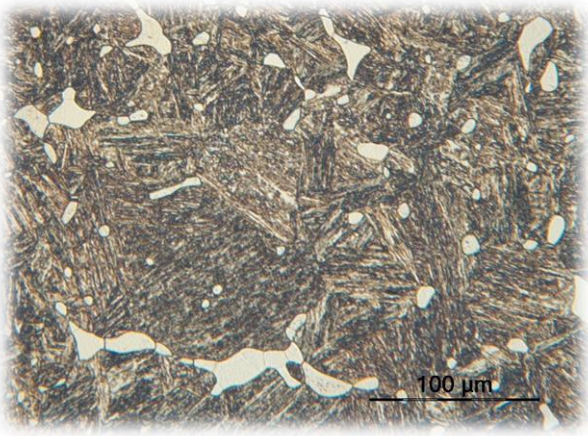

A5T

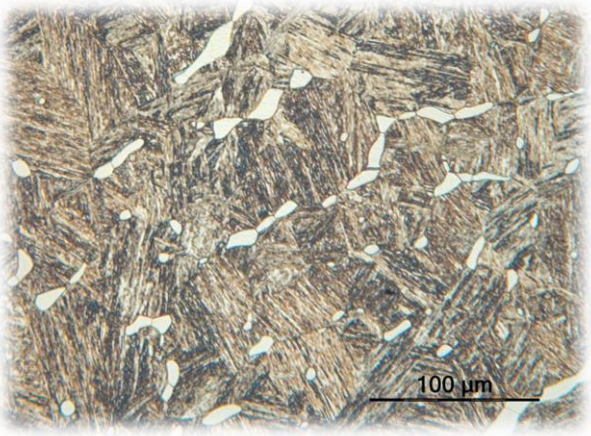

A10T

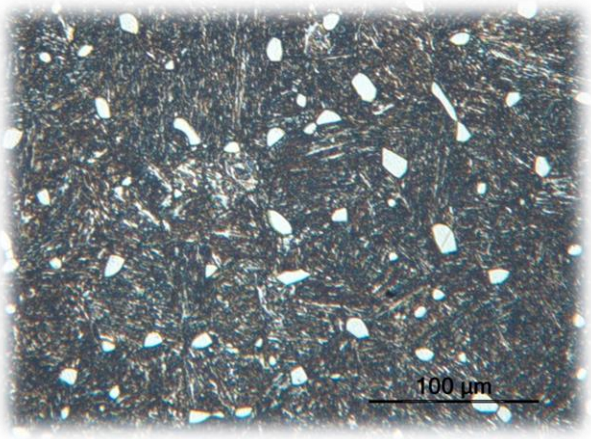

A20T

Figure 4.3 – Microstructures of AT-samples (20X magnification)

4.2.3 As-quenched H-samples (1030 °C, H1 – H20)

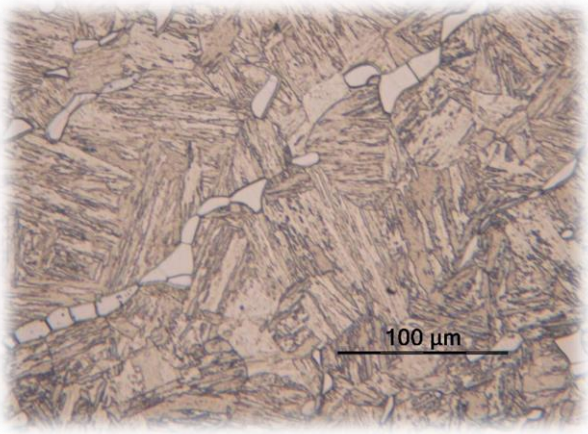

H1

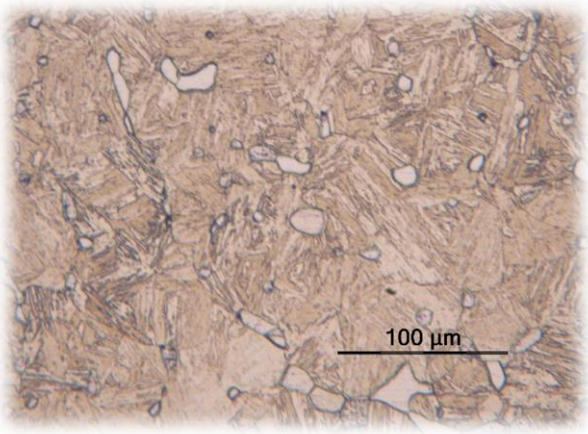

H2

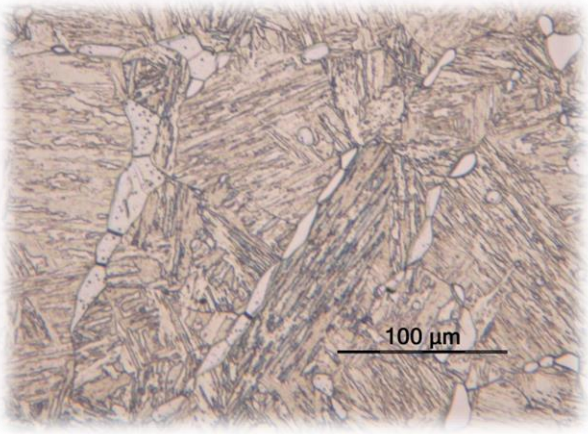

H5

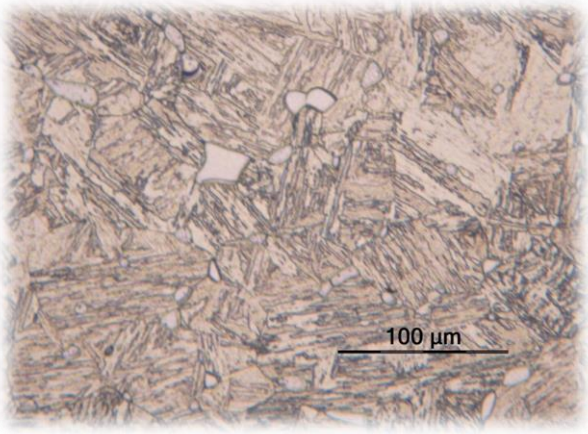

H10

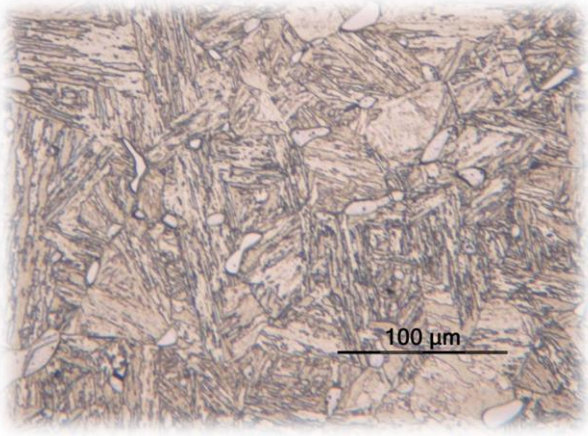

H20

Figure 4.4 – Microstructures of H-samples (20X magnification)

4.2.4 Tempered H-samples (1030 °C, H1T – H20T)

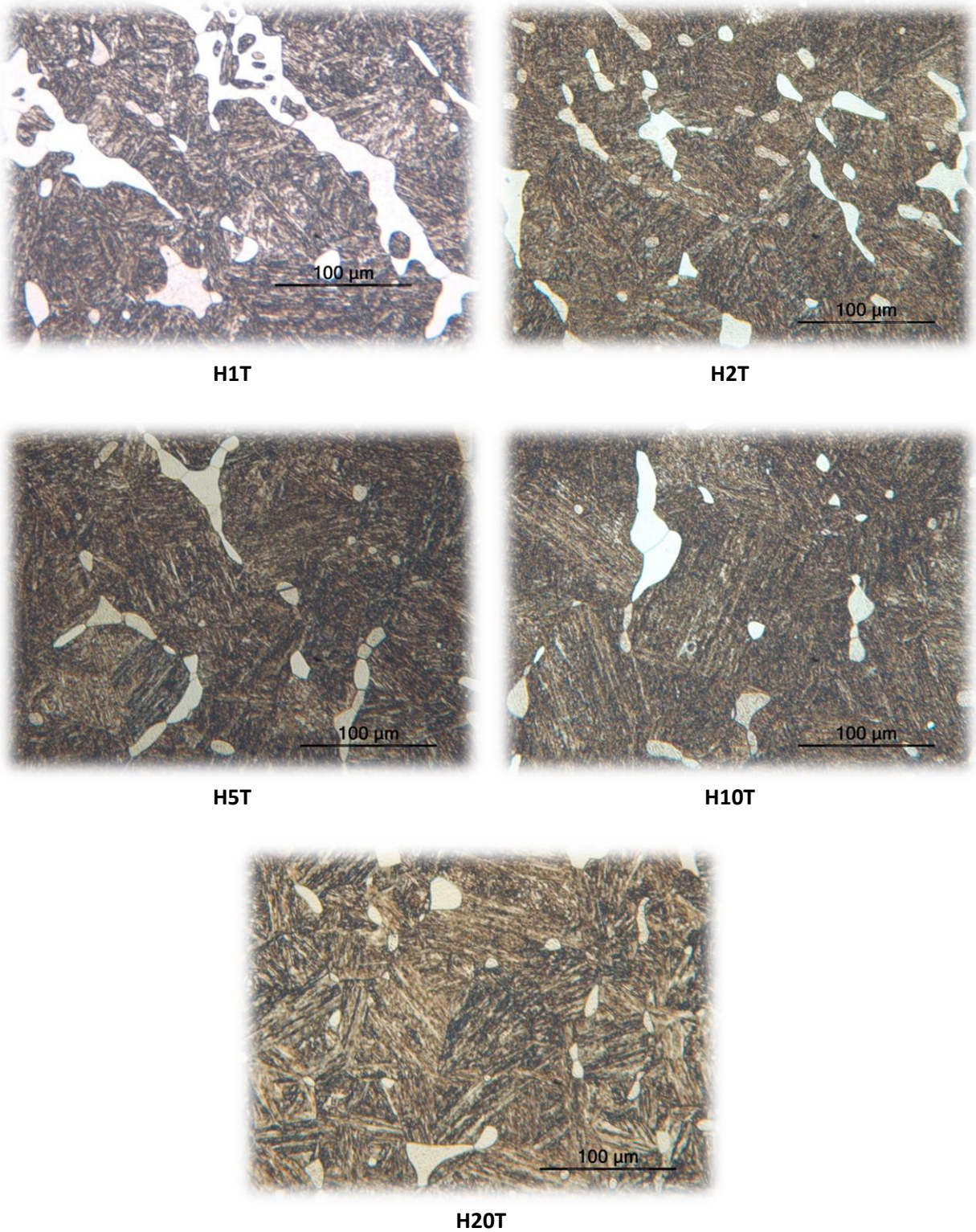

H1T H2T

H5T H10T

H20T

Figure 4.5 – Microstructures of HT-samples (20X magnification)

4.3 Graphical presentations of data sets

4.3.1 Yield strength

The results presented in Figure 4.6 below are calculated using the raw data collected during tensile stress testing. The yield strength is calculated from the 0.2 % point, and is therefore compatible with $Rp_{0.2\%}$.

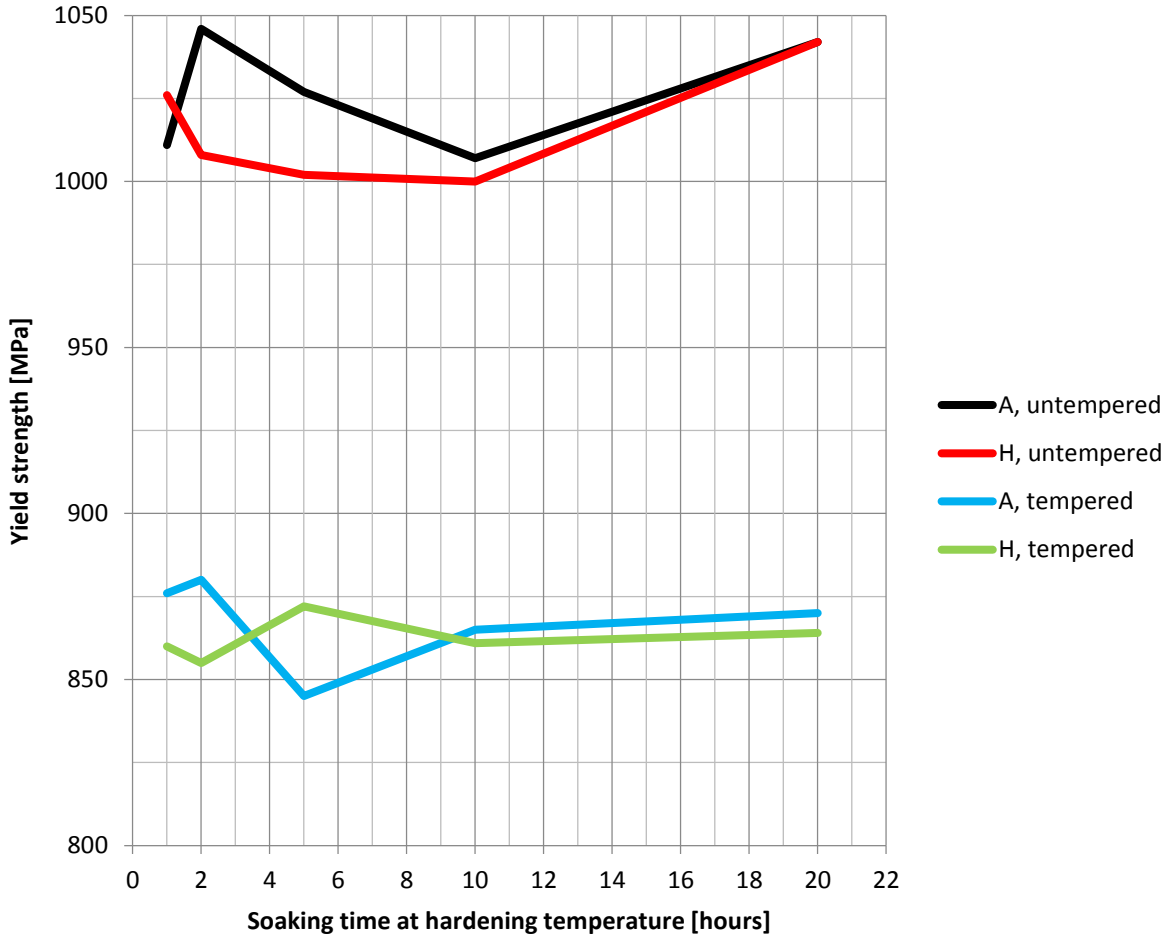

Figure 4.6 – Yield strength (0.2 %) VS. Soaking time at hardening temperatures

As expected, the data shows a clear difference between the as-quenched and tempered samples. There is some fluctuation in the data, but given the standard deviations in Table 4.1, there is no indication that there are any upwards- or downwards-pointing trends. The as-quenched yield strengths differ somewhat from NOMAC standards. This is discussed in further detail in section 5.2.

4.3.2 Ultimate tensile strength

The results presented I Figure 4.7 below are those provided from the tensile stress testing software. The data was also verified with calculations performed using the raw data.

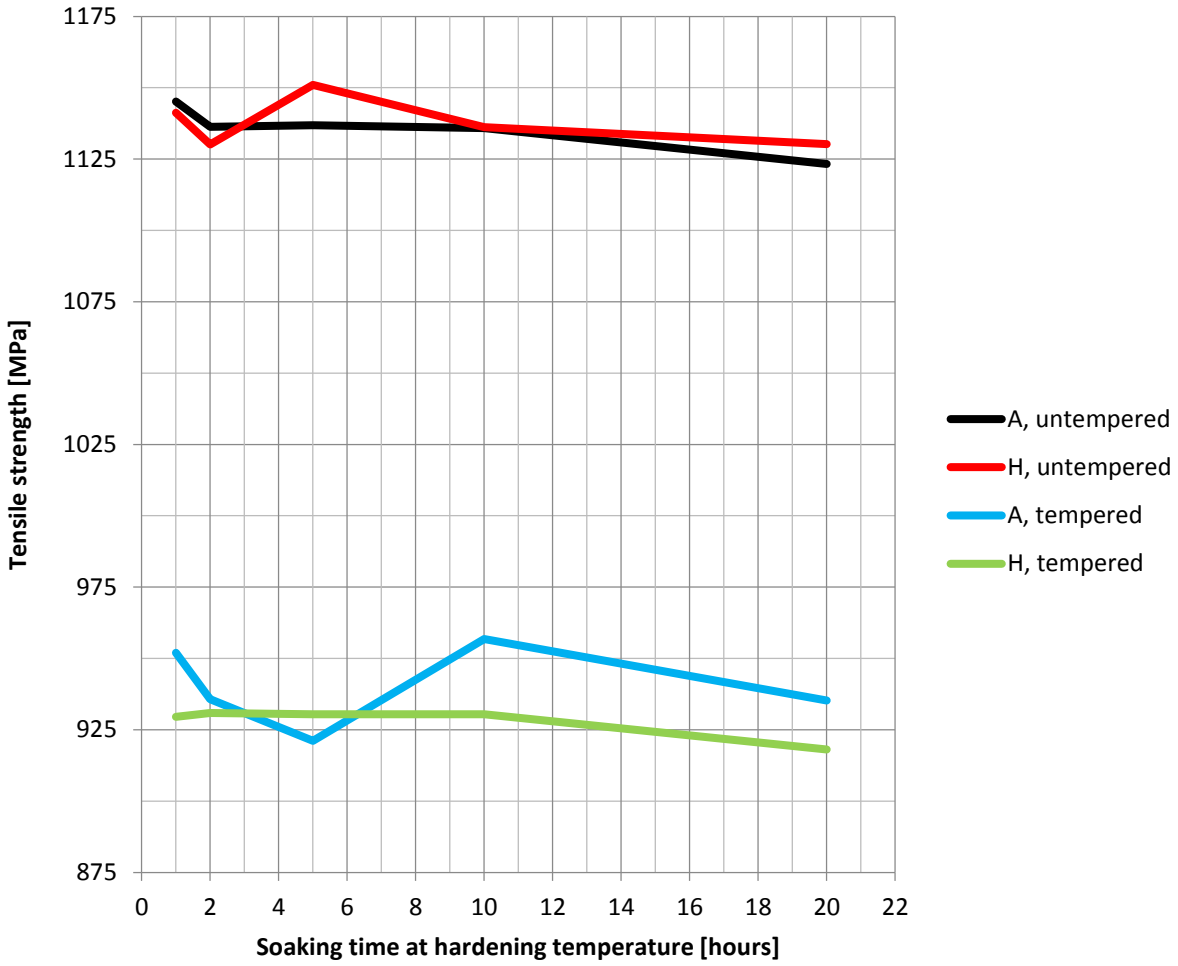

Figure 4.7 – Ultimate tensile strength VS. Soaking time at hardening temperatures

The ultimate tensile strength data is by far the most consistent data set. Although the tempered A-sample shows the largest data variation (when compared to the other 3 sets), the variation is not unexpected due to the calculated standard deviations of the sample sets. It is worth to note that all of the sample sets show slightly lower values with increasing soaking times. The possible reasons for this are discussed in more detail in section 5.4.

4.3.3 Charpy-V impact energy

All heat treatments were impact tested at -20 °C, as per NOMAC standards. All heat treatments yielded 3 Charpy-V impact specimens each, totaling 60 specimens. The data presented in Figure 4.8 below are average values.

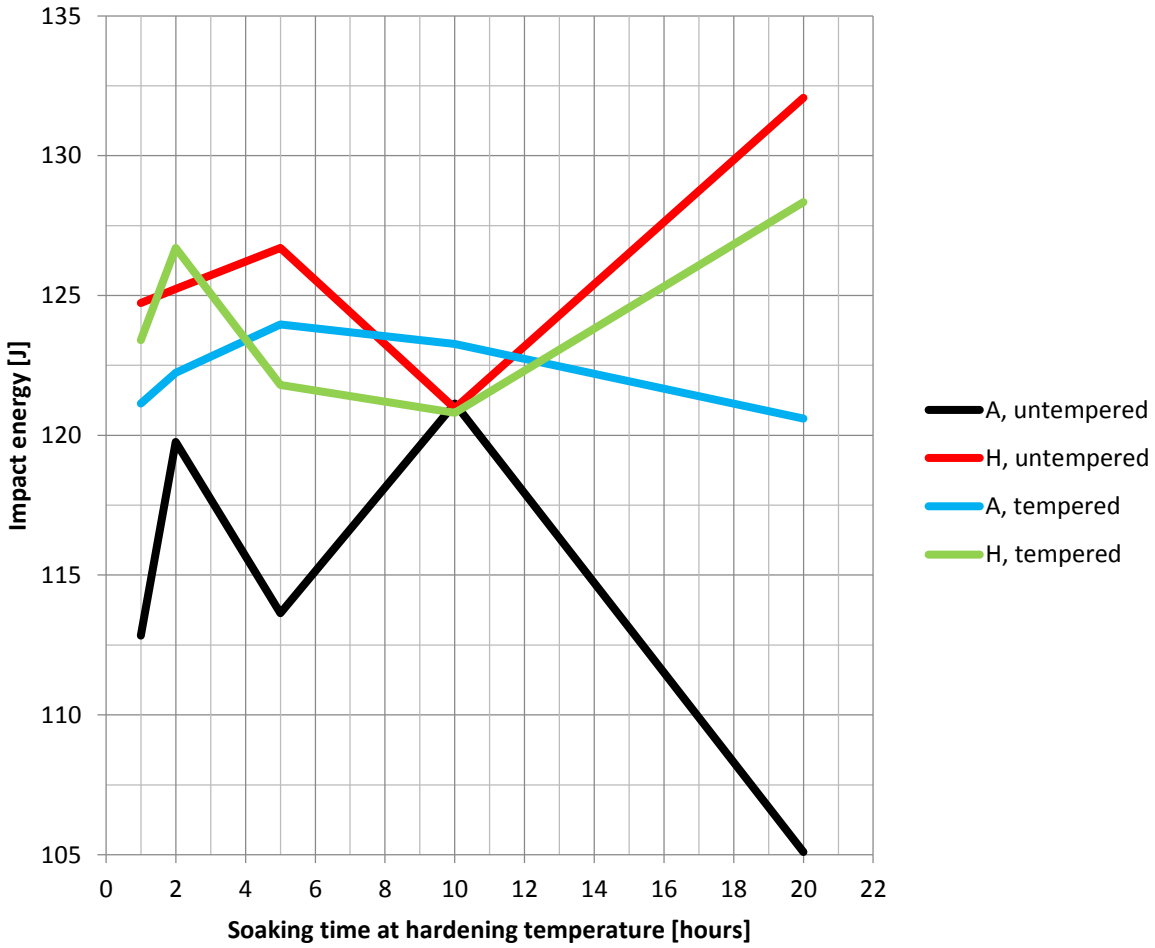

Figure 4.8 – Charpy-V impact energy VS. Soaking time at hardening temperatures

The data spans from 105.1 J (A20) to 132.1 J (H20). The impact values from the 20 heat treatments differed from what was expected. Most notably, the impact energy for S165M is expected to be higher for tempered samples than what this data suggests. Also, there is a stark alternation point in the data, located at 10 hours, suggesting that metallurgical differences with an effect on the impact energy occurs around this soaking time. This is discussed in more detail in section 5.2.

4.3.4 Hardness

All of the separate 20 heat treatments were hardness tested. The results are presented below in Figure 4.9, where the data is plotted VS. the respective soaking times the samples underwent during hardening. The data presented in Figure 4.9 are average values.

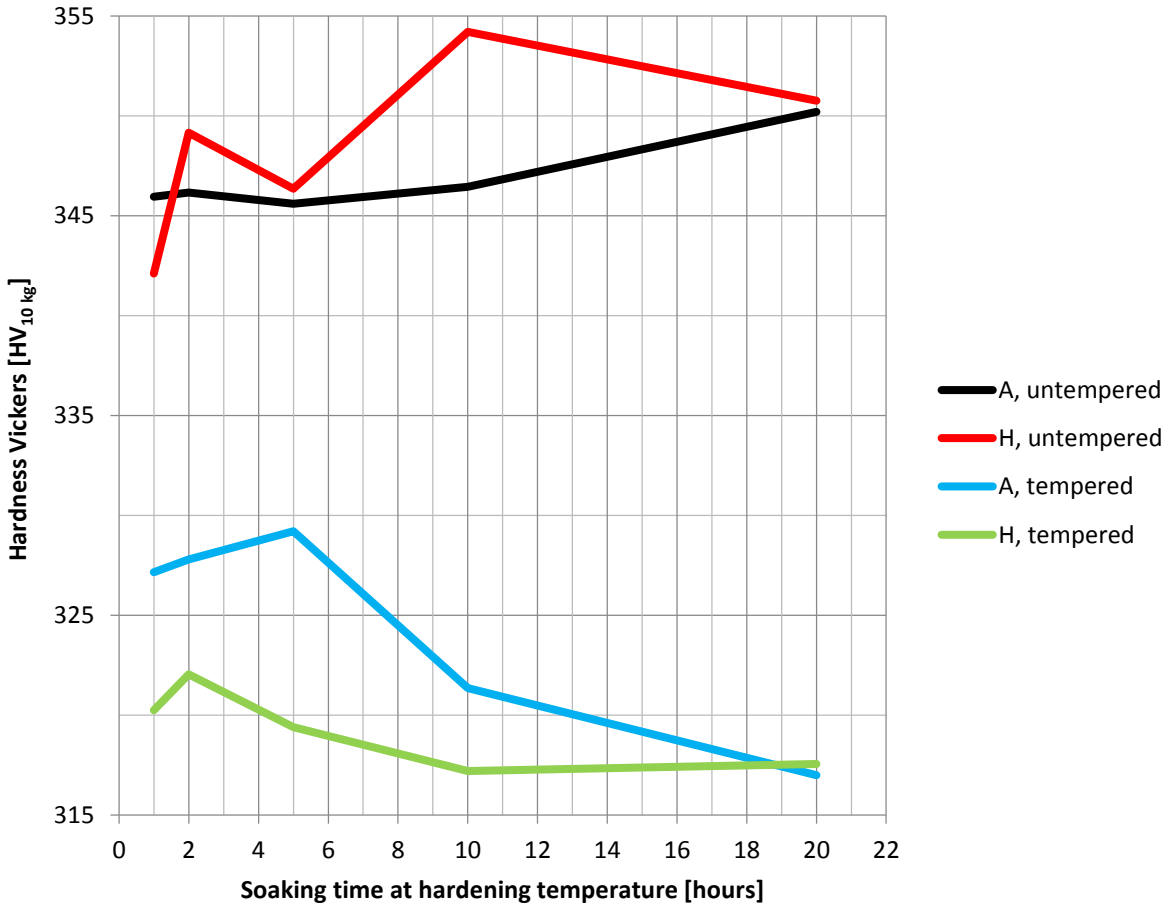

Figure 4.9 – Hardness Vickers VS. Soaking time at hardening temperatures

As the data shows, there is a clear difference in hardness between the as-quenched and the tempered samples. On average, the as-quenched samples gave a measured hardness value approximately 22 – 25 HV higher than their tempered counterparts. Some sample sets seem to indicate an increasing hardness trend with increasing soaking times, and vice versa. However, the data change is not necessarily indicating any trends when the sample standard deviations are considered. The hardness data differentiates somewhat from NOMAC standards. This is discussed in further detail in section 5.2.

4.4 Morphology analysis

From the analysis performed using Scanning Electron Microscopy, a vast array of data were collected. Most notably, detailed information regarding the chemical composition and crystallographic structure was obtained. The following sections present these results, along with general comments and inputs. The relevant results are discussed in more detail in section 5.4.

4.4.1 EDS results

4 separate heat treatment samples were analyzed using EDS: A1, A20T, H1 and H20T. The four samples were an adequate representation of the heat treatments, because:

- The samples spanned the shortest and longest soaking time for both hardening temperatures
- Both as-quenched and tempered samples from both temperatures were analyzed

Results from all 4 samples are included in the following section (Figures 4.10 through 4.14), and present:

- EDS spectrum and chemical composition of a general cross-section from the samples
- Chemical composition of phases suspected to be martensite and ferrite

The images showing where the scans were taken are for illustrational purposes only. Thus, these images are only included for sample A1 (Figures 4.10 and 4.11). Samples A20T, H1 and H20T are presented with the general EDS spectrum and the 3 separate EDS scans of the general cross-section, ferrite and martensite, respectively.

A1:

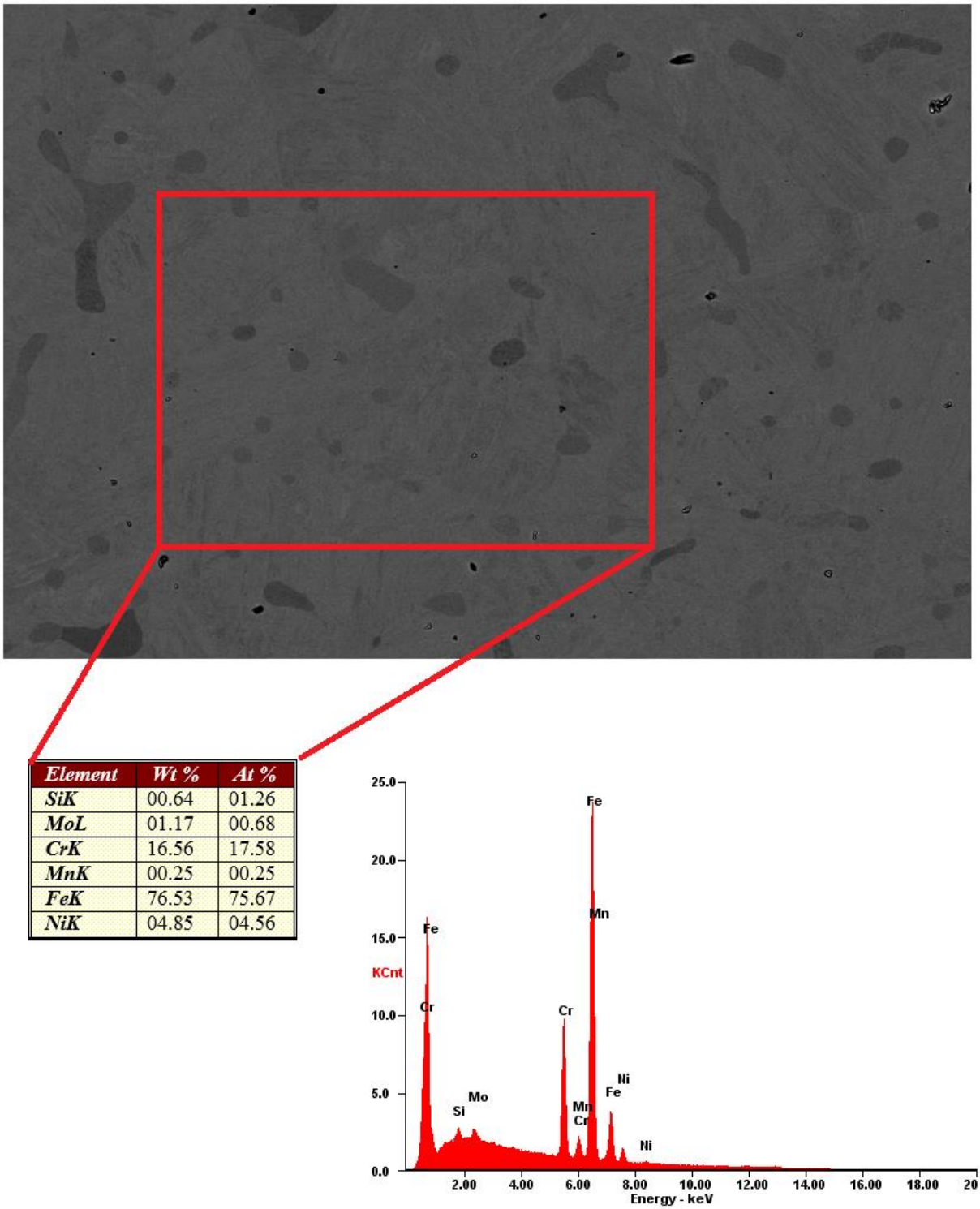

Figure 4.10 – EDS scan of a general cross-section from sample A1, including EDS spectrum

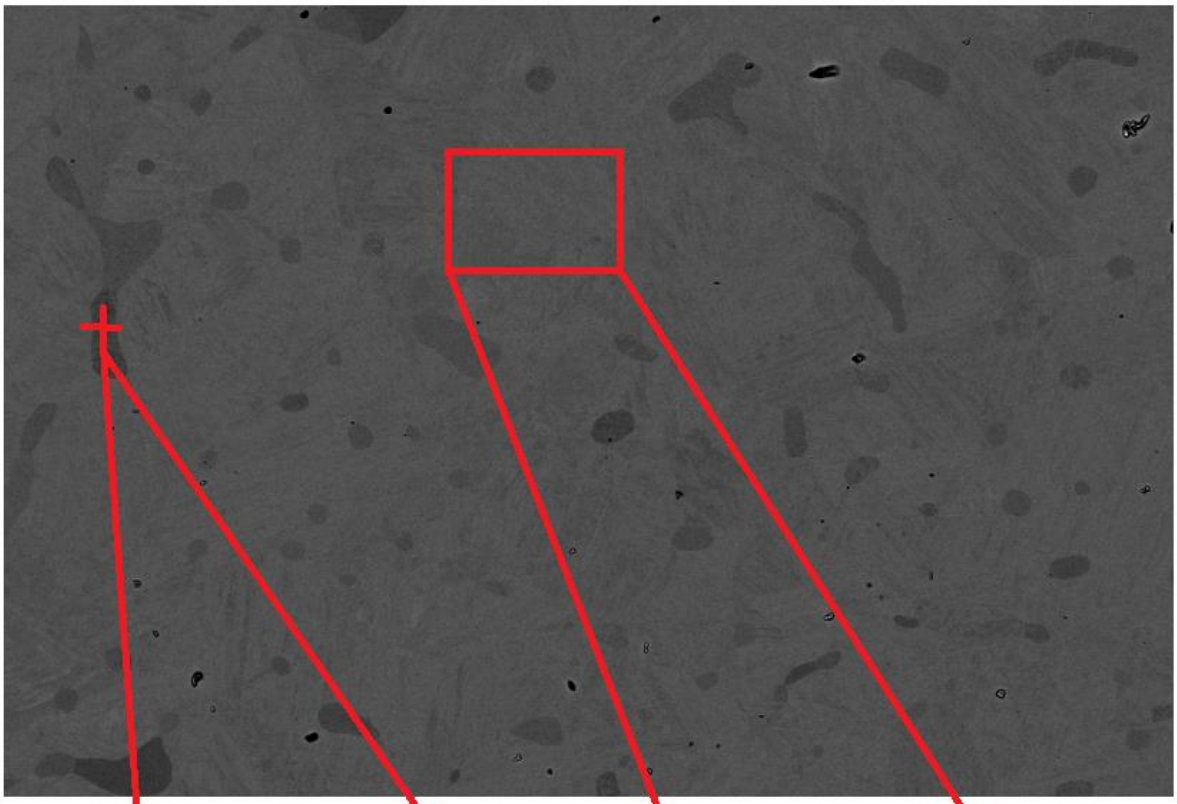

Element	Wt %	At %
SiK	00.66	01.30
MoL	02.23	01.29
CrK	20.35	21.62
MnK	00.26	00.26
FeK	73.70	72.91
NiK	02.79	02.63

(a)

Element	Wt %	At %
SiK	00.56	01.10
MoL	01.30	00.75
CrK	16.27	17.31
MnK	00.41	00.42
FeK	76.26	75.53
NiK	05.20	04.90

(b)

Figure 4.11 – Chemical composition obtained from EDS scans of A1, from (a) ferrite and (b) martensite, respectively. The image displays the sections the scans were performed on

A20T:

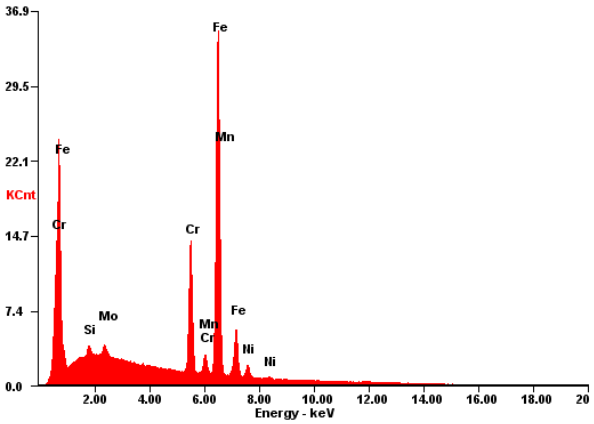

(a)

Element	Wt %	At %
SiK	00.63	01.23
MoL	01.17	00.67
CrK	16.42	17.44
MnK	00.13	00.13
FeK	76.84	75.99
NiK	04.81	04.53

(b)

Element	Wt %	At %
SiK	00.61	01.20
MoL	01.20	00.69
CrK	16.31	17.33
MnK	00.31	00.31
FeK	76.55	75.74
NiK	05.04	04.74

(c)

Element	Wt %	At %
SiK	00.72	01.42
MoL	02.23	01.28
CrK	20.59	21.85
MnK	00.00	00.00
FeK	73.94	73.07
NiK	02.53	02.38

(d)

Figure 4.12 – EDS scan results of A20T, including (a) EDS spectrum of a general cross-section, plus chemical composition of (b) said cross-section, (c) martensite and (d) ferrite

H1:

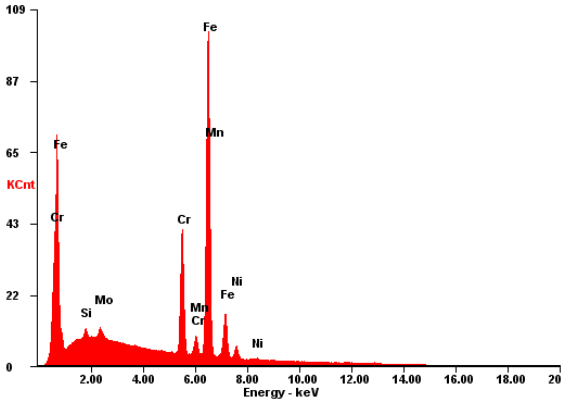

(a)

Element	Wt %	At %
SiK	00.57	01.13
MoL	01.19	00.69
CrK	16.38	17.41
MnK	00.25	00.25
FeK	76.67	75.87
NiK	04.94	04.65

(b)

Element	Wt %	At %
SiK	00.59	01.16
MoL	01.18	00.68
CrK	16.01	17.03
MnK	00.32	00.32
FeK	76.28	75.52
NiK	05.62	05.29

(c)

Element	Wt %	At %
SiK	00.63	01.24
MoL	02.09	01.20
CrK	20.36	21.63
MnK	00.07	00.07
FeK	74.08	73.25
NiK	02.77	02.60

(d)

Figure 4.13 – EDS scan results of H1, including (a) EDS spectrum of a general cross-section, plus chemical composition of (b) said cross-section, (c) martensite and (d) ferrite

H20T:

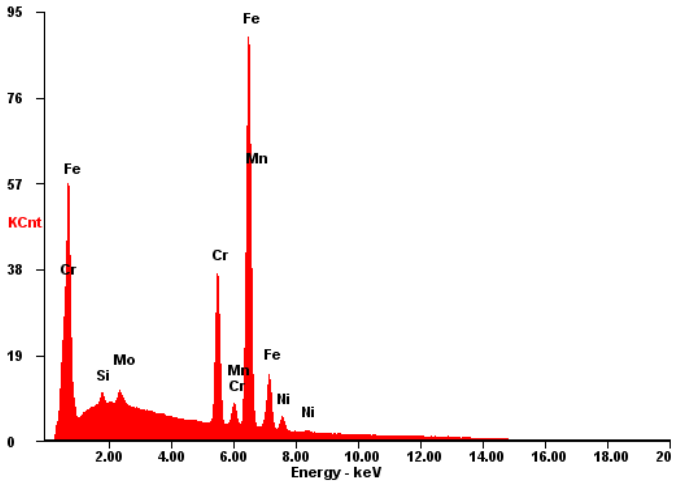

(a)

Element	*Wt %*	*At %*
SiK	00.58	01.14
MoL	01.28	00.74
CrK	16.66	17.70
MnK	00.36	00.36
FeK	76.37	75.58
NiK	04.76	04.48

(b)

Element	*Wt %*	*At %*
SiK	00.58	01.13
MoL	01.12	00.64
CrK	16.00	17.02
MnK	00.41	00.41
FeK	76.43	75.65
NiK	05.47	05.15

(c)

Element	*Wt %*	*At %*
SiK	00.63	01.25
MoL	02.17	01.25
CrK	20.19	21.46
MnK	00.24	00.24
FeK	74.05	73.25
NiK	02.72	02.56

(d)

Figure 4.14 – EDS scan results of H20T, including (a) EDS spectrum of a general cross-section, plus chemical composition of (b) said cross-section, (c) martensite and (d) ferrite

These results from the general cross-section scans are consistent with the bulk material composition listed in the material certificate (see Appendix B). There are slight variations from sample to sample, but nothing that indicates any drastic changes in the alloy chemistry.

EDS scans cannot be used independently to identify phases, since the chemical composition of phases is not a constant factor. However, due to the morphology effects of certain alloy elements, one can expect to see more of ferrite formers – and consequently less of austenite formers – in phases suspected to be ferrite, and vice versa. From the scans of the phases suspected to be martensitic (Figures 4.11 (b), 4.12 (c), 4.13 (c) and 4.14 (c)), we see a higher wt% of austenite formers such as Mn and Ni than in the suspected ferritic phase. Consequently, there are higher amounts of certain ferrite formers (i.e. Mo, Si and Cr) in the suspected ferritic phases (Figures 4.11 (a), 4.12 (d), 4.13 (d) and 4.14 (d)) than in their martensitic counterparts.

4.4.2 EBSD crystallographic scan results

Samples A1 and A20T were scanned using EBSD in order to properly identify the crystallographic structure of the phases present in the alloy. The suspected phases – i.e. ferrite and martensite – have differing crystallographic unit cells, and they are thus in theory possible to separate using such analysis. However, as discussed in section 2.6.2, the martensitic unit cells (BCT) are difficult for EBSD software to separate from ferritic unit cells (BCC), due to the fractional difference in the single lattice parameter (and the unknown orientation of the individual BCT cells). Therefore, the EBSD scan could not be used to *identify* martensite, but as a means to *separate* between martensite/ferrite and possible occurrences of austenite. This is a useful tool when evaluating if the structure contained any notable amounts of retained or reversed austenite.

Figures 4.15 and 4.16 show the EBSD scans developed from the A1 and A20T samples, respectively. In the figures, (a) illustrates a micrographic view of the scan area, and (b) illustrates the identified unit cells in the sample, using color coding (see legend in figures). Some areas were not identifiable using the software, and were most likely physical or digital pollution caused by particles or code-error.

Figure 4.16 shows the scan performed on the sample containing tempered martensite. As shown in the figure, the white areas differentiate from the darker, surrounding phase. The crystallographic analysis reveals the white areas to consist of solely BCC unit cells, which is consistent with ferritic structure. The surrounding martensite were identified to consist of BCC cells – in reality BCT cells, but the software was unable to differentiate between them – mixed with a fair amount of FCC-cells, i.e. austenite. This indicates that the tempered sample consists of ferrite and martensite, and where the martensitic structure also includes a fine dispersion of austenite. This is believed to be reversed austenite, seeing that the austenite content increases from hardened-as-quenched samples to those that have been tempered. The thermal energy exposed to the sample during the 8 hours of tempering was sufficient to revert some of the as-quenched martensite to the more stable phase of austenite. Se section 5.4 for discussion in more detail regarding the phase compositions.

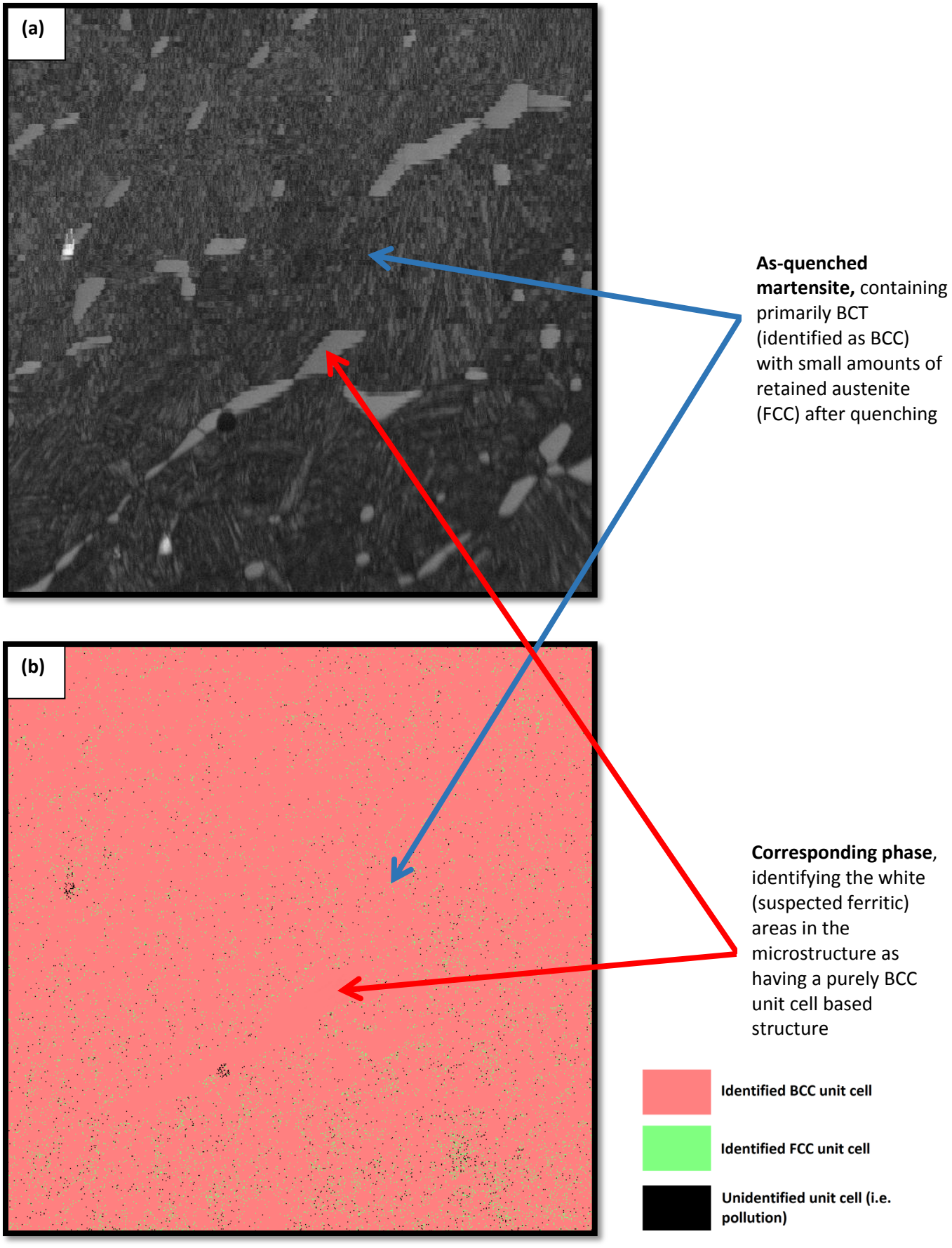

Figure 4.15 – EBSD scan of A1, illustrating the identified unit cells in the material crystal structure

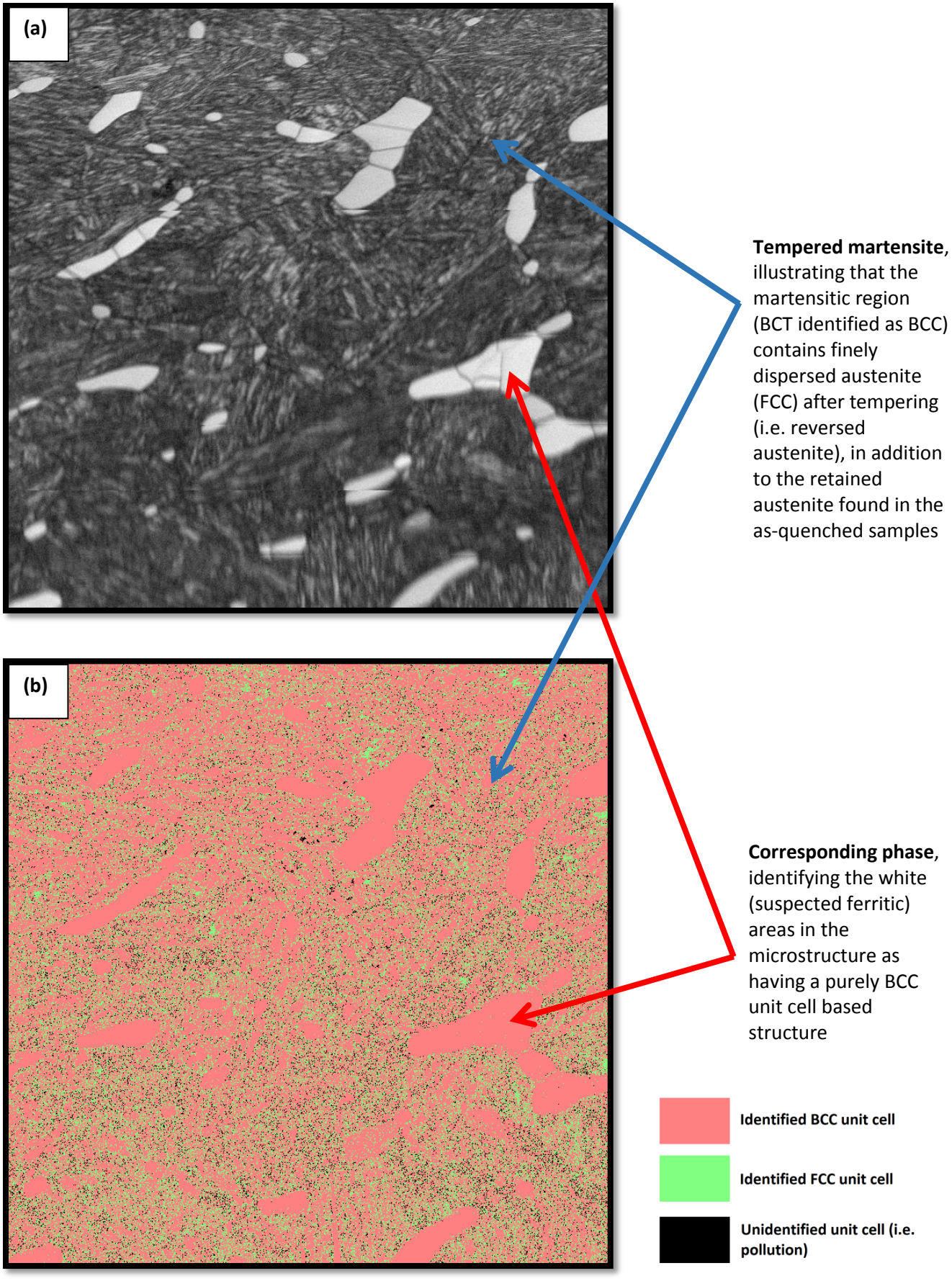

Figure 4.16 – EBSD scan of A20T, illustrating the identified unit cells in the material crystal structure

4.4.3 Heat treatment effect on general grain size

The use of EBSD is often applicable when estimating the average grain size of a polycrystalline sample. However, the method is far from usable when evaluating a material consisting fully or partly of martensitic or bainitic crystalline structures. The lathe shape and grain orientation of such structures infer a severe constraint on the use of such analysis, seeing as it is based on volume-based orientation; the plate-like structures of martensite and bainite cause this restriction in current analysis software.

Therefore, traditional cross-section analysis was performed in order to create an estimate of average grain sizes. Given the contrast quality of Marble's etch, one can separate martensite and ferrite from a general cross section. Marble's etch causes one to be able to identify the previous γ-γ/γ-δ[see footnote 5] grain boundaries using general image analysis software. Thus, the change in martensitic grain size is determined by using the prior austenite grain boundaries. The change in grain size was evaluated from the AT-samples, given that hardening at 1000 °C followed by tempering is the standardized heat treatment used at NOMAC. 5 images – each measuring an area of $1.2 \cdot 10^5$ µm^2 – were used as the basis for this analysis, yielding a total analysis area of $6.0 \cdot 10^5$ µm^2. The image analysis software differentiated between the martensitic (dark) and ferritic (light) areas of the cross-section. The average grain size diameter was calculated manually, using the scale on the optical microscopy images. The use of an average diameter may yield low values for long, thin grains. Note that the grain size was evaluated using cross-sections; the true average grain sizes may differ from the results presented. A total mean for each sample was then calculated, and the results are presented numerically in Table 4.2, and graphically in Figure 4.17.

Table 4.2 – Average martensitic/ferritic grain diameters in samples A1T, A2T A5T, A10T and A20T

	Average grain diameters	
	Martensite	**Ferrite**
A1T	36.3 µm	18.2 µm
A2T	36.9 µm	17.4 µm
A5T	41.8 µm	17.1 µm
A10T	52.7 µm	18.6 µm
A20T	67.6 µm	19.4 µm

[5] γ = austenite (γ-iron) / δ = δ-ferrite (δ-iron)

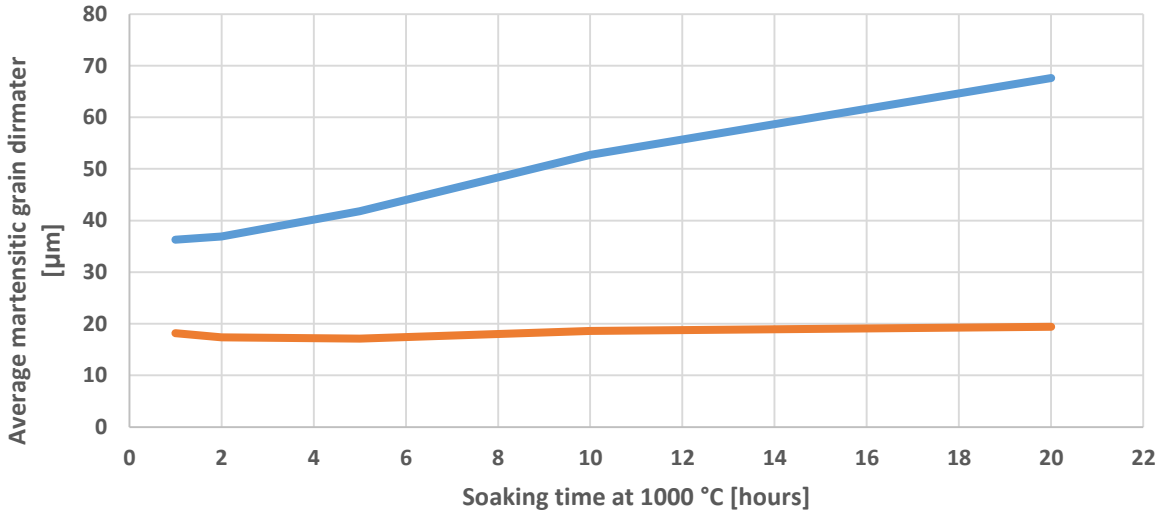

Figure 4.17 – Graphical presentation of average martensitic (blue) and ferritic (red) grain diameters for AT-samples

The average grain diameters cannot be viewed as the definite true values, due to the use of two-dimensional cross-sections. The average grain size for the martensitic grains appear to undergo an exponential rate of growth, proportional to the soaking time at hardening temperature. The average ferritic grain diameters appear to be unaffected by the heat treatment. However, the ferritic content seems to dominantly take the form of long, stretched grains, thus yielding low average diameter values.

Figure 4.18 illustrates examples of how the different grains – i.e. δ-ferrite and prior austenite boundaries – were identified. The lines separating the grains in Figure 4.18 are for illustrational purposes only, and are not as exact as the ones used in the actual analysis (performed using Adobe Photoshop® CC 6, Edge Animate software bundle).

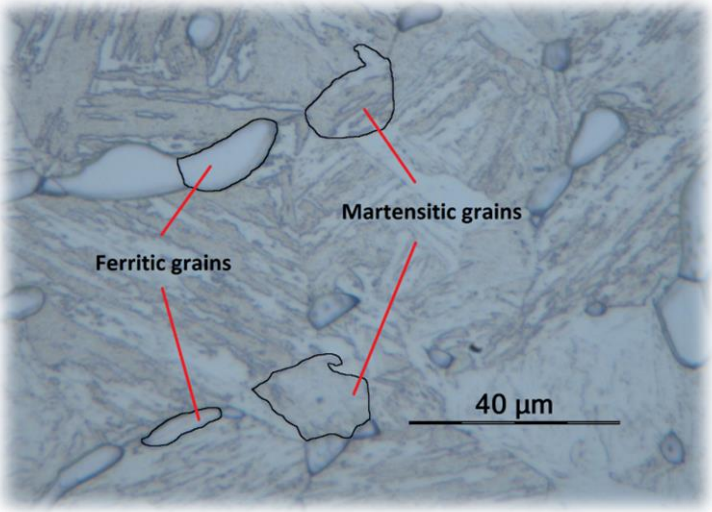

Figure 4.18 – Sample A1T: Simplified identification of ferritic and martensitic (prior austenitic) grains, used to measure the change in grain diameter

4.4.4 Estimation of phase fractions

The principle of cross-section analysis was also performed on samples A1T, A2T, A5T, A10T and A20T in order to provide a somewhat reliable estimate of the fractions of phases that were present. Adobe Photoshop® CC 6 was used for this analysis. There were no noticeable precipitations in the microstructure. Therefore, this analysis only differentiated between martensite and ferrite. Note that the numbers are purely estimates, based on the analyzed cross-sectional areas. The true phase fractions may differ substantially from the results collected from the relevant areas.

The measurements were performed on 5 micrographic images from each sample, totaling an area of $6.0 \cdot 10^5$ µm^2. The results are presented in Figure 4.19 below. The fractions are rounded to two significant figures, due to the error margin in the analysis. The fractions are calculated as follows, where PF equals Phase Fraction (and is unitless):

$$PF_{ferrite} = \frac{\sum Surface\ area\ identified\ as\ ferritic\ [\mu m^2]}{Total\ surface\ area\ analyzed\ [\mu m^2]}$$

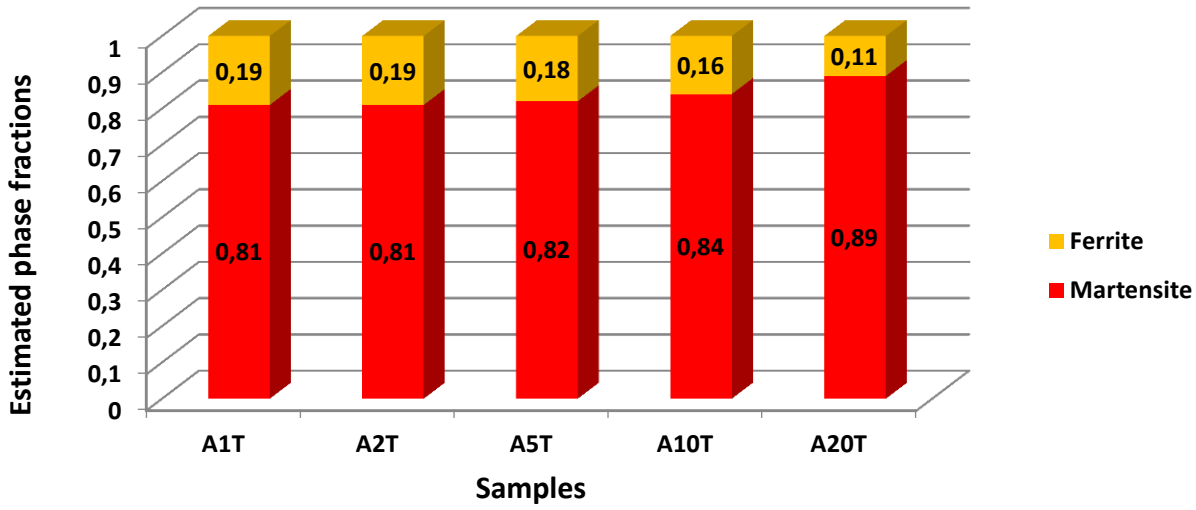

Figure 4.19 – Estimation of martensitic/ferritic phase fractions in AT-samples

Although the numbers are estimates, the analyzed cross-sectional areas show a clear increase in martensitic phase fractions, and a corresponding decrease in ferritic phase fractions. This change in morphology may have impacted the mechanical properties – simultaneously with other factors – and will be discussed in more detail in section 5.4

4.5 Control sets (core temperatures)

As mentioned in section 3.3, all heat treatments were performed in parallel with a dummy set of samples, in order to verify the heating rate of the specimen cores. The dummy set consisted of one 20 mm x 20 mm x 180 mm rod, and one 12 mm x 12 x 180 mm rod. A center bore – measuring 4 mm in diameter – was drilled, running 95 mm from one end. Thermocouples were inserted in the samples, and spot-welded in the insertion end. This ensured that no air could penetrate the core cavity. The thermocouples were connected to separate Ehlm V temperature loggers. The thermometer logged the spot temperature in the thermocouple with 10 second intervals. The dummy set was inserted in the furnace chamber simultaneously as the control sample. The furnace chamber held the relevant temperature at the time of specimen insertion, i.e. 1000 °C for A-samples, and 1030 °C for H-samples. The time it took for the dummy set to reach – and hold a stable core temperature for 60 seconds – is shown in Table 4.3 below. All durations are rounded to nearest 10 s.

Table 4.3 – Duration of heating until stable core temperature for all hardening processes

Treatment code	**Core heating time**	
	Large dummy sample *20 mm x 20 mm x 185 mm*	Small dummy sample *12 mm x 12 mm x 185 mm*
A1	13 min 20 s	8 min 50 s
A2	13 min 40 s	8 min 40 s
A5	14 min 0 s	9 min 20 s
A10	13 min 30 s	9 min 10 s
A20	13 min 30 s	9 min 20 s
A1T	14 min 10 s	8 min 30 s
A2T	14 min 0 s	8 min 50 s
A5T	13 min 40 s	9 min 0 s
A10T	14 min 50 s	9 min 0 s
A20T	14 min 20 s	9 min 0 s
H1	13 min 50 s	8 min 50 s
H2	14 min 10 s	9 min 20 s
H5	13 min 40 s	9 min 50 s
H10	14 min 50 s	9 min 40 s
H20	14 min 10 s	8 min 50 s
H1T	14 min 20 s	8 min 30 s
H2T	14 min 20 s	8 min 40 s
H5T	13 min 50 s	8 min 40 s
H10T	13 min 40 s	9 min 10 s
H20T	14 min 0 s	9 min 20 s

4.6 Correlation of data sets

Figure 4.20 below shows some correlation graphs for the mechanical properties collected from the 20 heat treatments. Soaking time is on the X-axis, while mechanical properties are on the Y-axis. From statistics, there is a dictum stating that *correlation does not imply causation*, where the meaning is that one cannot use a correlation to infer a causal relationship between the variables. However, this dictum does not exclude the possibility that a correlation indicates a possible existence of causal relations (Hagen, 2010). The different correlation sets are used in this section to possibly verify or reject any indication of whether or not the soaking time shows any tendency to correlate with the mechanical properties. The properties shown are from the AT-samples (i.e. samples hardened at 1000 °C and tempered at 560 °C for 8 hours).

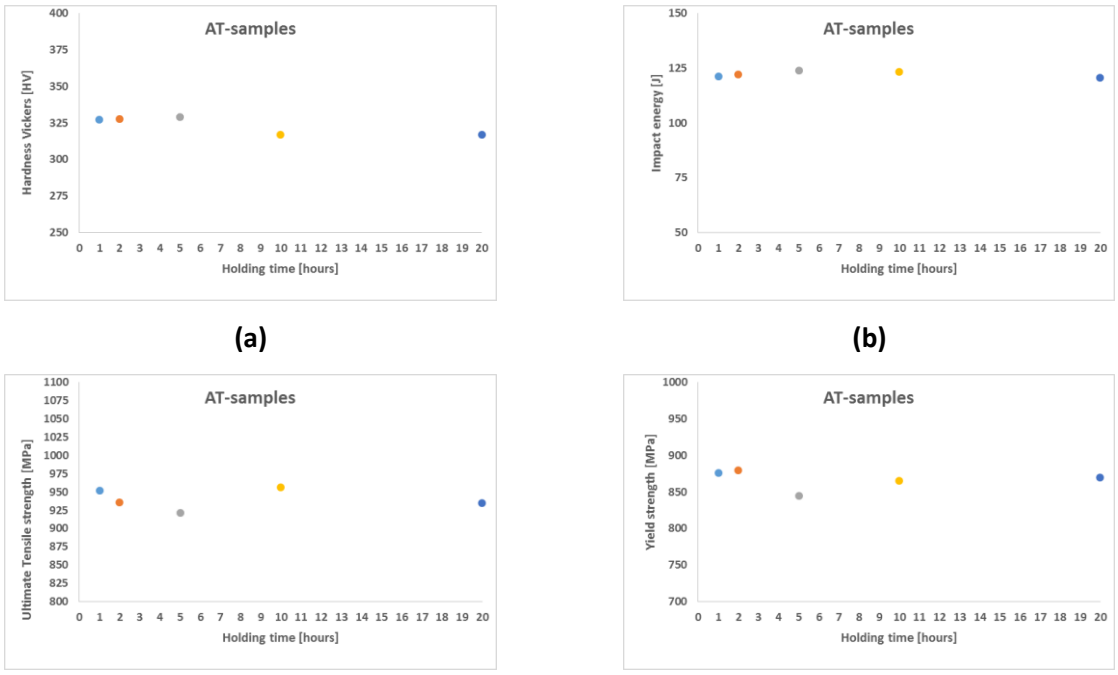

Figure 4.20 – Correlation of soaking times and (a) hardness, (b) impact energy, (c) ultimate tensile strength and (d) yield strength for AT-samples

None of the data sets indicate any noticeable correlation between the soaking time during hardening and the relevant mechanical properties. The correlation graphs for sample sets A, H and HT are presented in Appendix E, and indicate the same results as for the AT-samples. Note that this does *not* automatically imply that the soaking time has no any effect on mechanical properties, only that there is no noticeable correlation (i.e. correlation coefficient ≈ 0)

5. Discussion

5.1 Research assumptions and/or limitations

Overall, the experimental and analytical methods utilized in this thesis were based on a set of assumptions and/or limitations. This was done to ensure that the quality of the data is properly maintained, and to ensure the verifiability and the reproducibility of the experiments. The assumptions and limitations described in the following section are to avoid confusion regarding the contents and postulations that formed the basis of the thesis. In regards to the experiments and analysis performed, the following is assumed to be true:

- The provided chemical composition for the material is the true composition for the material as a whole, and forms the baseline for the composition of alloy elements
- The temperatures registered in the furnace chamber during testing, and subsequently from the dummy samples, are the true temperatures at the given times
- Slight variations in the time used to remove specimens from the furnace chamber did not affect the material properties significantly
- Measurements given by other calibrated equipment are true values[6]
- Averages of collected mechanical properties are representative for the samples[7]

The thesis is also performed on the basis of the following limitations:

- The quantity of material to be analyzed was restricted; the quantity defined the amount of test specimens produced from each heat treatment. Said amount is believed to be statistically accurate as a sample
- Analysis software utilized for EDS and EBSD computed results at a limited rate; the results provided by said analysis is for all intents and purposes believed to be genuine

[6] There are valid reasons for suspecting that the equipment used to measure the impact energy provides non-valid data. This is discussed in further detail in section 5.2.1

[7] The collected Charpy-V impact values presented in this thesis is not comparable to those normally found when analyzing S165M at -20 °C, which are higher than the average values found in this thesis. The main topic of this thesis is to evaluate if the alloy experiences any changes in mechanical properties when the soaking time is varied. Thus, the real value is not as significant as any occurrence of change in the properties

5.2 Quantitative results

The quantitative results collected included (but was not limited to) yield strength, ultimate tensile strength, Charpy-V impact energy, hardness, elongation, contraction, modulus of elasticity plus various fractions and compositions. Few of these quantities change noticeably, even with a high increase in soaking time. It is postulated that the constant mechanical properties is a sum function of the subsequent changes to the morphology for longer soaking times. This is discussed in more detail in later section.

The displayed properties show a high level of consistency when confined to specimen groups (i.e. A, AT, H and HT). Most of the changes between specimen groups are to be expected, i.e. the drop in hardness for tempered samples when compared to their as-quenched counterparts. However, there is no evidence that a variation in the soaking times at the hardening temperatures has any noticeable effect on mechanical properties such as yield strength, ultimate tensile strength and hardness.

5.2.1 Charpy-V impact energy

The measured Charpy-V impact energy values ranged from 105.1 J (A20) to 132.1 J (H20), as seen in Table 4.1. Although the difference from the highest to the lowest exceeds 25 J, the average of the total number of tests equal 122 J with a standard deviation of 6 J. 75 % of the data points lie within 1σ of the average, and 95 % of the data points lie within 2σ.

From section 4.6, we see that the variation in soaking times seems to have no correlation with the impact energies of the samples. This is valid for both the as-quenched and the tempered samples. However, this is not the expected values for impact energy when comparing as-quenched samples to tempered samples. Normally, tempering is performed in order to increase the ductility of a material. This occurs due to the removal of grain boundary strains and dislocations (Bhadeshia & Honeycombe, 2006). The tempered samples seem to provide – on average – the same impact energy values as those that are as-quenched. When primarily austenitic before quenching, the resulting micro-structure is mostly martensitic. The microstructure analysis of the as-quenched samples – both for hardening at 1000 °C and 1030 °C – indicate that the majority of the phase composition is martensitic. This would imply a fairly brittle microstructure, since as-quenched martensite normally is very brittle (Callister & Rethwisch, 2011). No noticeable increase in ductility is registered. However, it has been discussed with metallurgists and material engineers at NOMAC that this may be due to lack of calibration of the testing apparatus.

5.2.2 Hardness testing

The material hardness was measured using Hardness Vickers. The Hardness Vickers test normally tests areas ranging from 10000 μm^2 – 40000 μm^2, and is often characterized as *microhardness*. It is applicable in order to gauge the hardness of smaller fractions of the material sections (i.e. the hardness of specific phases). Although some standards present conversion tables between Hardness Vickers and Hardness Brinell[8], the accuracies of these conversions are limited. This is because the standardized tables are based on plain carbon and/or low-alloy steels.

Hardness Vickers – unit HV – measures hardness by applying a standardized diamond pyramid into the sample, and calculating the hardness using the diagonals of the resulting indentation. The applied load was 10 kg, and the load duration was 10 s. The as-quenched samples yielded Hardness Vickers values in the range of 346 HV – 350 HV for a hardening temperature of 1000 °C, and values in the range of 342 HV – 354 HV for a hardening temperature of 1030 °C. The tempered samples yielded hardness values that were lower than the as-quenched samples. This was to be expected, seeing that the results of a tempering process is to relieve stresses and embrittlement from the structure, yielding a material less resistant to plastic deformation (Hibbeler, 2008). The tempered samples produced hardness values that were 22 – 29 HV lower than their as-quenched counterparts (i.e. when comparing samples with equal soaking times, for example A5 and A5T).

The collected HV values are remarkably consistent, and there are no indications that the HV values have any correlation with the soaking time at the two analyzed hardening temperatures. However, this does not mean that any morphological changes occur that does not impact the hardness. This is discussed in greater detail in section 5.4. Also, even though the change in hardness values were to be expected, the HV values dropped by a factor that was lower than what is expected for tempered low-carbon martensitic ferritic steels. It is suspected that the tempering temperature plays a critical role in the development of the hardness values. The Holloman-Jaffe parameter presented in section 2.5.3 is very sensitive for this alloy composition, ranging from 15.7 – 18.2 for the tempering temperature interval of 480 °C – 600 °C (Hollomon & Jaffe, 1947). This indicates that a higher tempering temperature would yield a greater drop in hardness for the tempered samples.

[8] Single Hardness Brinell tests – unit HB – were performed on all 20 heat treatments. The individual values are found in Appendix G. The HB-values are not included in the discussion, as it only validated the consistency of the material hardness. Thus, the discussion focuses on discussing Hardness Vickers values. This was determined after discussing results with NOMAC (att. Håkon Jørgensen).

5.2.3 Validity of data (standard deviation)

Standard deviation is, from the field of statistics, a useful tool to quantify the amount of variation within a specific data set. A standard deviation close to 0 indicates that the data points tend to be very close to the average value of said data set, while a high standard deviation value indicates that the data points are spread more from the average. The numerical value of the standard deviation is always measured against the average, i.e. a data set with an average of 10 and a standard deviation of 8 has a far higher data spread than that of a data set with an average of 100 and a standard deviation of 12.

From the quantitative results (Table 4.1) it is clear that the samples provided data sets with low standard deviation values, relative to the measurement. For sample sets with 20 individual measurements (i.e. hardness testing), this is to be expected if the equipment is properly calibrated and the methodic is followed consistently. However, an equally low level in the standard deviation values for those samples with only 2 individual measurements (i.e. tensile stress testing) indicates that the data is either a) highly reliable, or b) subject to a random occurrence, causing similarly equal results. Given the fact that the standard deviation for all tensile stress test measurements – including yield point and ultimate tensile strength – was consistently below 1.0 % of the average values, it is fair to claim that the quantitative data collected has a high level of validity. Therefore, the tensile stress test results are deemed to be reliable.

5.3 Microstructure analysis

5.3.1 Effect of hardening temperatures (1000 °C and 1030 °C) on general microstructure

The resulting microstructures of the two hardening temperatures are very comparable when the samples are exposed to equally long soaking times. For example, the microstructure of sample A1 is comparable to that of sample H1, as seen in Figure 5.1. The microstructure of sample A20 is comparable to that of H20, as seen in Figure 5.2. Tempered samples (A1T VS. H1T and A20T VS. H20T) are also included in the figures, and show the same tendency.

The orientation of the δ-ferrite seem to be of a random nature, and not dependent on the hardening temperature. There is no indication that the ferrite aligns in a uniaxial direction when exposed to longer soaking times during hardening, or during tempering. As examined in equivalent low-carbon alloys (Kokawa, Kuwana, & Yamamoto, 1989), the lacy and vermicular morphologies of the δ-ferrite co-exist. These morphologies are the most thermodynamically stable at room temperature for δ-ferrite. The coloring of the micrographs is not related to the microstructure, but the parameters used in the light microscope to obtain the highest possible resolution/contrast for the different samples.

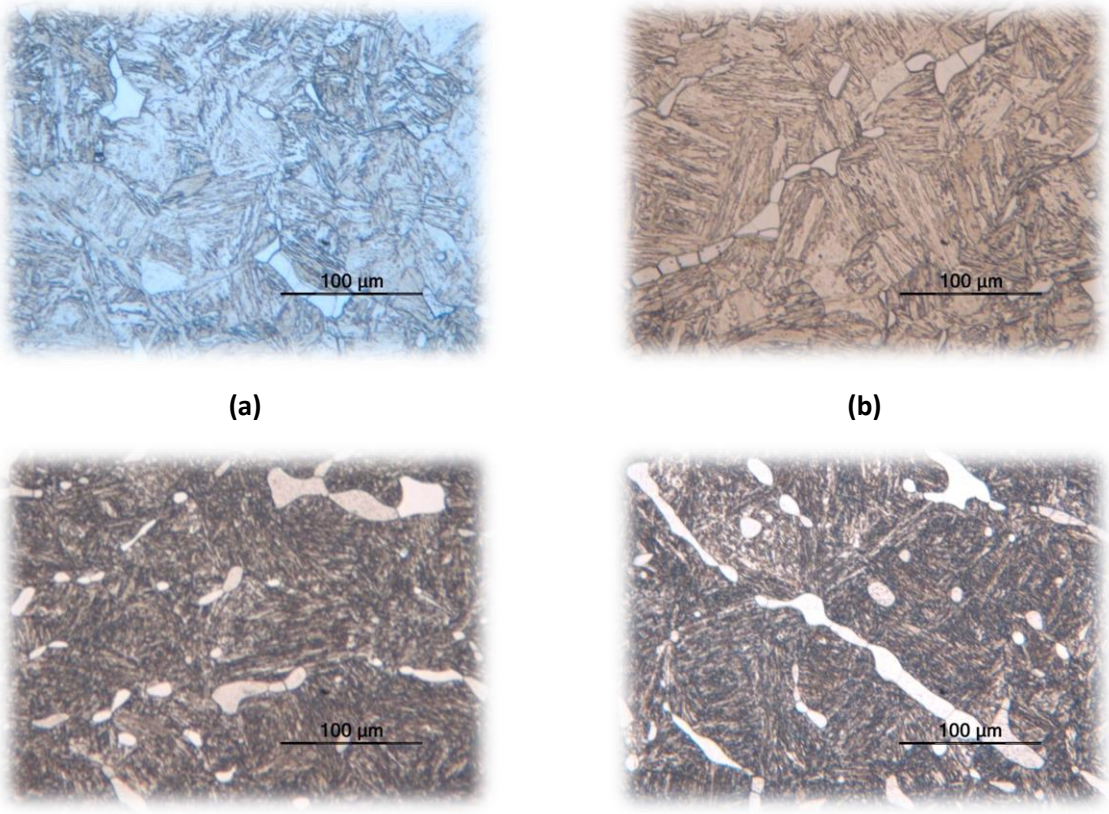

(a) **(b)**

(c) **(d)**

Figure 5.1 – Comparison of microstructures at 20X magnification, showing samples (a) A1, (b) H1, (c) A1T and (d) H1T

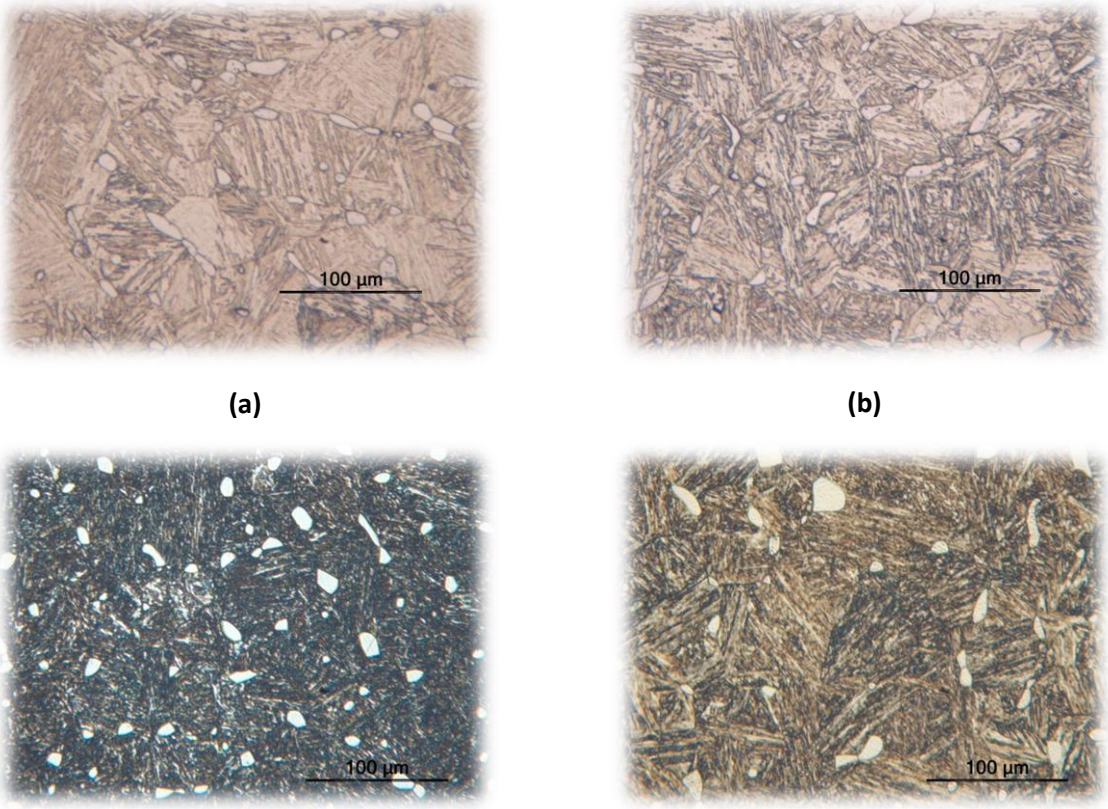

Figure 5.2 – Comparison of microstructures at 20X magnification, showing samples (a) A20, (b) H20, (c) A20T and (d) H20T

From the microstructural analysis, there are no results indicating that hardening at 1000 °C yields a different microstructure than when hardening at 1030 °C.

The figures seem to indicate that the ferrite content decreases when the material is exposed to longer soaking times, which is in thread with the analysis performed on cross-sectional areas. This is discussed in more detail in section 5.3.2.

The ferritic grains also experience a shape-change, possibly related to the soaking times. The ferritic grains seem to evolve from lacy/vermicular grains to globular grains. This may have impacted the original forging characteristics of the microstructure. Further analysis is offered in section 5.3.4.

5.3.2 Effect of soaking time on ferrite content

As presented in section 4.4.4, the ferrite content in the microstructures decreases when the soaking times increase. This indicates that the ferrite content has an inverse proportional relationship to the soaking times the samples are exposed to. This decrease in ferrite content is also evident if micrographs from short and long soaking times are compared, as in Figure 5.3.

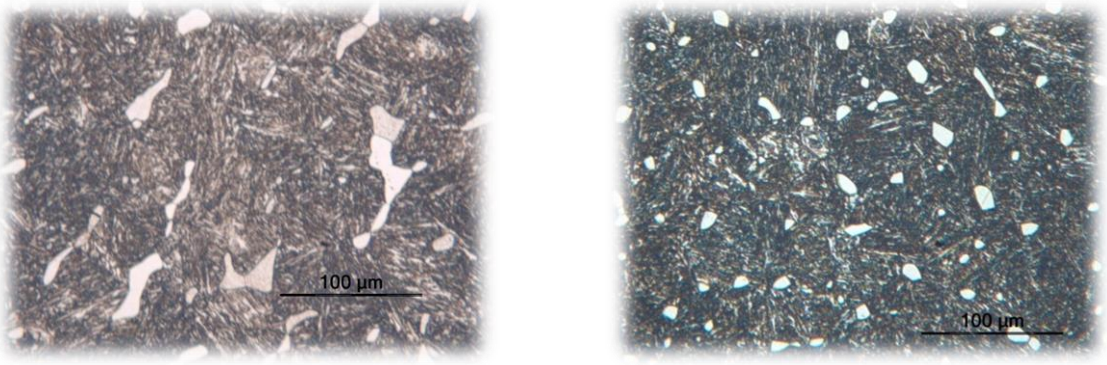

(a) **(b)**

Figure 5.3 – Micrographs at 20X magnification from (a) A1T and (b) A20T. The decrease in ferrite content is evident

Figure 5.4 shows the computed phase diagram for S165M, based on the chemical composition of charge A19606 (see Table 2.2). The phase diagram is an illustration of the equilibrium state of the material, i.e. if the material is allowed to fully thermodynamically stabilize at given temperatures. The two hardening temperatures 1000 °C and 1030 °C are marked in the figure, illustrating that the composition of S165M is fully austenitic if allowed to reach equilibrium. The longer the soaking time is, the closer the material is able to approach its equilibrium state. The reduction of ferrite content with longer soaking times at hardening temperatures is logical, seeing that the equilibrium states at both of the hardening temperatures is fully austenitic. The increased austenite content causes the subsequent increase in martensite content after quenching.

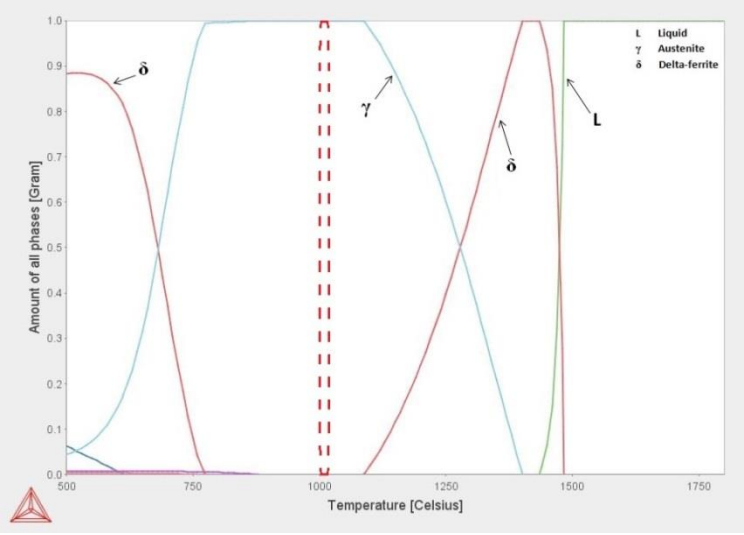

Figure 5.4 – Computed S165M phase diagram, amount of phases VS. temperature. The austenitic phase composition for A and H at equilibrium is marked in red (NOMAC v/ Håkon Jørgensen, 2015)

5.3.3 Longitudinal VS. Transverse microstructure

All of the microstructure analyzed in sections 4.2 and 4.4 are from longitudinal samples, i.e. they are viewed in the cross-section of the tensile stress test rods. In order to establish a basis for the three-dimensional microstructure, transverse samples from A1T and A20T were analyzed. The resulting microscopic images are shown in Figure 5.5, along with the corresponding longitudinal samples.

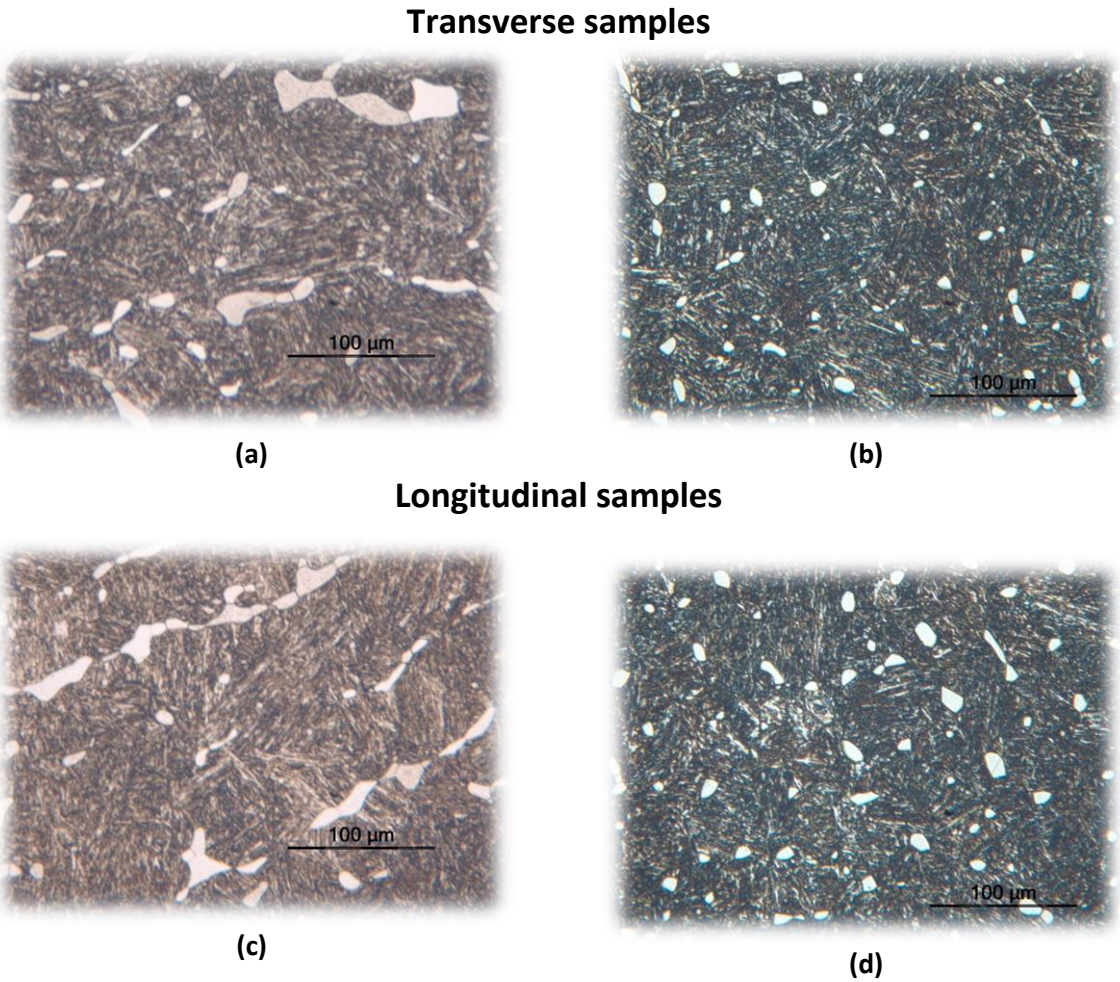

Figure 5.5 – Longitudinal VS. Transverse microstructure in samples A1T and A20T at 20X magnification, where (a) A1T transverse; (b) A20T transverse; (c) A1T longitudinal; (d) A20T longitudinal

The results show that the transverse samples exhibit very similar microstructures to those of the longitudinal samples. This implies that the two-dimensional images created from either of the cross-sections are representative for the three-dimensional microstructure. The images clearly illustrate how the ferrite content decreases in correlation with an increasing soaking time at hardening temperature, as calculated in section 4.4.4. It was suspected that the orientation of the δ-ferrite would change when switching from a longitudinal to a transverse viewing angle. However, these results indicate that the orientation of the ferritic grains is a random function, entirely independent of how the microstructure is observed.

5.3.4 Effects of soaking time on original forged grain structure

Another notable result stemming from the examination of longitudinal VS. transverse samples is the evolution of the ferrite grain shape with the increase soaking times. From the figure, it is evident that the general ferrite grain morphology evolves from the symbiotic lacy/vermicular forms into globular grains. This is in addition to the fraction of the ferrite dissolving and transforming into martensite. The samples hardened for 1 hour seem to retain the stretched ferritic structure one often finds in forged steels. When the soaking time is increased, the effects gained from the forging process are diminished. The ferrite transforms into more stable, globular grains (see Figure 5.5).

During the longer soaking times, the samples are exposed to a larger sum amount of thermal energy. This thermal energy alters the phase composition by increasing and/or decreasing the amount of free energy stored in the crystal structure. This allows the structure to approach its equilibrium state, which consists of less ferrite. This implies that the heat treatment is the sole contributor to the alteration of the material phase composition, and that an increasing soaking time at hardening temperatures may affect the grain distribution of ferrite in the material structure.

The continuous grain flow achieved through forging is a strengthening contributor. However, the results seem to indicate that the reduced grain flow has little to no effect on the material properties. It is worth to note that this change in microstructure cannot be analyzed independently. It is likely that the constant mechanical properties is a sum function of the alterations examined in the morphology of the material by exposing it to prolonged soaking times. The weakening factors are assumed to be the growth of martensitic grains and the loss of continuous grain flow. The strengthening factors are assumed to be the decrease of the ferrite fraction, and the increase of martensite. Together these factors combine and affect the material properties in opposite directions, yielding an average that remains relatively unchanged. This is discussed in further detail in section 5.4.

5.4 Morphologic changes and subsequent effects on material properties

5.4.1 Average martensitic grain diameters VS. Phase fractions of ferrite

There are many factors that contribute when one is evaluating how the general strength and toughness of a material changes. The list includes (but is not limited to) alloy composition, atomic density, lattice structure, crystal morphology, phase distribution and grain size. The latter is often alterable through heat treatment, where one subjects an alloy to thermal energy. This thermal energy may alter the level of free energy within the material structure, causing a rearrangement in the global crystallographic structure and a subsequent change in mechanical properties.

Metallurgic theory illustrates a strong support for the relation between a material grain size and the corresponding material strength that evolves from said size. The Hall-Petch equation[9] is a relevant example of how such a corresponding mathematical relationship has been established (Morris, 2004). The logic behind this connection is simple; the smaller grains a material has, the larger is the total amount of grain boundaries. On these boundaries we often find dislocations and concentrated shear strain, increasing the material ability to resist further deformation. Thus, there is a logical connection behind the grain sizes in the material and the material strength.

The data from the microstructure analysis indicated that the average martensitic (i.e. prior austenitic) grain diameters increased when exposed to corresponding increasing soaking times at hardening temperatures. The grain diameters evolved from 36.3 µm when held at hardening temperature for 1 hour, into 67.6 µm when held at 20 hours. If assuming ceteris paribus, this should have had detrimental effects on the general material strength, seeing as the average grain size increased by over 82 % when comparing the samples hardened for 1 and 20 hours, respectively. However, as seen in sections 4.1 and 4.3, the mechanical properties remain relatively unchanged. This is despite the fact that the growth in grain size occurs. The material properties therefore contradict established theory. This is an indication that other factors play a significant role in terms of altering the mechanical properties.

The distribution and formation of different phases also play an important role in terms of how a material can resist deformation. In ferritic-martensitic steels, the ratio between ferrite and martensite play a substantial role in terms of mechanical properties. For tempered martensitic

[9] $\sigma_y = \sigma_0 + K_y d^{-1/2}$, where σ_y is the yield strength, K_y is the Hall-Petch slope and d is the average grain diameter

ferritic steels, a lower ferrite fraction normally yields better results in terms of tensile strength. At the same time, it normally affects ductility negatively (Pouranvari, 2010). As seen in section 4.4.4, the estimated ferrite fraction based on image analysis decreased with increasing soaking times. The ferrite fractions ranged from approximately 0.19 in the sample soaked for 1 hour at 1000 °C down to as little as 0.11 for the sample soaked for 20 hours at the same temperature. Due to the expected effects of the changing average martensitic grain sizes, it may be possible that the decrease in ferrite content has had a positive effect on the mechanical properties of S165M.

Figure 5.6 illustrates the average martensitic (i.e. prior austenitic) grain diameters and the estimated ferrite content in the respective samples, where the former is marked by a red line and the latter is marked by a black line. The axises are scaled in order to highlight the change in either property. The inverse relationship between the factors is remarkably consistent, and the graphs seem to correlate negatively. It is possible that since these processes seem to have taken place simultaneously, they have enabled the alloy to exhibit consistent material properties; the increase in grain diameters have had a negative effect, but the decrease in ferrite content may have had a positive effect. Note that the horizontal axis is not scaled to represent the factor of time (thus yielding graphs that appear to behave more exponentially than they actually do).

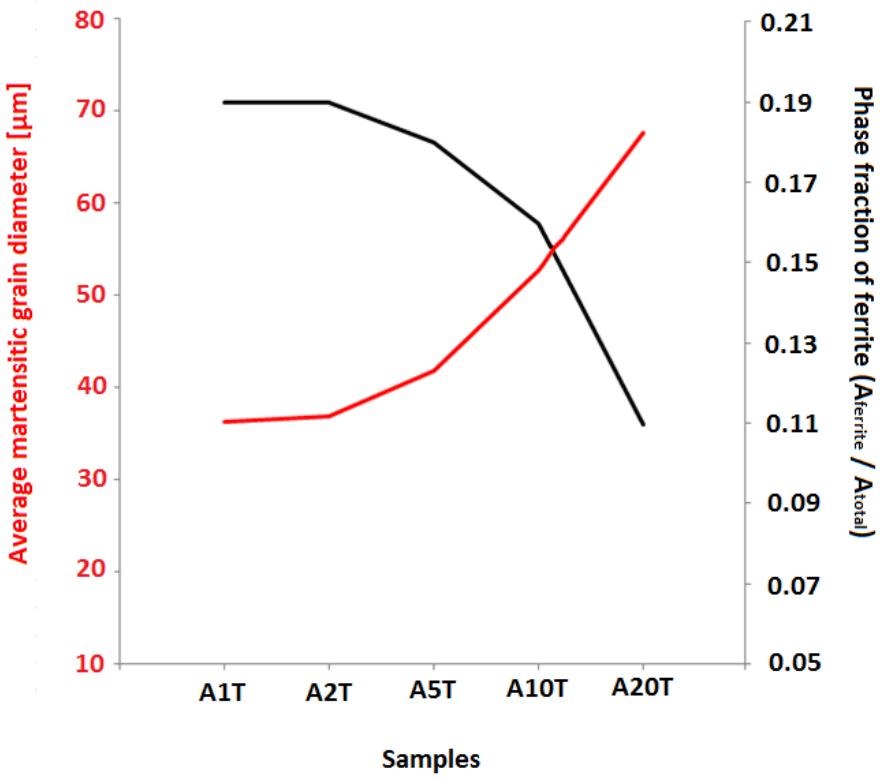

Figure 5.6 – Average martensitic grain diameter (red) and phase fraction of ferrite (black) in AT-samples

5.4.2 Effect of tempering on reversed austenite formation

The EBSD scans of samples A1 and A20T illustrated that the austenite was present in both the as-quenched and tempered samples. Figure 5.7 shows the samples set up side by side for comparison.

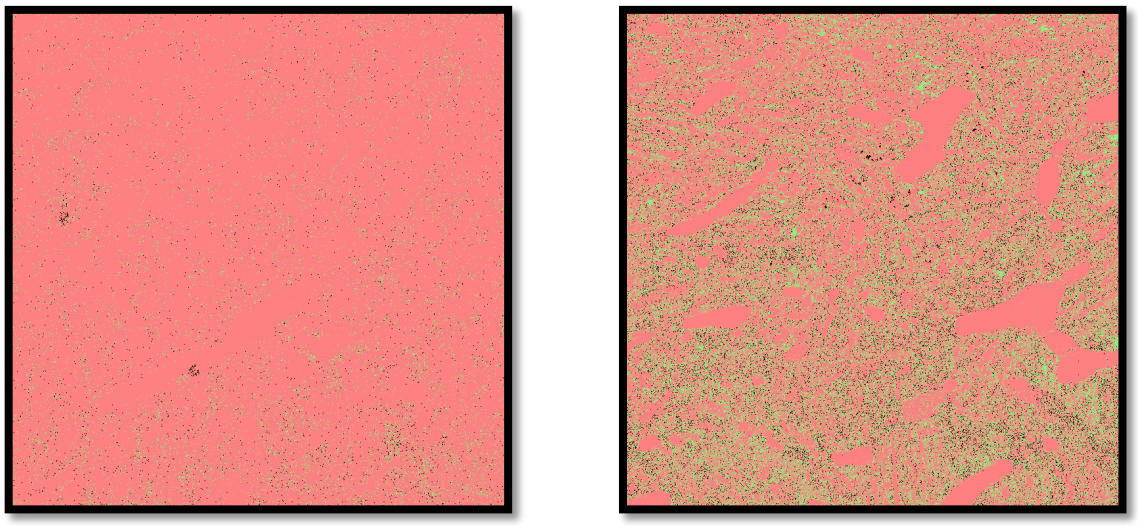

(a) **(b)**

Figure 5.7 – EBSD unit cell identification scan, showing (a) A1 and (b) A20T. The pink pixels correspond to BCC/BCT, and the green pixels correspond to FCC. Black pixels are unidentified (i.e. signal pollution)

The scans show that varying amounts of austenite is present in both samples. In the as-quenched sample (A1), the present austenite is categorized as *retained austenite* (austenite that did not fully transform into martensite during quenching). The tempered sample (A20T) shows a massive increase in austenite in the martensitic structure. The tempered sample consists of a mix between *retained austenite* and *reversed austenite*, where the majority of the present austenite in this sample is of the latter type. Studies have shown that the tempering temperature has a direct effect on the formation on reversed austenite during tempering of martensitic steels (Song, Rong, & Li, 2011). Normally, the formation of reversed austenite starts at 550 °C (i.e. the formation-start temperature). The tempering temperature used in this thesis was consistent at 560 °C. It is believed that it was the tempering process that yielded the formation of reversed austenite, not the hardening process. The amount of formed reversed austenite affects the tensile properties of the material. The effect on the tensile properties is directly proportional to the difference from the formation-start temperature, i.e. that higher tempering temperatures have substantially larger effects on the tensile properties. The difference between the tempering temperature and the formation-start temperature (ΔT) was only 10 °C. It is believed that the reversed austenite had no noticeable effect on the properties other than affecting the decrease in hardness. A larger ΔT could yield a larger effect on tensile properties.

5.5 Method: Weaknesses and improvement proposals

Whenever an experimental method is applied, care must be taken in order for it to be possible to reproduce the gathered results. This thesis relies on numerous experiments with varying elements of accuracy. The key unverified variable is the possibility that testing apparatuses were improperly calibrated. The results in this thesis are based on several measurement devices, which may or may not have been calibrated. However, seeing as the main purpose was to identify any change in mechanical properties and/or morphology, the grade of change was equally – if not more – important than the true values themselves.

For further testing and/or analysis regarding this alloy, it is recommended to pursue the following elements (due to the reasons listed):

- **Microstructural analysis:** Analyze the longitudinal and transverse microstructure in all separate heat treatments, in order to verify the development of the microstructure in all stages
- **EBSD sample examination:** Examine and compare the crystallography for solely as-quenched samples. This will reduce any uncertainty produced by the tempering process.
- **Effect of tempering durations:** Vary the duration the samples are tempered, in order to possibly quantify the optimal duration for the given alloy composition
- **Detailed phase fraction analysis:** Increase the analyzed cross-sectional area, so that the computed phase fraction estimates become more reliable. Also, utilize area calculations instead of average grain diameters. This will increase the reliability of the data
- **Quantification of phases:** The use of SEM-techniques to more accurately quantify the present phases in the alloy is recommended. For this alloy – given the increased presence of austenite in tempered samples – it is recommended that one uses EBSD in order to provide detailed grain volume information
- **Charge variation:** Analyze samples taken from different – but chemically equivalent – charges, in order to verify that it is said composition that is the main factor that affects the general material properties (pre-heat treatment)

This page has intentionally been left blank

6. Conclusion

This thesis focused on examining if the time a martensitic ferritic stainless steel was soaked at the hardening temperature had any effect on the material properties and/or its morphology. Two hardening temperatures were used in this thesis, i.e. 1000 °C and 1030 °C. Samples were soaked for 1, 2, 5, 10 and 20 hours at both hardening temperatures. Both as-quenched and tempered samples were analyzed and compared. Based on the collected data and subsequent analysis, the following general conclusions can be drawn:

- Soaking times up to and including 20 hours at hardening temperature has little to no outwardly evident impact on mechanical properties such as yield strength, ultimate tensile strength, elongation, contraction, hardness and/or ductility. The values stay within what is deemed to be a natural statistical variation, regardless of soaking time
- The use of 1000 °C and 1030 °C as hardening temperatures are deemed to be mutually exclusive in terms of resulting microstructures and mechanical properties. This is given equal soaking times at both temperatures. Neither temperature show signs of carbide precipitation
- Longer soaking times decreases the present ferrite fraction, because it approaches its equilibrium state, where the structure is fully austenitic
- Longer soaking times yield a linear growth of average martensitic (i.e. prior austenitic) grain diameters. The growth of the martensitic grains is believed to be somewhat proportional to the soaking time. The ferritic grains does not experience an equivalent growth, but experience a change in grain form (transformation from an outstretched vermicular to a globular grain structure)
- There seems to be a negative correlation between the average martensitic grain diameters and the ferrite fractions, where the former increases and the latter decreases with longer soaking times. These parallel processes are believed to be the main cause for why the mechanical properties remain unchanged, as they counteract each other
- The martensite in the as-quenched samples contains small amounts of retained austenite. The tempered martensite contains high amounts of reversed austenite. It is not believed that the reversed martensite is the primary cause for the lower mechanical properties in tempered samples, but is believed to aid in reducing the strength and hardness
- The factors by which the morphological changes affect the mechanical properties have yet to be quantified

In relation to the thesis question, it is justifiable to conclude on the following key points:

- **The mechanical properties remain relatively constant, regardless of soaking time. There is not found any direct correlation between increasing/decreasing soaking times and tested mechanical properties**

- **The soaking times at hardening temperatures alters the material morphology. An increased soaking time leads to:**
  - Growth of average martensitic grain diameters (i.e. prior austenitic grain diameters)
  - Reduction in material ferrite fraction (and subsequent growth of martensite fraction)

- **The changes in the morphology negatively correlate. They are believed to produce constant mechanical properties, due to the sum function of the morphological changes**

- **The two tested hardening temperatures do not produce statistically varying mechanical properties and/or morphologies, and are deemed to be mutually exclusive**

List of References

Ahlers, M. (2004). *Revista Matéria*. Hentet fra The Martensitic Transformation: http://www.materia.coppe.ufrj.br/sarra/artigos/artigo10308/

ASM International. (2006). Fundamentals of the Heat Treating of Steel. I A. International, *Practical heat Treating, Second Edition* (ss. 9-26). Ohio: ASM International.

ASTM. (2012). *Standard Hardness Conversion Tables for Metals Relationship Among Brinell Hardness, Vickers Hardness, Rockwell Hardness, Superficial Hardness, Knoop Hardness, Scleroscope Hardness, and Leeb Hardness.* PA: ASTM International.

ASTM. (2014). *ASTM A307-14: Standard Specification for Carbon Steel Bolts, Studs, and Threaded Rod 60000 PSI Tensile Strength.* PA: ASTM International.

ASTM A370. (2014). *ASTM A370-14: Standard Test Methods and Definitions for Mechanical Testing of Steel Products.* PA: ASTM International.

ASTM A370. (2014). *ASTM A370-14: Standard Test Methods and Definitions for Mechanical Testing of Steel Products.* PA: ASTM International.

Bhadeshia, H. K. (2002). *Martensite in Steels.* University of Cambridge - Department of Materials Science & Metallurgy.

Bhadeshia, H., & Honeycombe, R. (2006). *Steels - Microstructure and Properties.* Burlington: Elsevier.

Callister, W. D., & Rethwisch, D. G. (2011). *Materials Science and Engineering.* Hoboken: John Wiley & Sons.

Ceccon, T., Belloli, P., & Ramina, P. (2010). *The magnetic properties of a precipitation hardening and a soft martensitic stainless steel.* Vicenza: Acciaierie Valbrina SpA.

Davis, J. R.; A.I.H. Committee. (1994). *Stainless Steels.* ASTM International.

Dawood, M., Mahallawi, I., Abd El Azim, M., & Koussy, M. (2004). *Thermal aging of 16Cr – 5Ni – 1Mo stainless steel.* Teshrin: Institute of Materials, Minerals and Mining.

Efimenko, L., & Seledzhieva, M. (2000). Calculation of Ferrite Grain Diameters in Steel 08Kh22N6T under Welding Conditions. *Chemical and Petroleum Engineering*.

Hagen, P. C. (2010). *Innføring i Sannsynlighetsregning og Statistikk.* Bø: Cappelen Damm AS.

Hibbeler, R. C. (2008). *Mechanics of Materials.* Singapore: Prentice Hall.

Hollomon, J., & Jaffe, L. (1947). *Ferrous Metallurgical Design.* John Wiley and Sons Inc.

Irving, & Pickering. (1960). *Journal of the Iron and Steel Institute*.

Jacques, P., Allain, S., Bouaziz, O., Hance, B., Huang, J., Iza-Mendia, A., & Kruger, S. (2009). On measurement of retained austenite in multiphase TRIP steels — results of blind round robin test involving six different techniques. *Materials Science and Technology*, 20-31.

Kokawa, H., Kuwana, T., & Yamamoto, A. (1989). *Crystallographic Characteristics of Delta-Ferrite Transformations in a 304L Weld Metal at Elevated Temperatures.* Sendai: Department of Materials Processing, Tohoku University.

Krishnan, S., Dumbre, J., Bhatt, S., Akinlabi, E., & Ramalingam, R. (2013). Effect of Crystallographic Orientation on the Pitting Corrosion Resistance of Laser Surface Melted AISI 304L Austenitic Stainless Steel. *International Journal of Mechanical, Aerospace, Industrial and Mechatronics Engineering*, 239-242.

Maalekian, M. (2007). *The Effects of Alloyin Elements on Steels.* Graz: Institut für Werkstoffkunde, Schweißtechnik und Spanlose Formgebungsverfahren.

McConnel, C. R., Brue, S. L., & Flynn, S. M. (2012). *Microeconomics - Principles, Problems and Policies.* New York: McGraw-Hill.

Morris, J. (2004). *The Influence of Grain Size on the Mechanical Properties of Steel.* Berkeley, CA: Department of Materials Science and Engineering.

NOMAC v/ Håkon Jørgensen. (2015, May). Phase Diagram. Jørpeland: NOMAC.

NOMAC v/ Håkon Jørgensen. (2015, June). Scheil Diagram. Jørpeland: NOMAC (at.. Håkon Jørgensen).

Palizdar, Y., Cochrane, R. C., Brydson, R., Leary, R., & Scott, A. J. (2010). Accurate analysis of EBSD data for phase identification. *Journal of Physics*.

Porter, D. A., & Easterling, K. E. (1992). *Phase Transformations in Metals and Alloys (2nd ed.).* Chapman & Hall.

Pouranvari, M. (2010). *Tensile Strength and Ductility of Ferrite-Martensite Dual Phase Steels.* Dezful: Association of Metallurgical Engineers of Serbia.

Russ, J. C. (1984). *Fundamentals of Energy Dispersive X-ray Analysis.* London: Butterworths.

Sagalevich, Y., Potak, Y., & Sachkov, V. (1970). *The effect of delta-ferrite on the properties of low-carbon martensite stainless steels.* Moscow: Tsentral'nyy Nauchno-Issledovatel'skiy Institutit Chernoy Metallurgii.

Scheil, E. (1942). *Z. Metallk.*

Schwarzer, D. R. (2013). *Orientation Microscopy and Ion Backscattering*. Hentet fra Crystal Texture: http://www.crystaltexture.com/ibp_1.htm

Shlyakman, B. M., Tampolskii, O. N., & Ratushev, D. V. (2010, September). A Method for Determining Constant C in the Hollomon Parameter. *Metallovedenie i Termicheskaya Obrabotka Metallov*, ss. 48-51.

SIFCO. (2012). When Only a Hammer Will Do. Hentet fra http://www.sifco100.com/when-only-a-hammer-will-do/+&cd=3&hl=no&ct=clnk&gl=no

Song, Y. L., Rong, L., & Li, Y. (2011). The influence of tempering temperature on the reversed austenite formation and tensile properties in Fe–13%Cr–4%Ni–Mo low carbon martensite stainless steels. *Materials Science and Engineering A*, 4075-4079.

Song, Y., Li, X., Rong, L., Ping, D., Yin, F., & Li, Y. (2010). Formation of the reversed austenite during intercritical tempering in a Fe–13%Cr–4%Ni–Mo martensitic stainless steel. *Materials Letters*, 1411-1414.

UiS v/ Ingunn Oddsen. (2015, May). SEM analysis results of X4CrNiMo 16-5-1. Stavanger, Rogaland, Norway.

Wang, D., Chen, C.-W., Dalton, J. C., Yang, F., Sharghi-Moshtaghin, R., Kahn, H., . . . Heuer, A. (2014). Interstitial supersaturation in delta ferrite in stainless steels. *ScienceDirect*.

Winston, A. (2012). *Management Science Modeling.* Singapore: South-Western CENGAGE Learning.

This page has intentionally been left blank

Appendix

Appendix A – Data sheet (S165M)

NOMAC

Rev. 2

Quality no.	Quality group	Quality
2060	STAINLESS STEEL FOR FORGING	S165M

Chemical analysis:

	C	Si	Mn	S	P	Cr	Ni	Mo	N
min						15,0	4,50	0,80	0,020
max	0,05	1,00	1,50	0,015	0,035	17,0	6,00	1,50	

Corresponding standards:

EN 10088 (X4CrNiMo16-5-1)	M.no. 1.4418
SEW 400 (X 4 CrNiMo 16 5)	W.nr. 1.4418
NS (replaced by EN standard)	14 240
SS (replaced by EN standard)	14 23 87

Applications: S165M is a martensitic/ferritic stainless steel with excellent mechanical properties and ductility. General areas of application are propellers, shafts, spindels, bolts etc.

Minimum mechanical properties:

Dimension	Yield strength Rp0.2 [MPa]	Tensile strength Rm [MPa]	Fracture elongation A [%]	Charpy-V impact energy CVN [J]
< 250 mm	700	900-1100	14	42 (-20 °C)

Heat treatment: Normalized at 1000 °C and cooled in air, followed by tempering at 560-580 °C and air cooling. The tempering temperature may be adjusted within this temperature range to obtain the desired mechanical properties.

Weldability: The weldability of S165M is good.

Specific weight: 7.7 g/cm³

Coefficent of thermal expansion:

20-100 °C:	12.0·10-6 K-1
20-300 °C:	12.5·10-6 K-1
20-500 °C:	13.0·10-6 K-1

EØG 04.11.2003

Appendix B – Material certificate for charge A19606

Scana
SCANA STEEL STAVANGER AS
Scana Steel Stavanger as
4100 Jørpeland, Norway
Country of origin: Norway

INSPECTION CERTIFICATE/
INSPEKTION ZERTIFIKAT
EN 10204 - 3.1

Customer / *Besteller*	Date/*Datum*	Cert.no./*Zeugnis Nr.*
	Our order no./ *Unsere Auftrags- Nr.*	Our work-order no./
	Customer order no/ *Bestellungs- Nr.*	
Spesification/*Spezifikation:*	Certified goods/ *Gegenstand*	
Marking/*Kennzeichnung:*	Grade / *Werkstoff. Nr.*	

CERTIFIED GOODS / *ZERTIFIERTES GUT*

Test no./ *Probe Nr.*	Number / *Stück*	Weight/ *Gewicht (kg)*	Dimension	Heat treatment / *Wärmebehandlung*	Process/ *Erschmelzungsart*	Reduction grade/ *Verschmiedungsgrad.*	Charge no./ *Schmelze*
T12045	1	518		Hardened 1000°C;Water Tempered 560°C;Air	Forged E/ AOD	5,90:1	A19606

CHEMICAL COMPOSITION / *CHEMISCHE ANALYSE* **SSA Quality name: 2060 S165M**

C	Si	Mn	S	P	Cr	Ni	Mo	Cu	Al	Ti	N									
0,037	0,40	0,60	0,001	0,024	16,11	4,94	0,97	0,170	0,005	0,001	0,033									

MECHANICAL PROPERTIES (L=Longitudinal, T=Transverse) ***MECHANISCHE EIGENSCHAFTEN (L=längs, T=Quer)***

Test L/T Probe L/T	Temp.	Yield Strength/ *Streckgrenze*		Tensile Strenghth/ *Zugfestig-keit*		Elongation/ *Dehnung*	Red. of area/*Ein-schnürung*	Impact values / *Kerbschlagerbeit* Kv				Temp.	Hardness / *Härte*
	° C	Rp0.2 N/mm2	Rp1.0 N/mm2	*Rm N/mm2*	Rp/Rm	A %	z %	J	J	J	Avg.	° C	HB
T	20	841		996		18	45	115	117	112	115	20	293

RESULTS OF OTHER TESTS / *ERGEBNIS ANDERER PROBEN.*

UT and PT -Accepted. Report attached.

We herby declare that the product supplied are in compliance with the order in which test results are supplied.	
Manufacturer's authorized representative:	3.party representative:

Kontrollert av Tungland Scana Steel Stavanger as Quality Control Dept.

Appendix C – Stress VS. Strain curves from raw data

All heat treatments had 2 separate tensile stress tests. Both graphs are indicated in the same diagram for a specific heat treatment.

A1

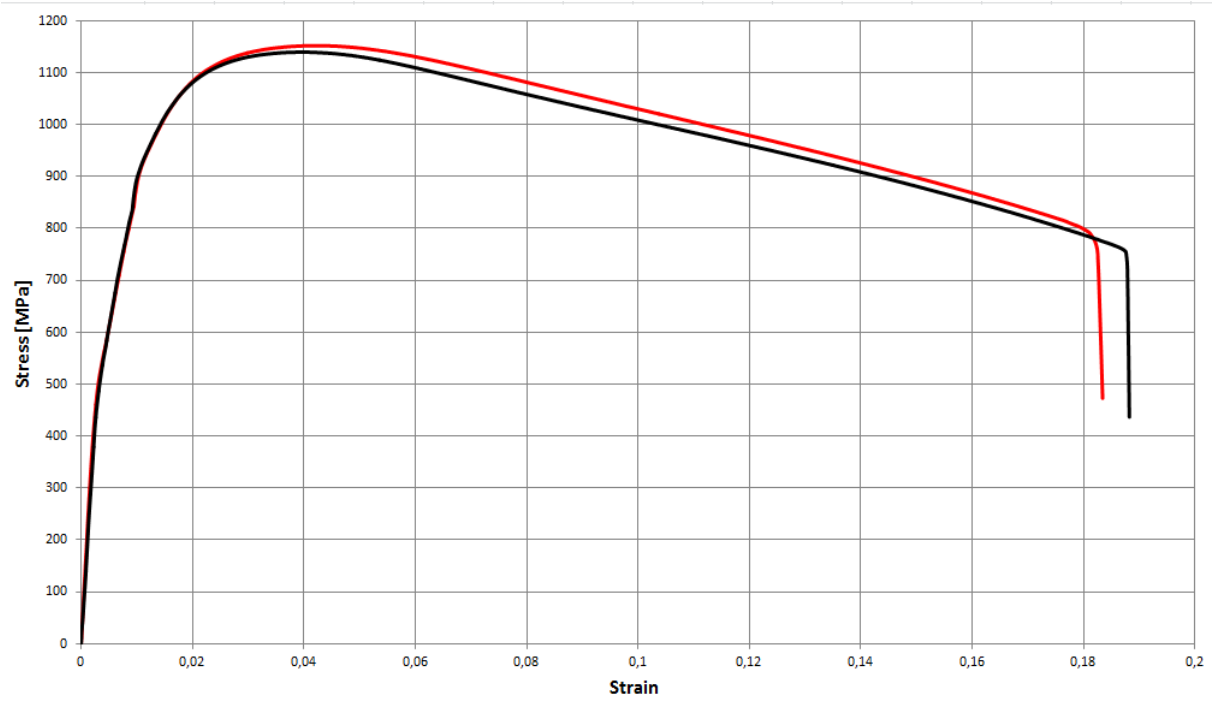

A2

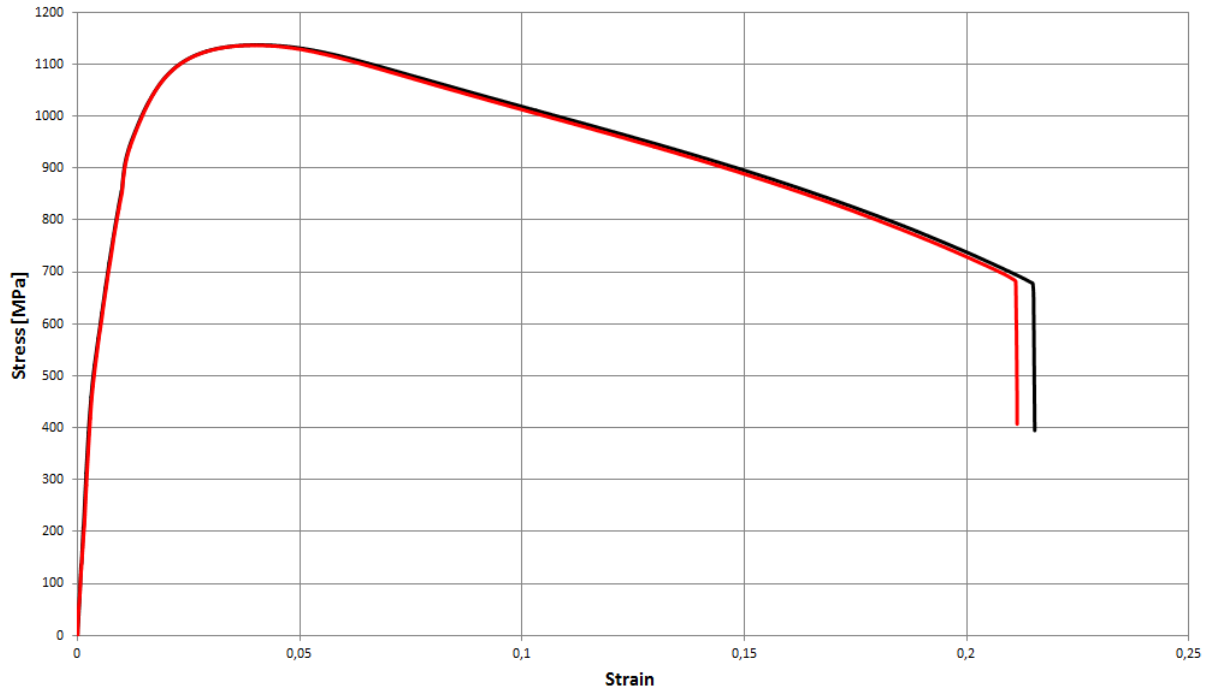

A5

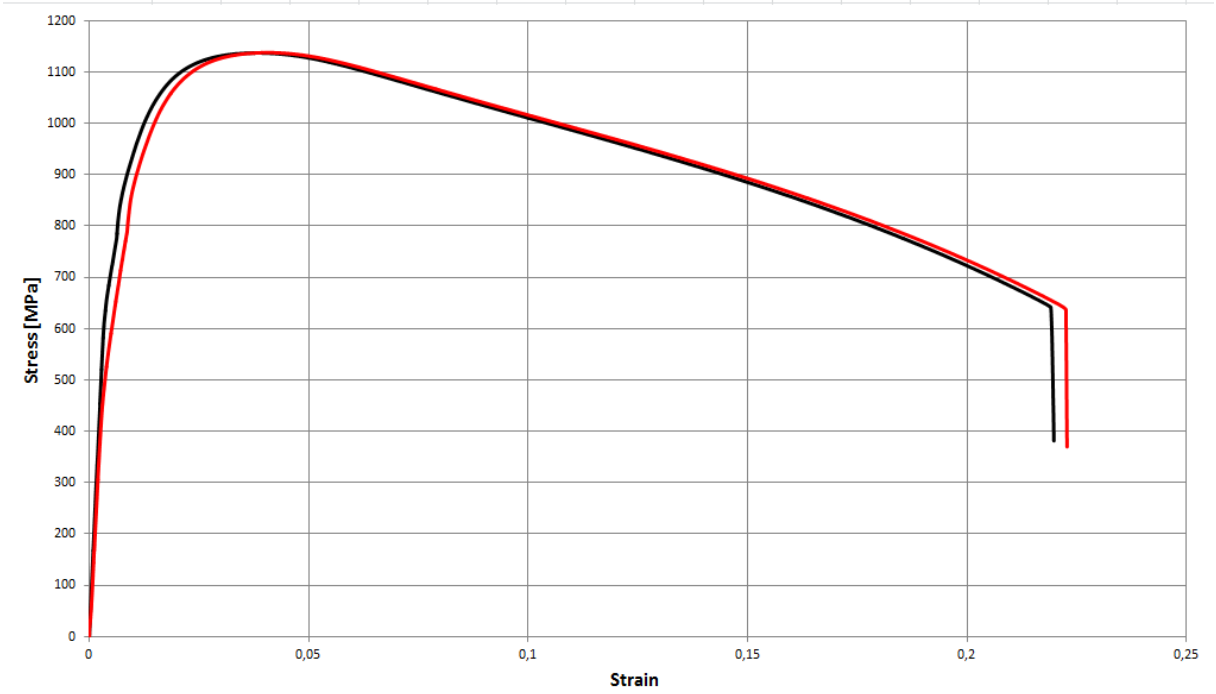
Stress [MPa]
Strain
0
100
200
300
400
500
600
700
800
900
1000
1100
1200
0
0,05
0,1
0,15
0,2
0,25

A10

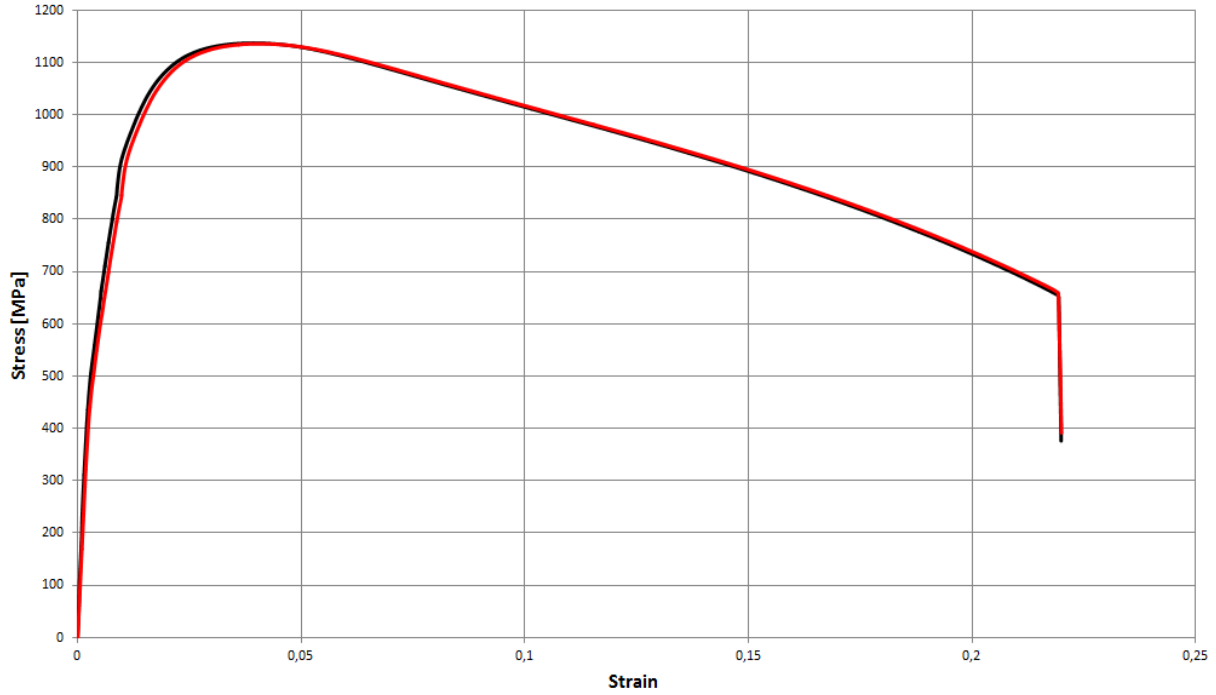
Stress [MPa]
Strain
0
100
200
300
400
500
600
700
800
900
1000
1100
1200
0
0,05
0,1
0,15
0,2
0,25

A20

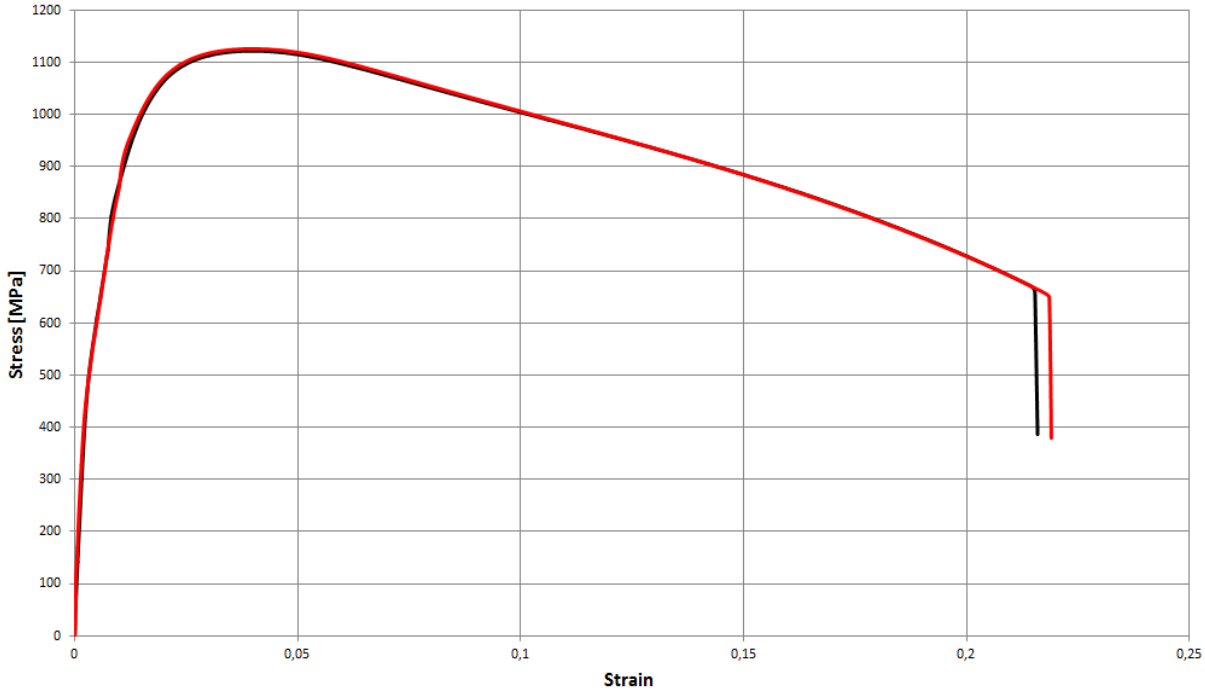
Stress [MPa]
Strain
0
100
200
300
400
500
600
700
800
900
1000
1100
1200
0
0,05
0,1
0,15
0,2
0,25

A1T

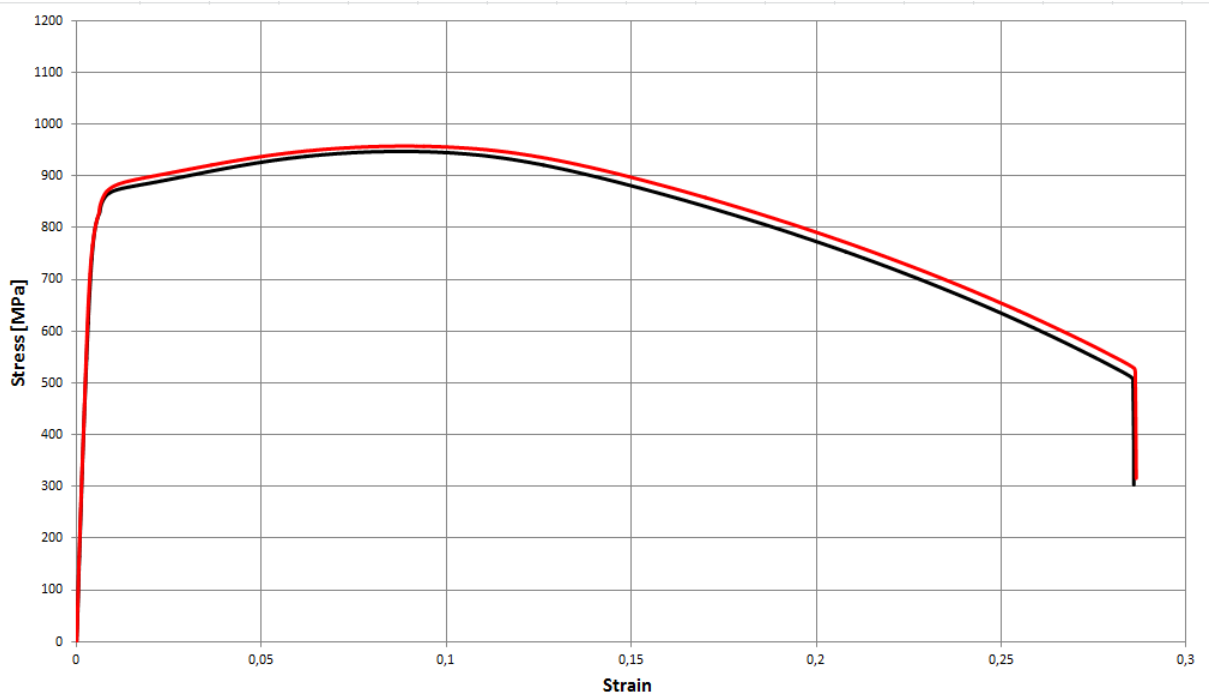
Stress [MPa]
Strain
0
100
200
300
400
500
600
700
800
900
1000
1100
1200
0
0,05
0,1
0,15
0,2
0,25
0,3

A2T

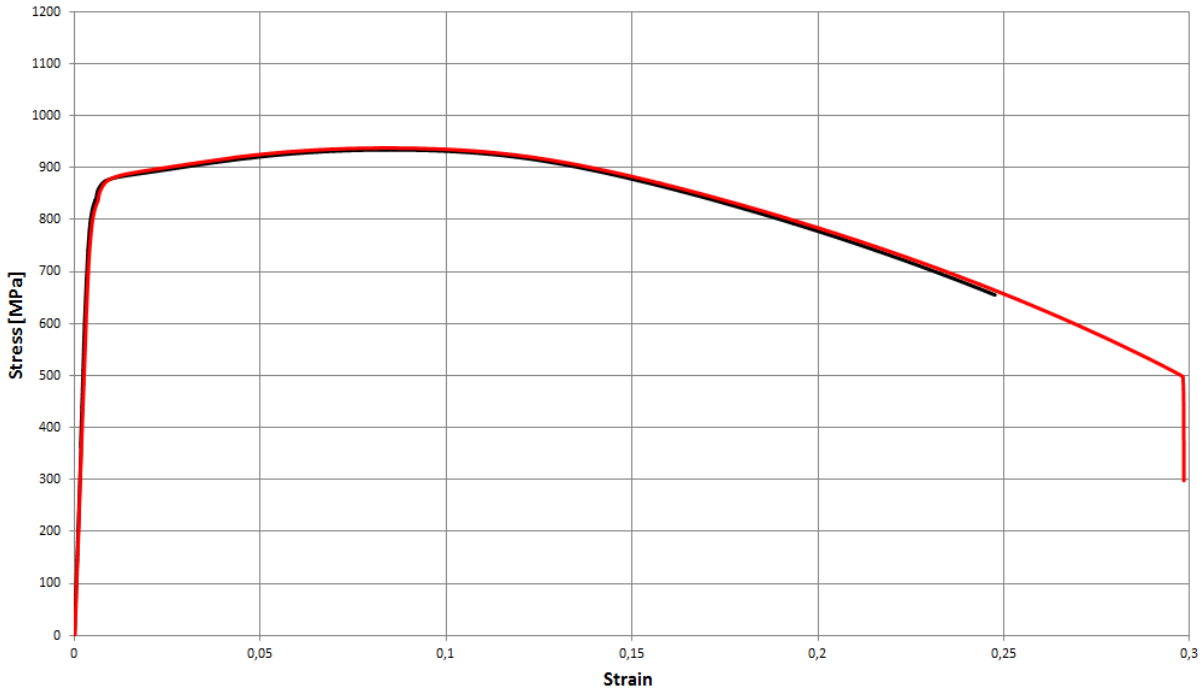
Stress [MPa]
Strain
0
100
200
300
400
500
600
700
800
900
1000
1100
1200
0
0,05
0,1
0,15
0,2
0,25
0,3

A5T

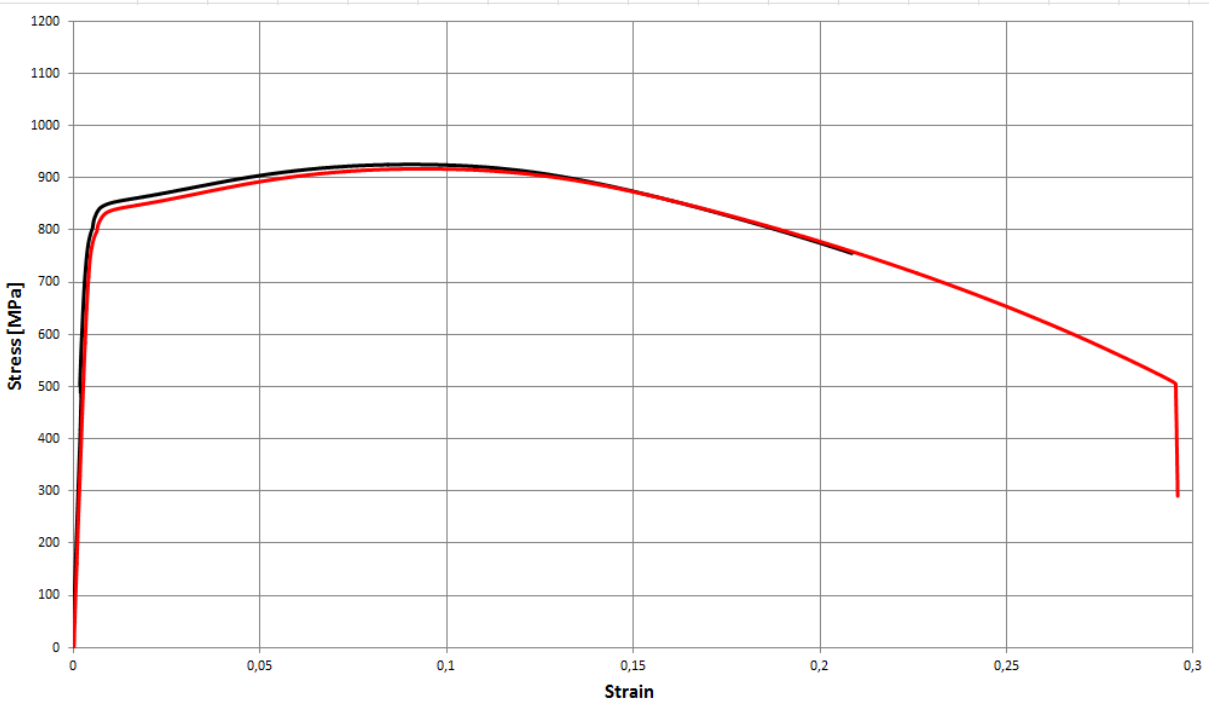
Stress [MPa]
Strain
0
100
200
300
400
500
600
700
800
900
1000
1100
1200
0
0,05
0,1
0,15
0,2
0,25
0,3

A10T

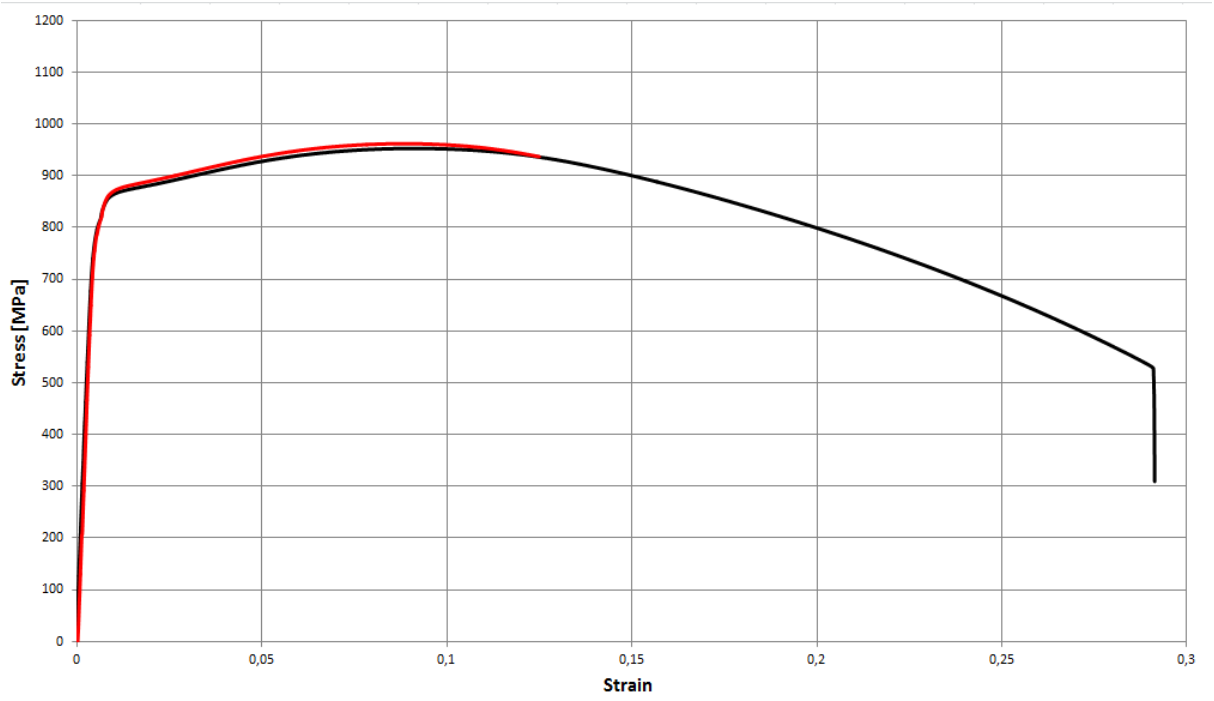
Stress [MPa]
Strain
0
100
200
300
400
500
600
700
800
900
1000
1100
1200
0
0,05
0,1
0,15
0,2
0,25
0,3

A20T

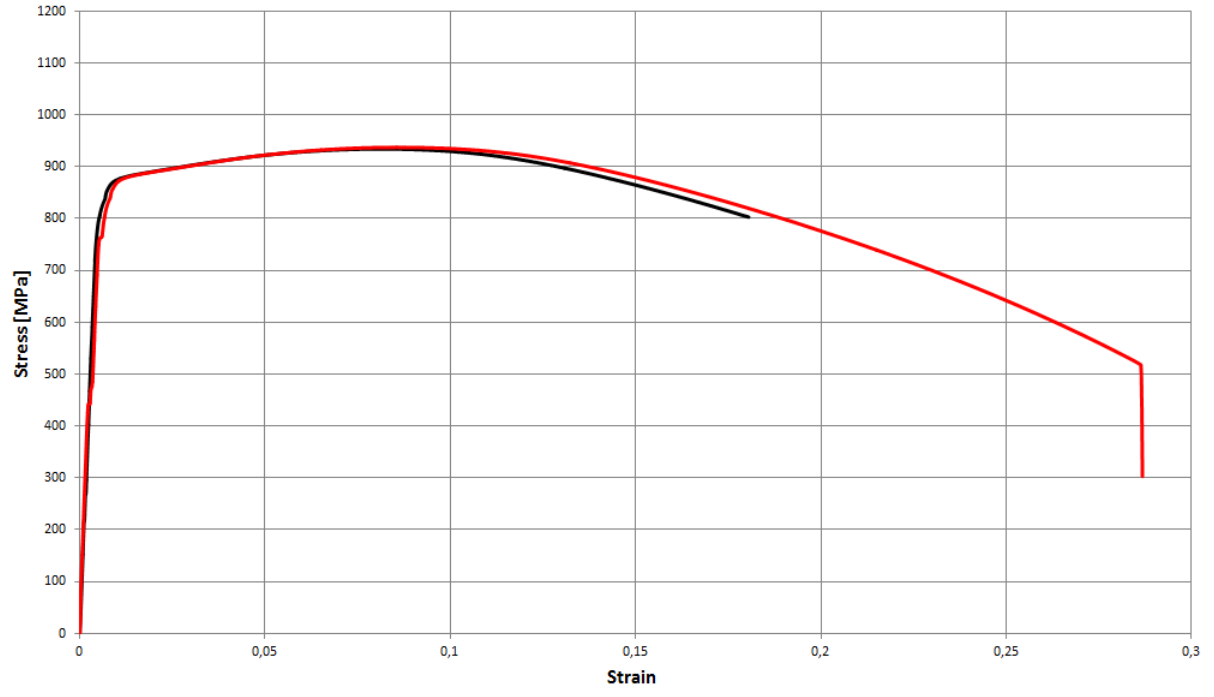
Stress [MPa]
Strain
0
100
200
300
400
500
600
700
800
900
1000
1100
1200
0
0,05
0,1
0,15
0,2
0,25
0,3

H1

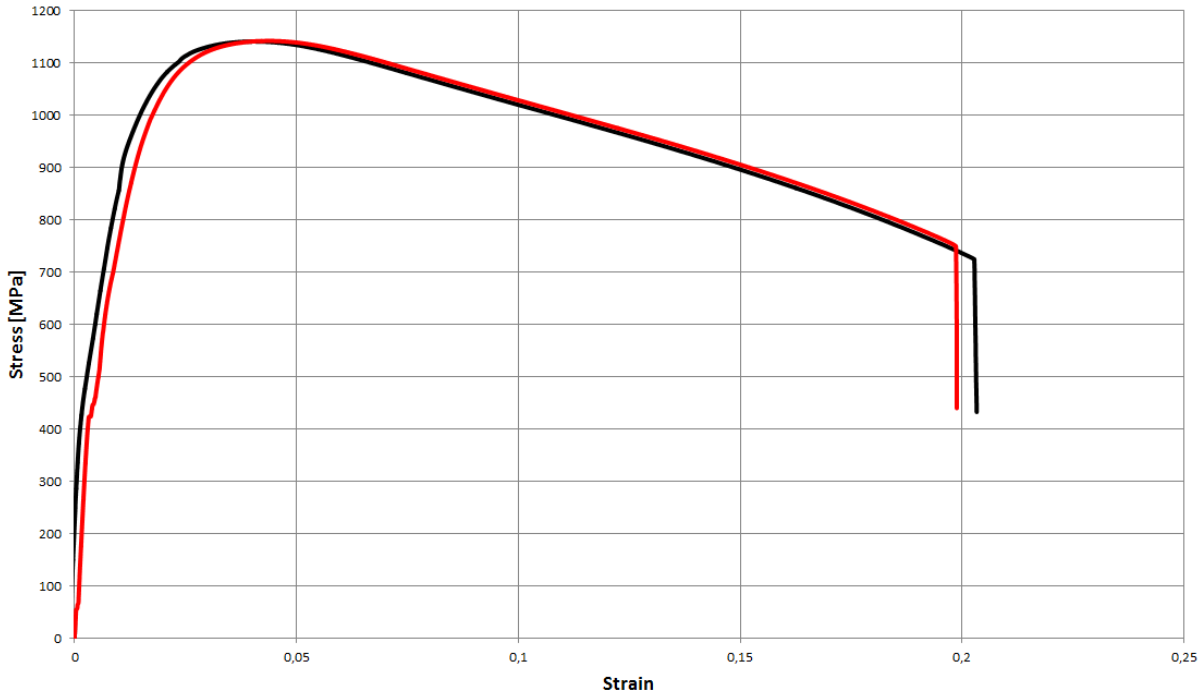
Stress [MPa]
Strain
0
100
200
300
400
500
600
700
800
900
1000
1100
1200
0
0,05
0,1
0,15
0,2
0,25

H2

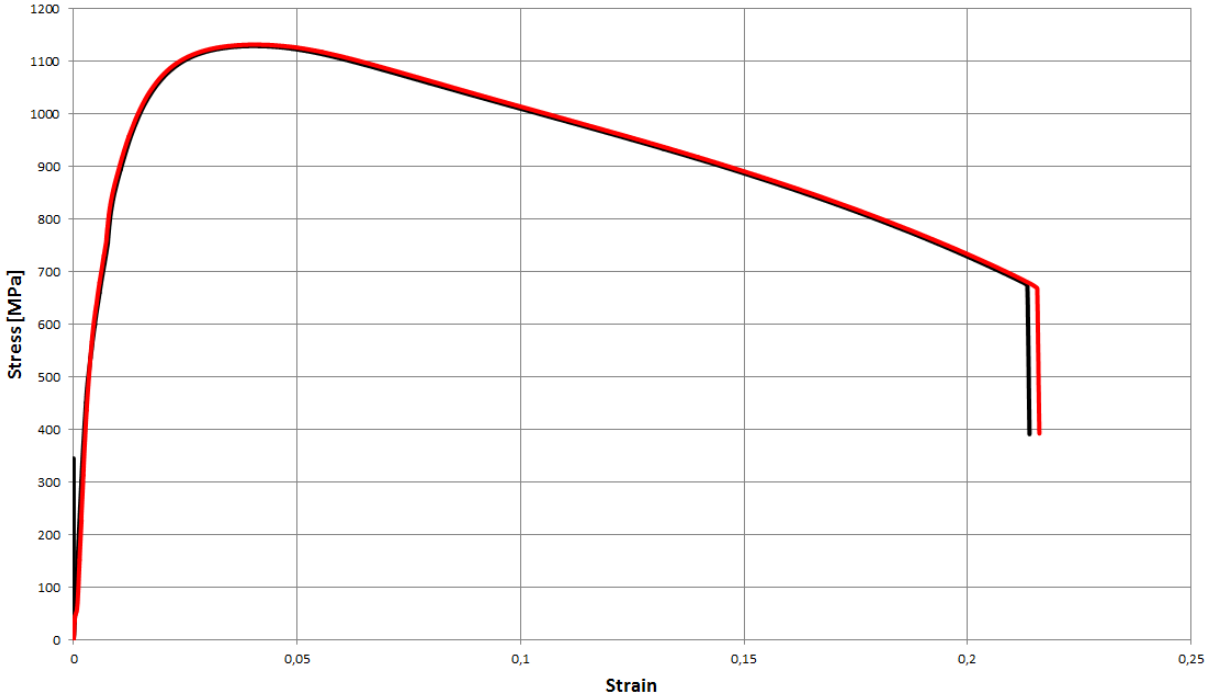
Stress [MPa]
Strain
0
100
200
300
400
500
600
700
800
900
1000
1100
1200
0
0,05
0,1
0,15
0,2
0,25

H5

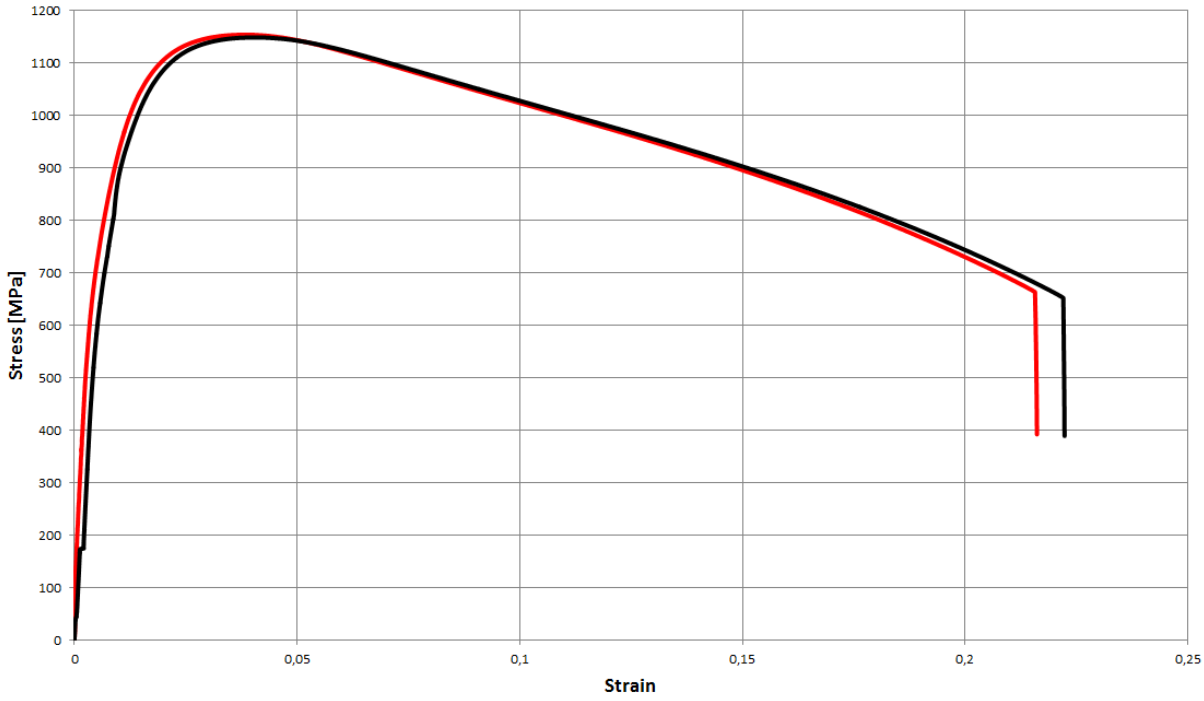
Stress [MPa]
1200
1100
1000
900
800
700
600
500
400
300
200
100
0
0
0,05
0,1
0,15
0,2
0,25
Strain

H10

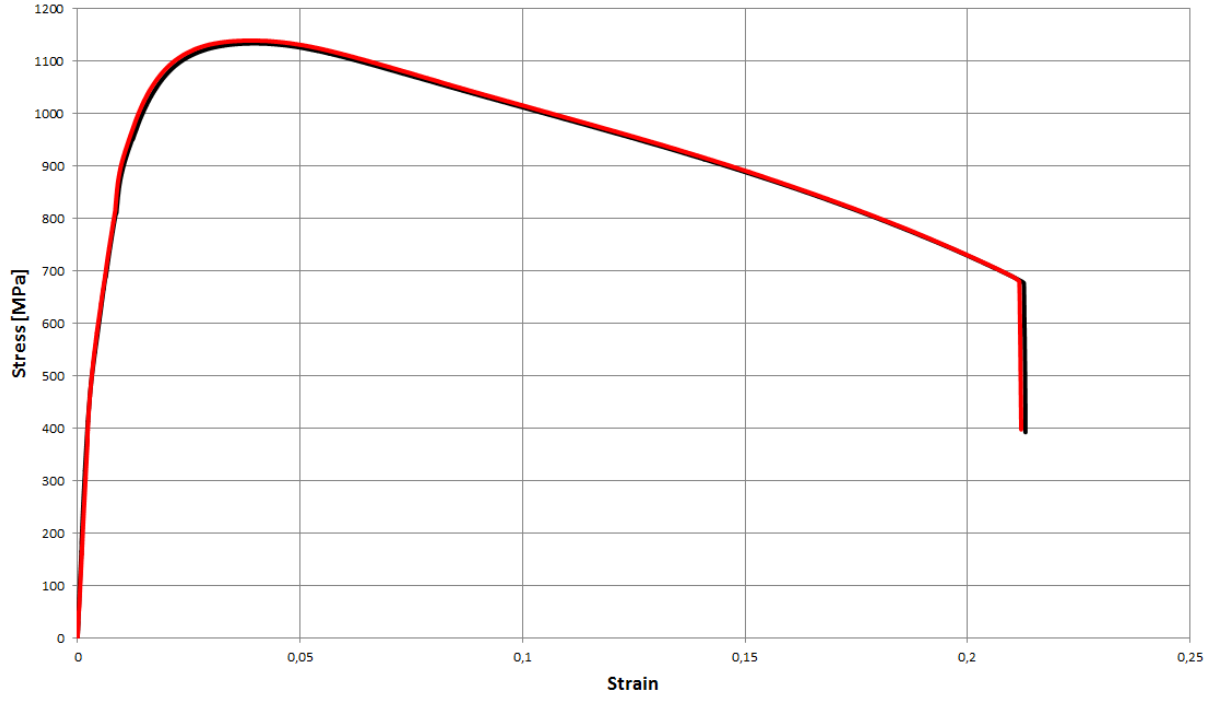
Stress [MPa]
1200
1100
1000
900
800
700
600
500
400
300
200
100
0
0
0,05
0,1
0,15
0,2
0,25
Strain

H20

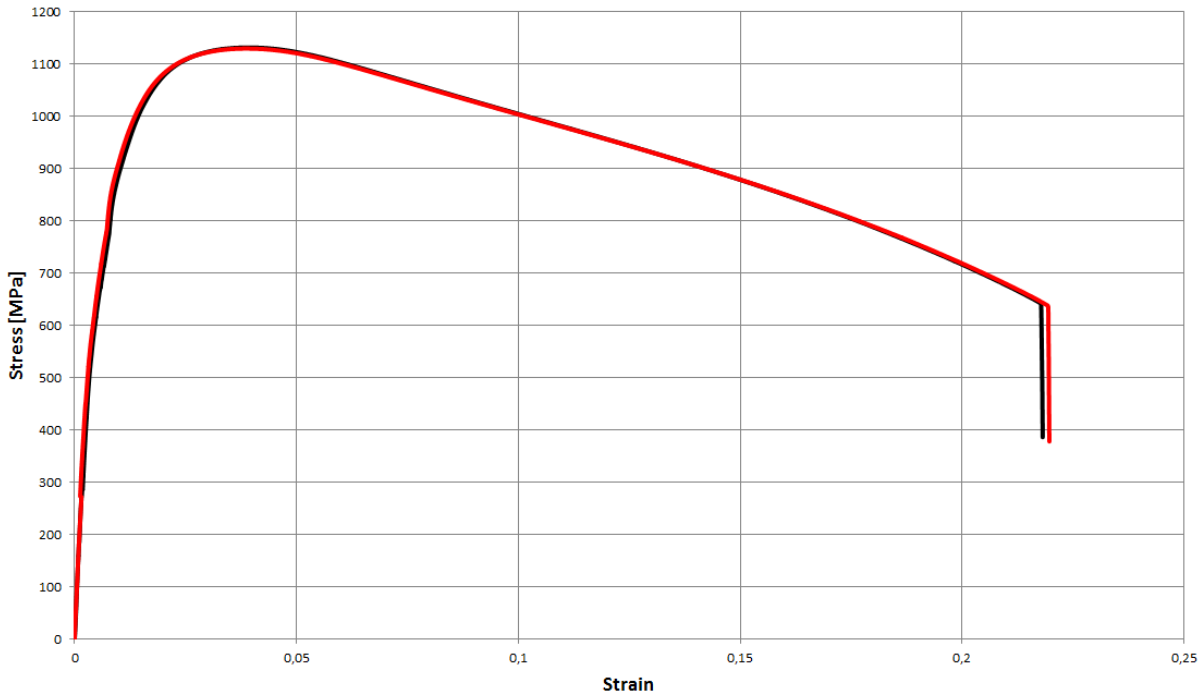
Stress [MPa]
Strain
0
100
200
300
400
500
600
700
800
900
1000
1100
1200
0
0,05
0,1
0,15
0,2
0,25

H1T

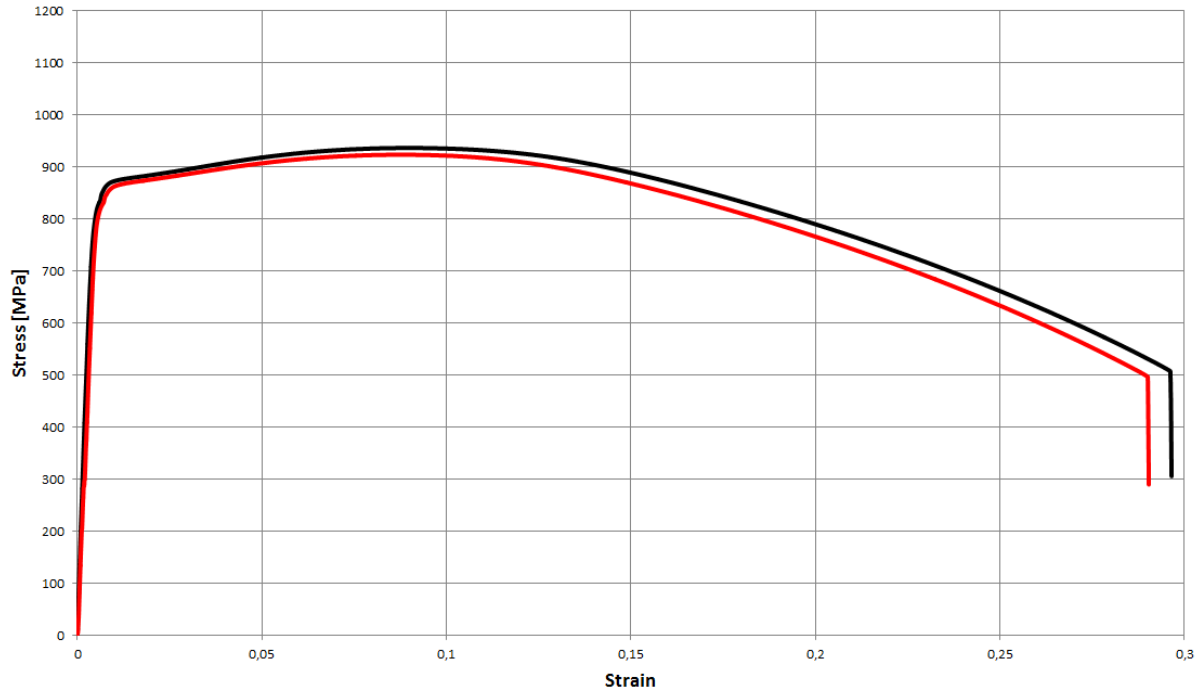
Stress [MPa]
Strain
0
100
200
300
400
500
600
700
800
900
1000
1100
1200
0
0,05
0,1
0,15
0,2
0,25
0,3

H2T

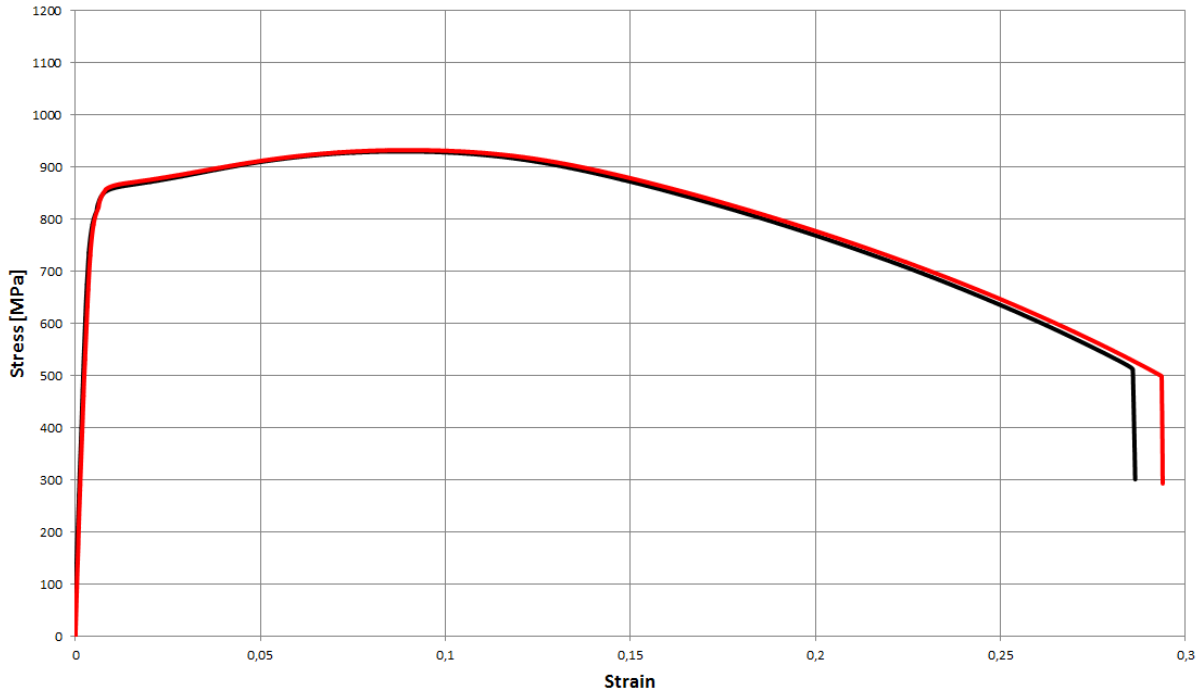
1200
1100
1000
900
800
700
600
500
400
300
200
100
0
Stress [MPa]
0
0,05
0,1
0,15
0,2
0,25
0,3
Strain

H5T

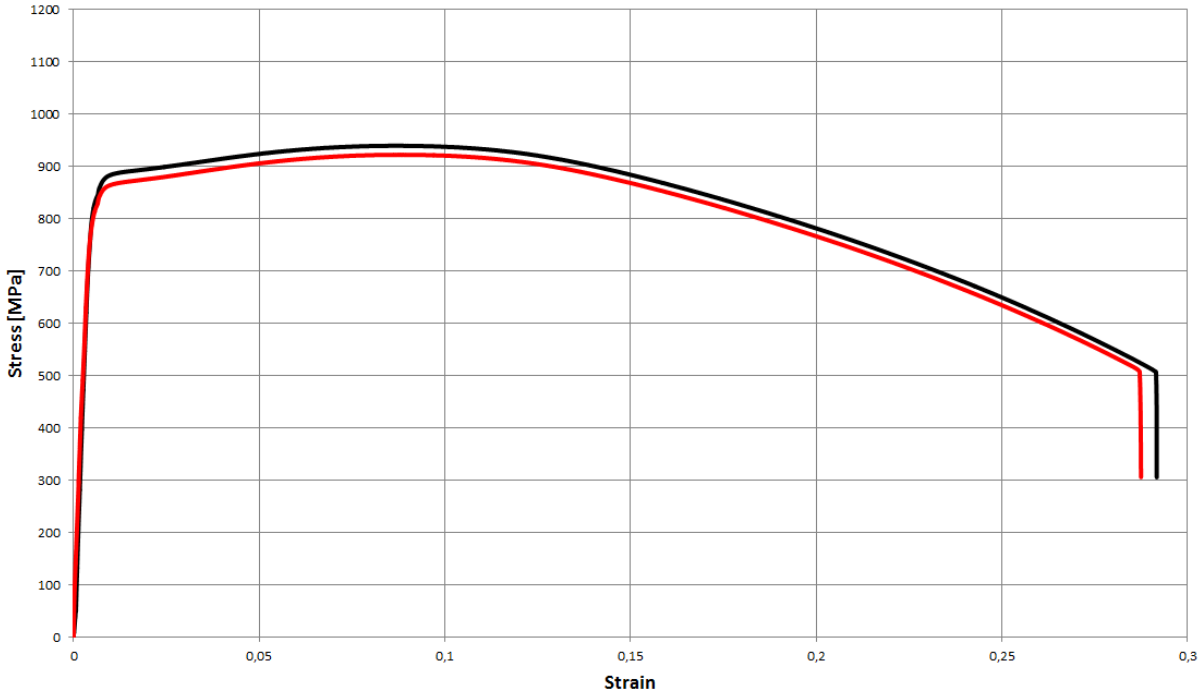
1200
1100
1000
900
800
700
600
500
400
300
200
100
0
Stress [MPa]
0
0,05
0,1
0,15
0,2
0,25
0,3
Strain

H10T

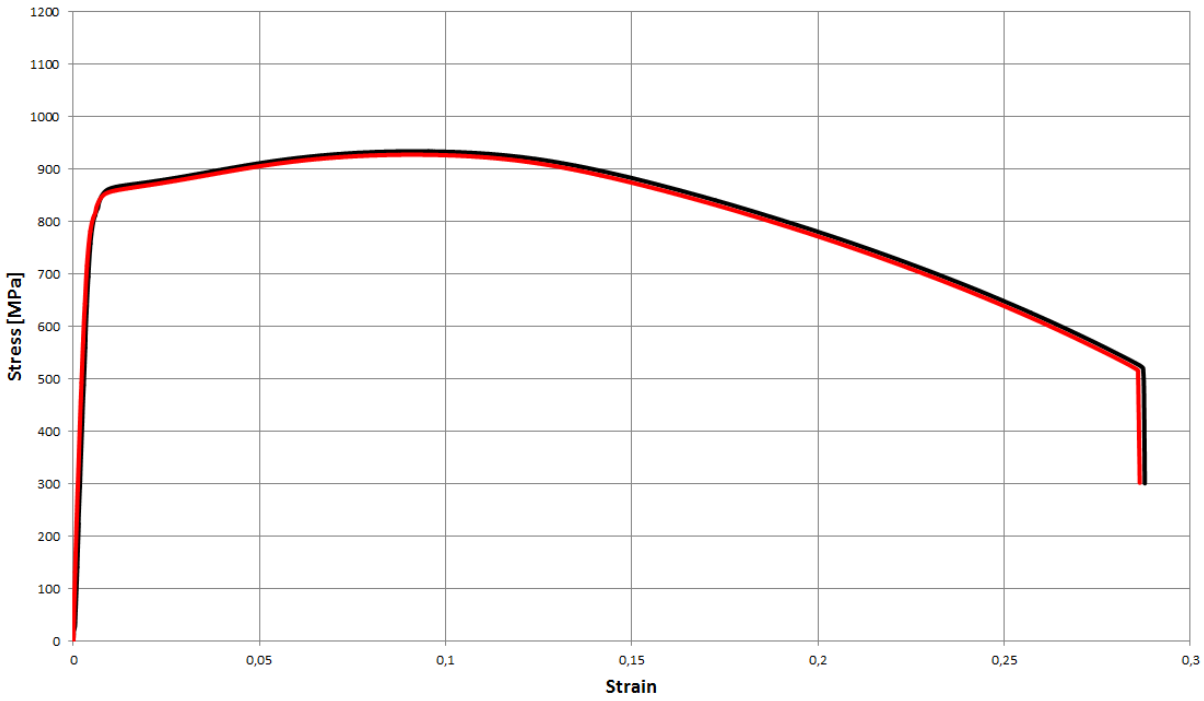
Stress [MPa]
Strain
0
100
200
300
400
500
600
700
800
900
1000
1100
1200
0
0,05
0,1
0,15
0,2
0,25
0,3

H20T

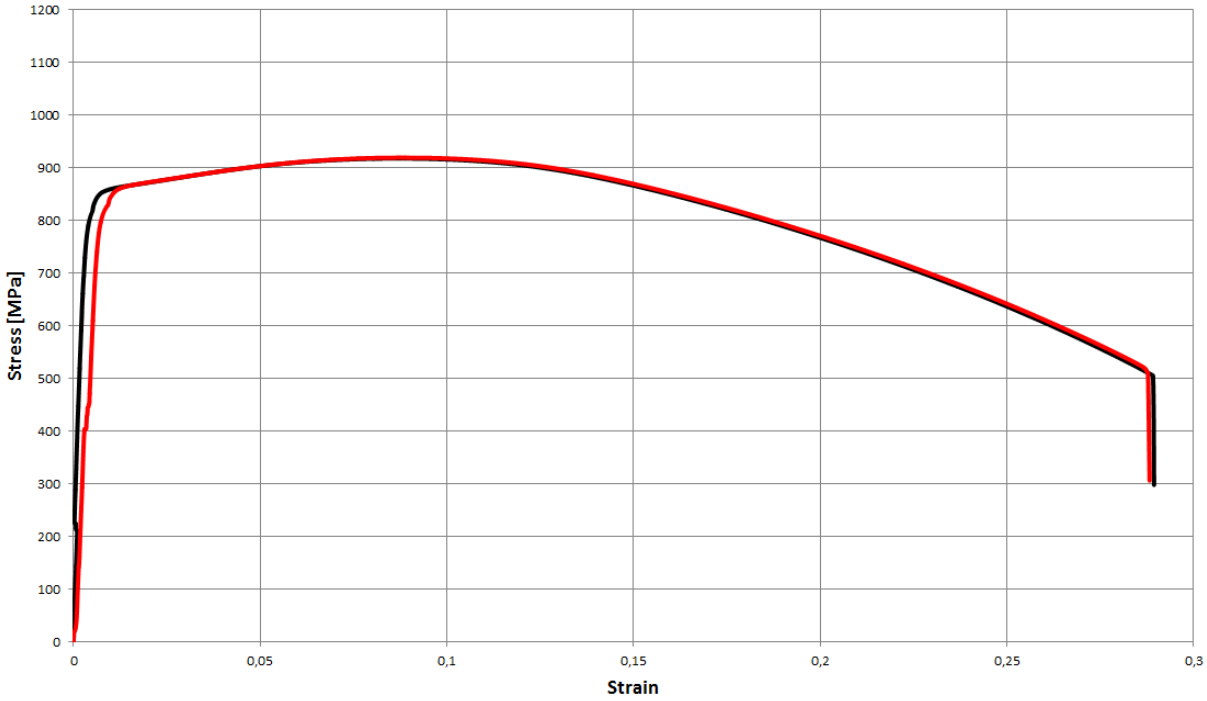
Stress [MPa]
Strain
0
100
200
300
400
500
600
700
800
900
1000
1100
1200
0
0,05
0,1
0,15
0,2
0,25
0,3

Appendix D – Optical light micrographs w. different magnifications

D.1 - 10X magnification

As-quenched A-samples (1000 °C, A1 – A20)

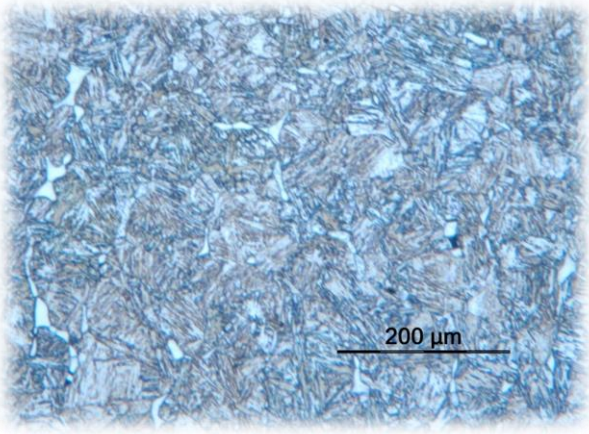

A1

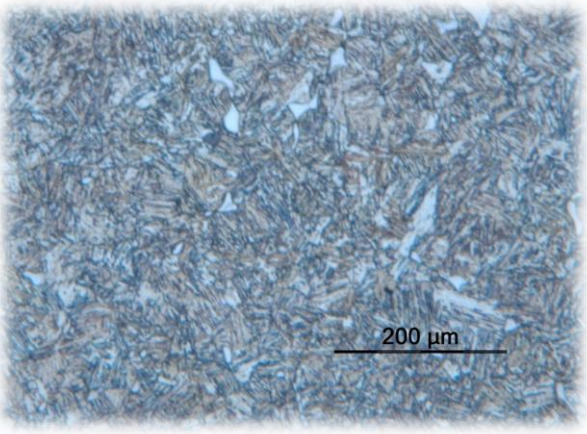

A2

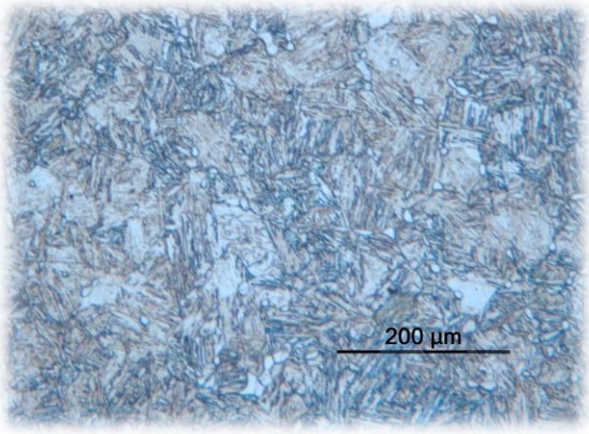

A5

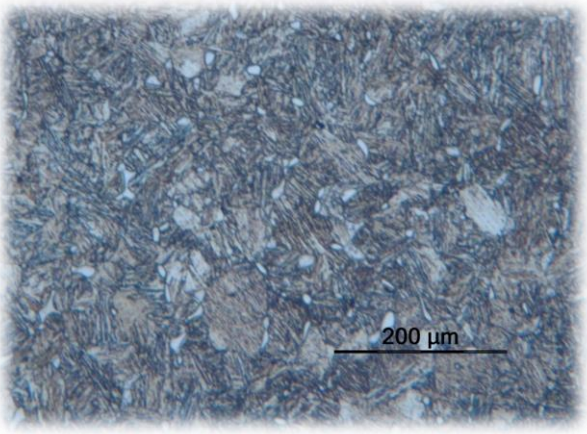

A10

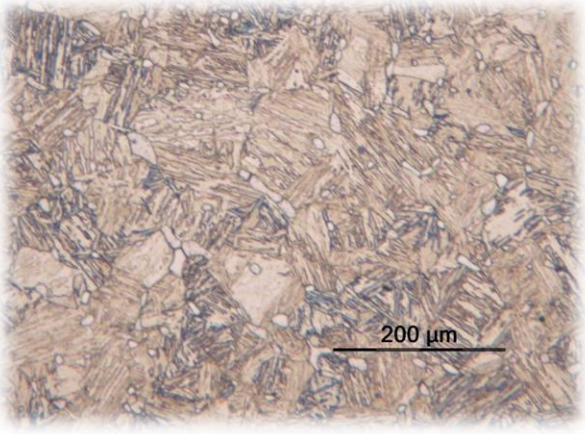

A20

Tempered A-samples (1000 °C, A1T – A20T)

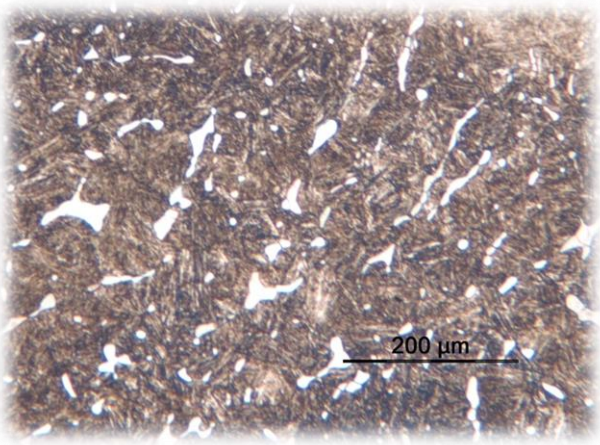

A1T

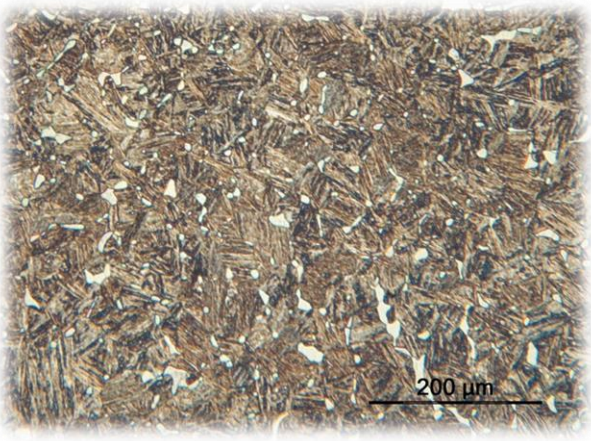

A2T

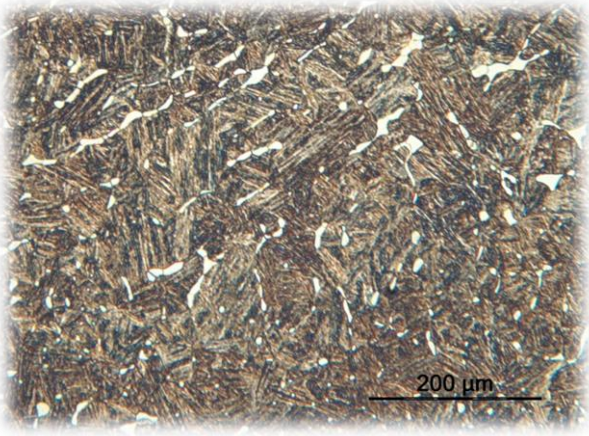

A5T

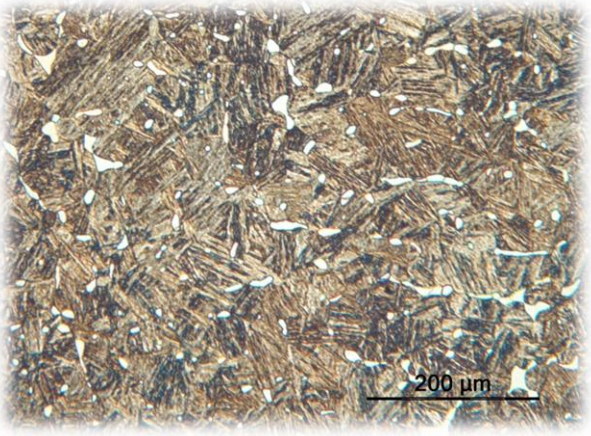

A10T

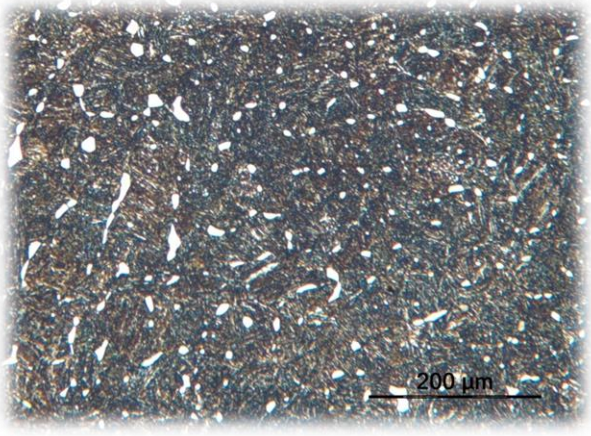

A20T

As-quenched H-samples (1030 °C, H1 – H20)

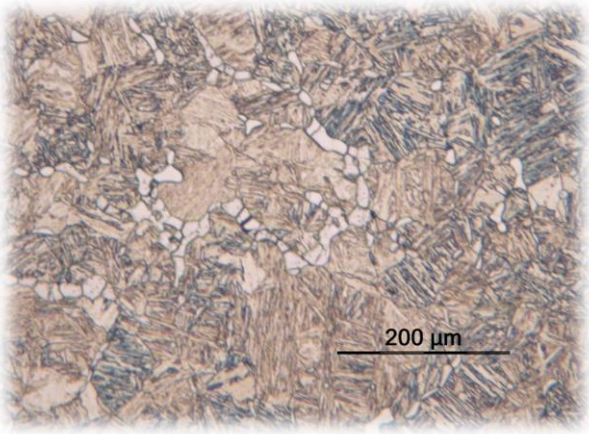

H1

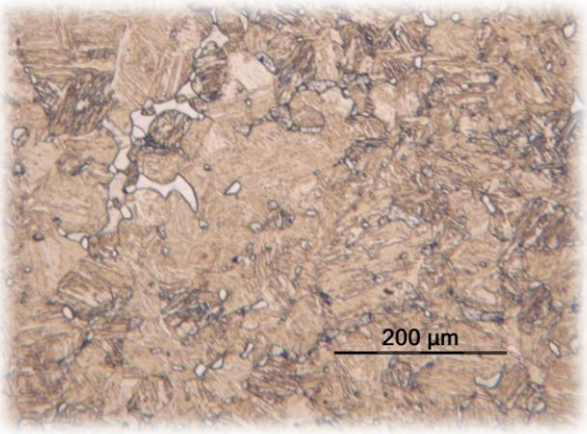

H2

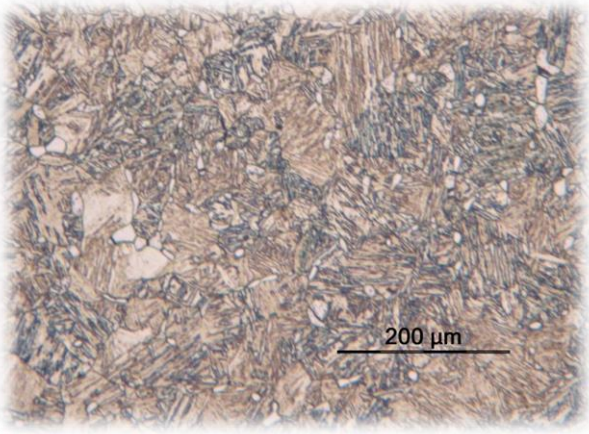

H5

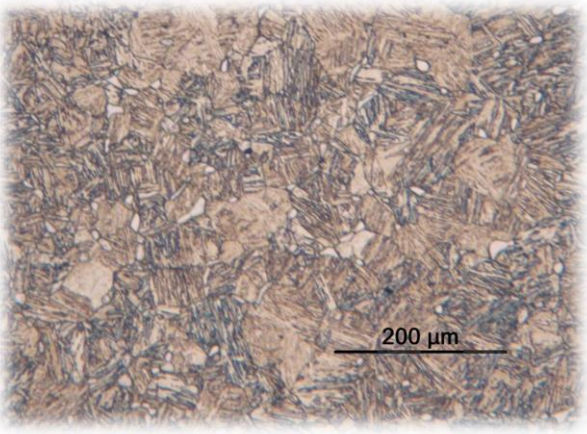

H10

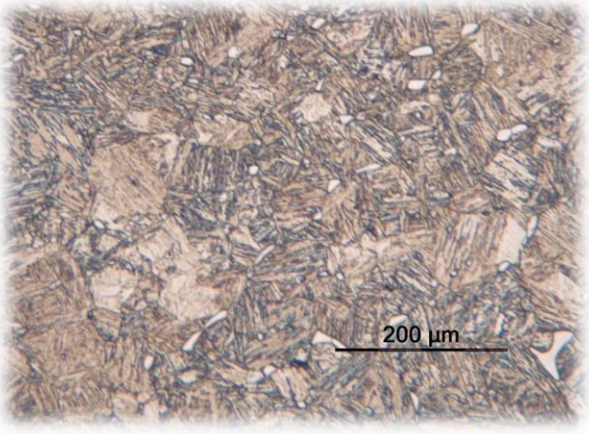

H20

Tempered H-samples (1030 °C, H1T – H20T)

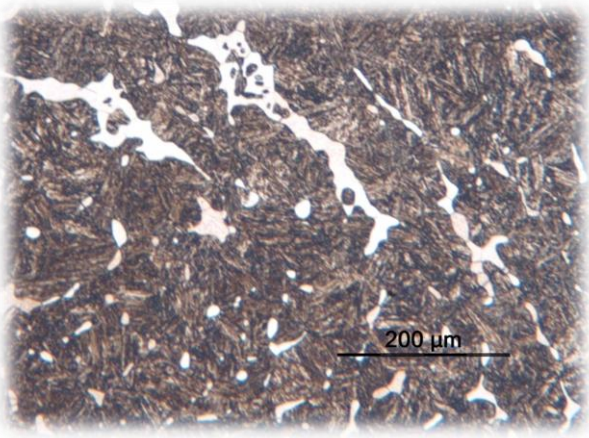

H1T

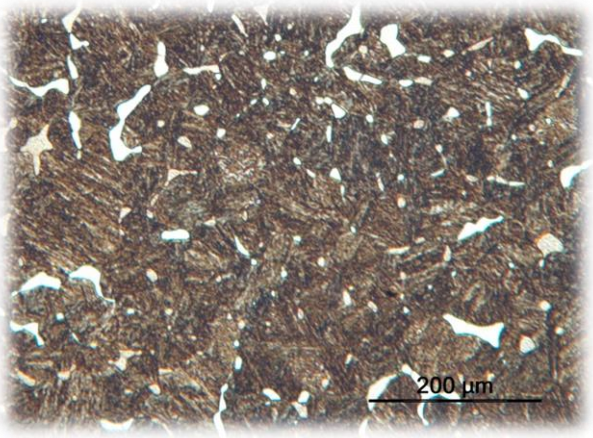

H2T

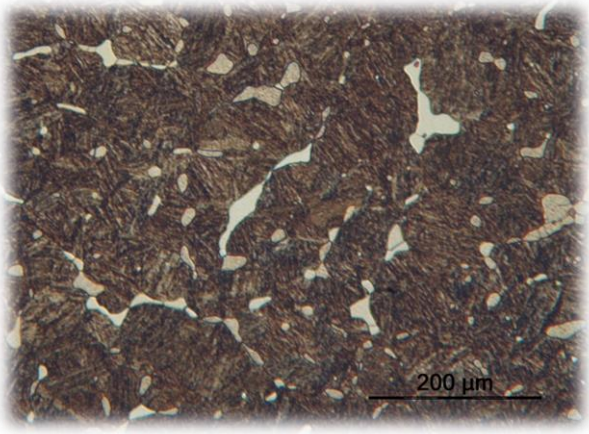

H5T

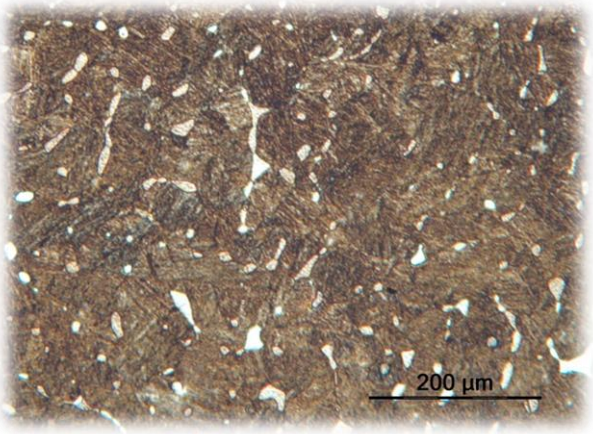

H10T

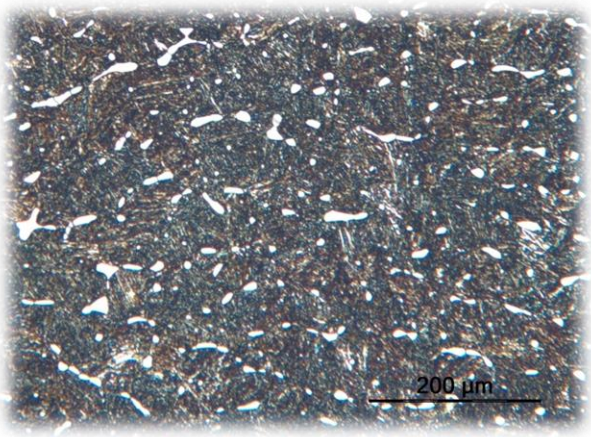

H20T

D.2 – 50X magnification

As-quenched A-samples (1000 °C, A1 – A20)

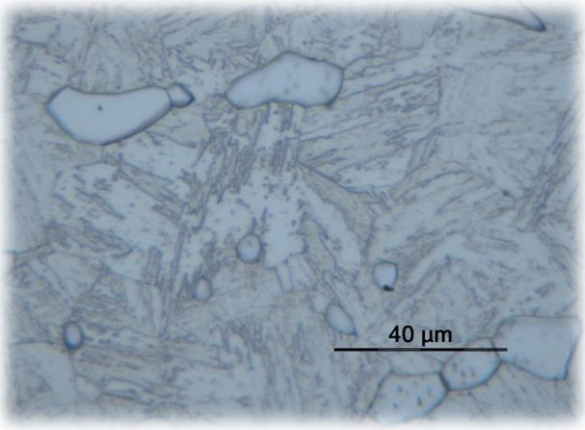

A1

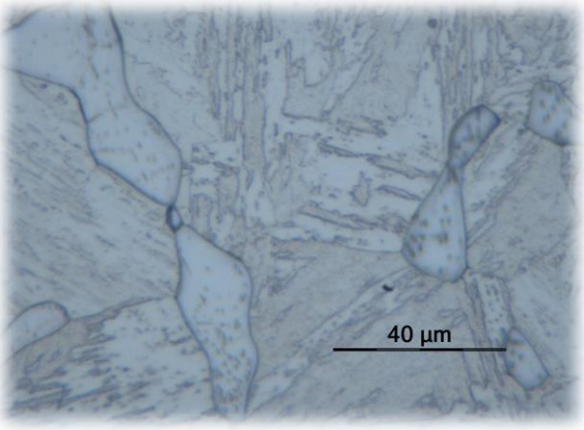

A2

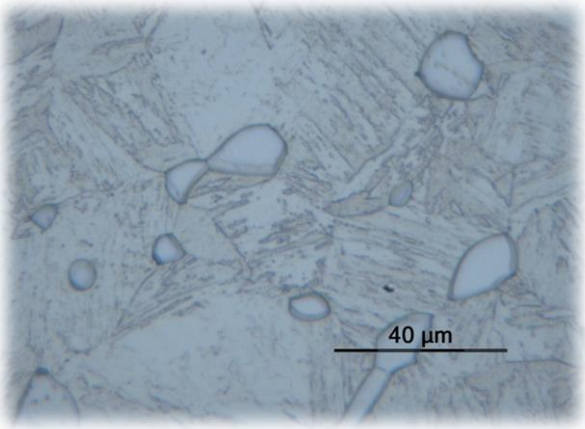

A5

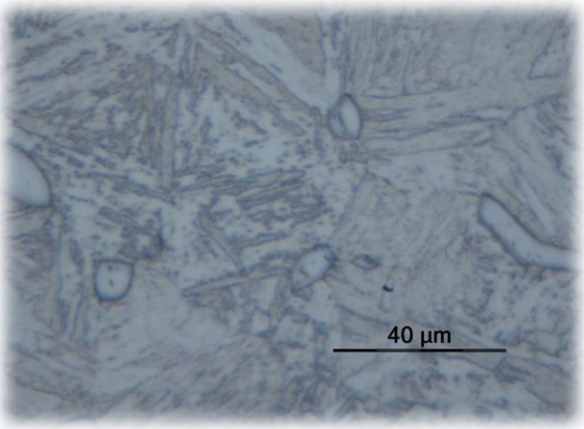

A10

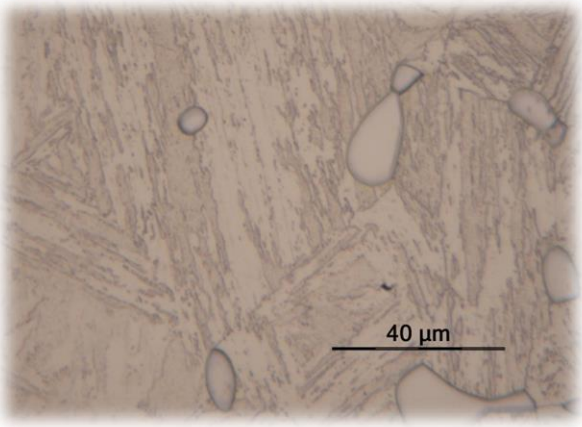

A20

Tempered A-samples (1000 °C, A1T – A20T)

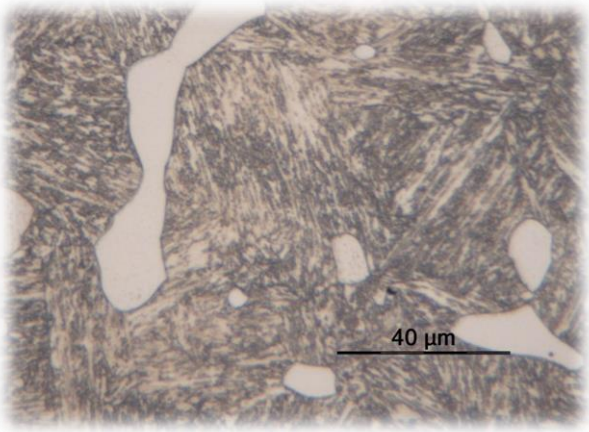

A1T

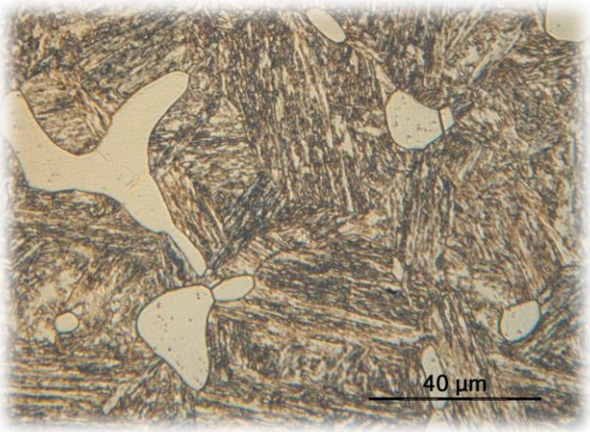

A2T

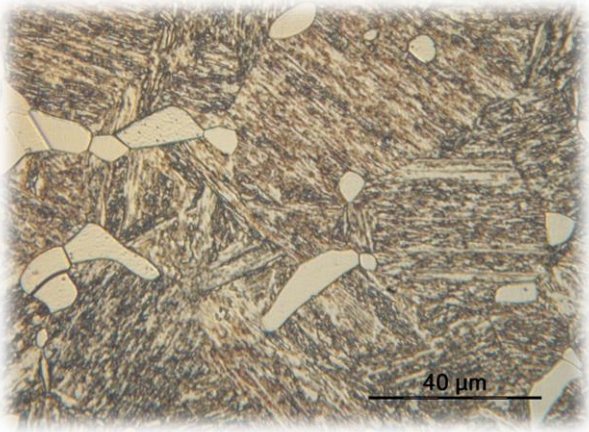

A5T

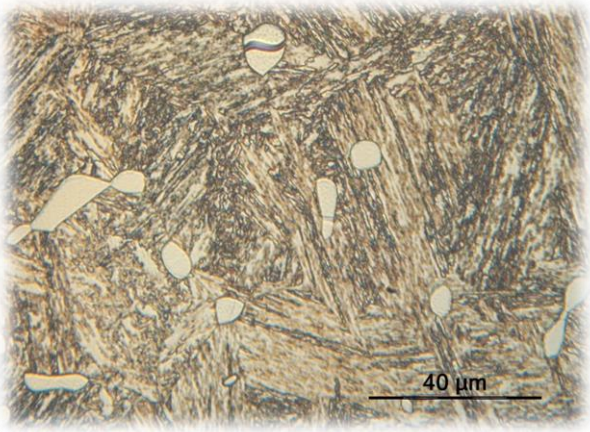

A10T

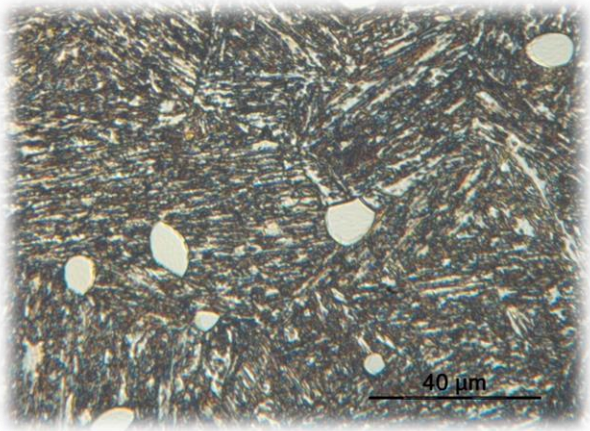

A20T

As-quenched H-samples (1030 °C, H1 – H20)

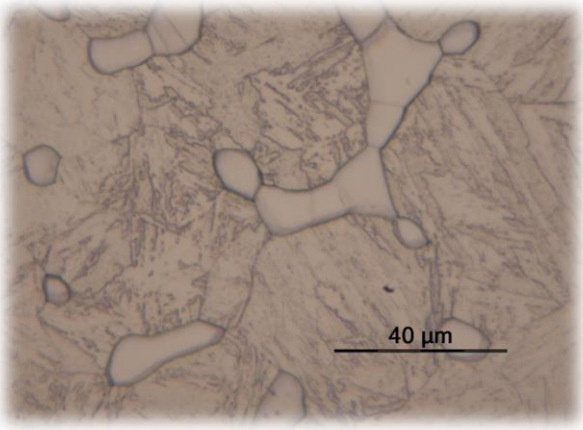

H1

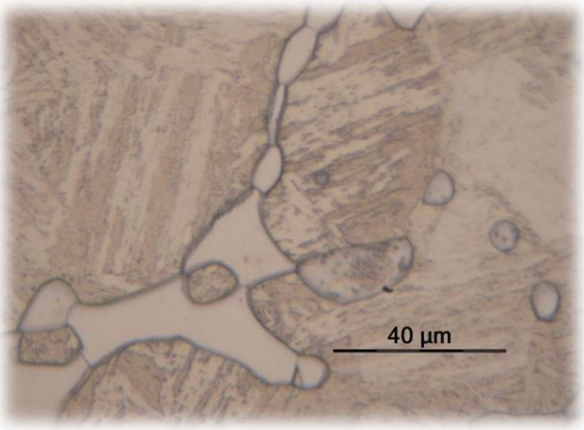

H2

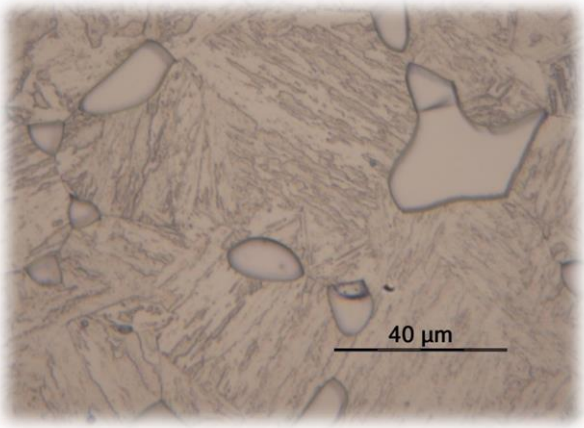

H5

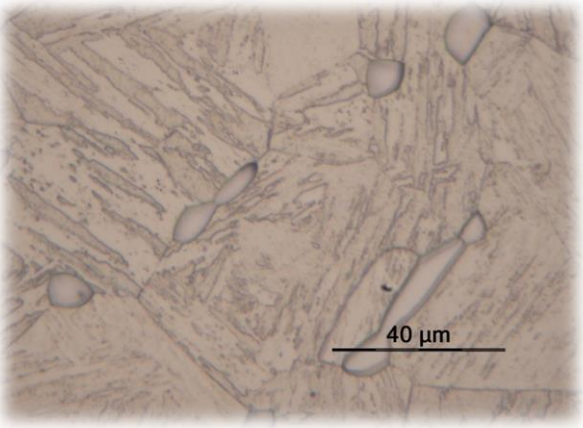

H10

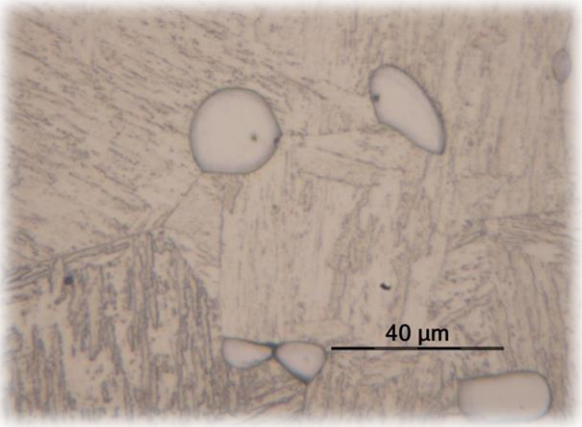

H20

Tempered H-samples (1030 °C, H1T – H20T)

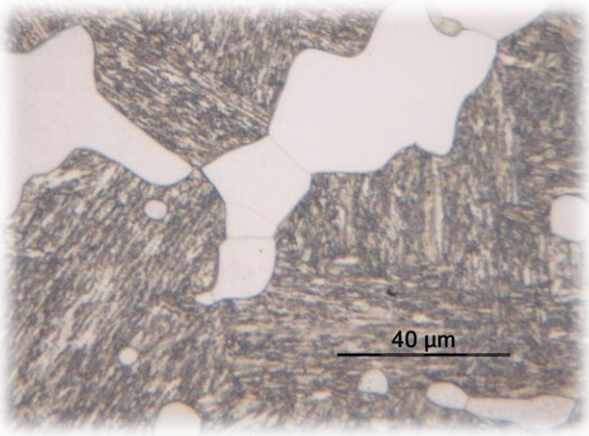

H1T

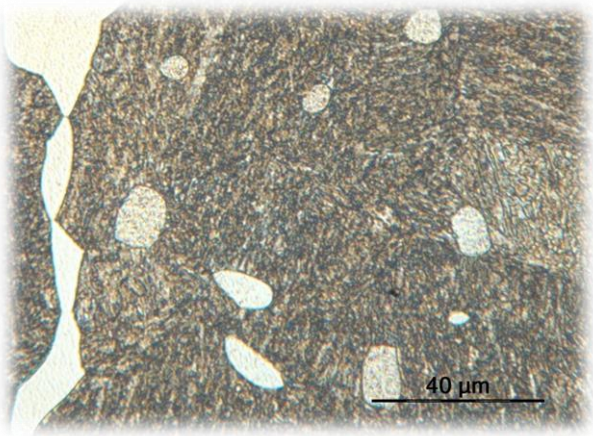

H2T

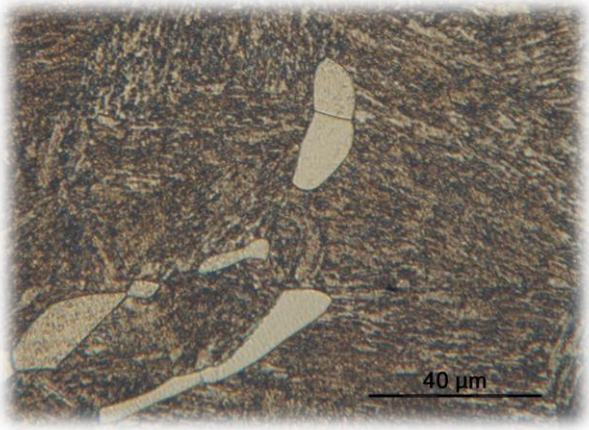

H5T

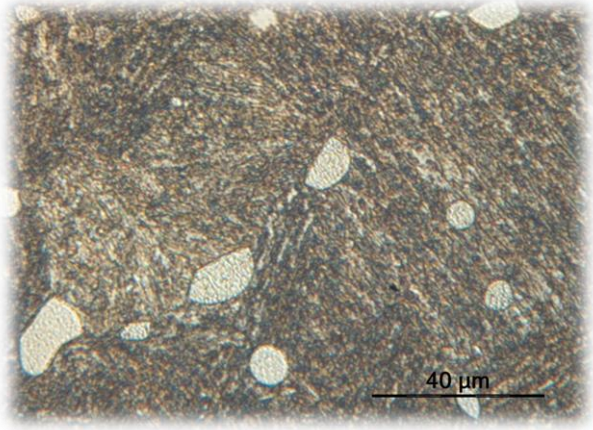

H10T

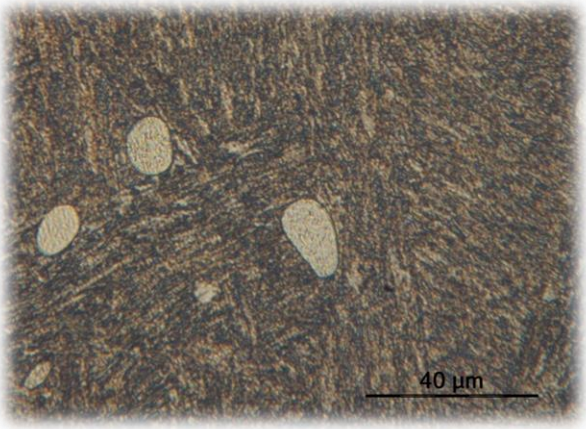

H20T

Appendix E – Correlation with soaking time for A, H and HT-samples

E.1 – A-samples

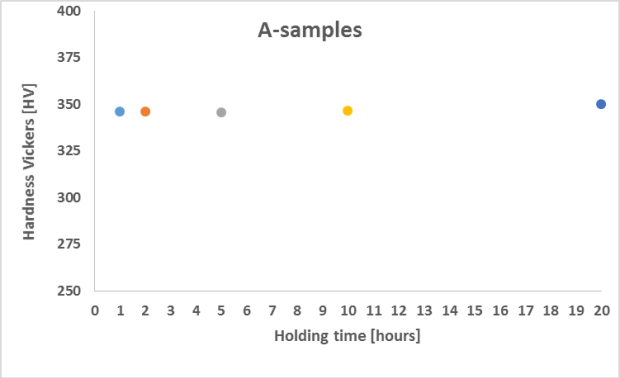

(a)

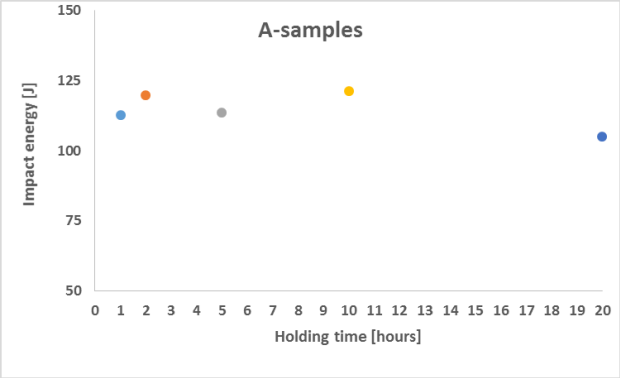

(b)

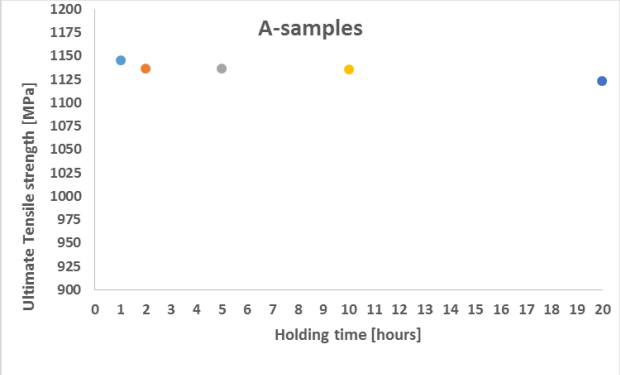

(c)

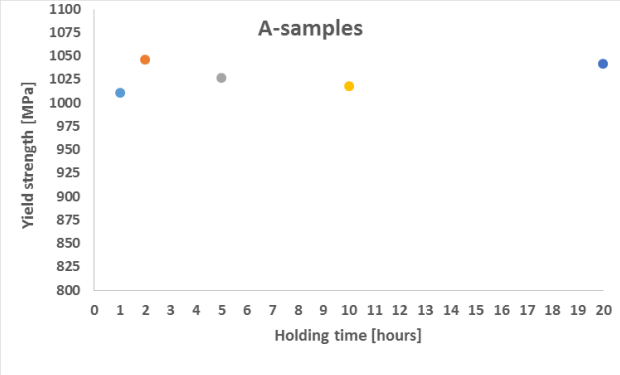

(d)

Correlation of soaking times and (a) hardness, (b) impact energy, (c) ultimate tensile strength and (d) yield strength for A-samples

E.2 – H-samples

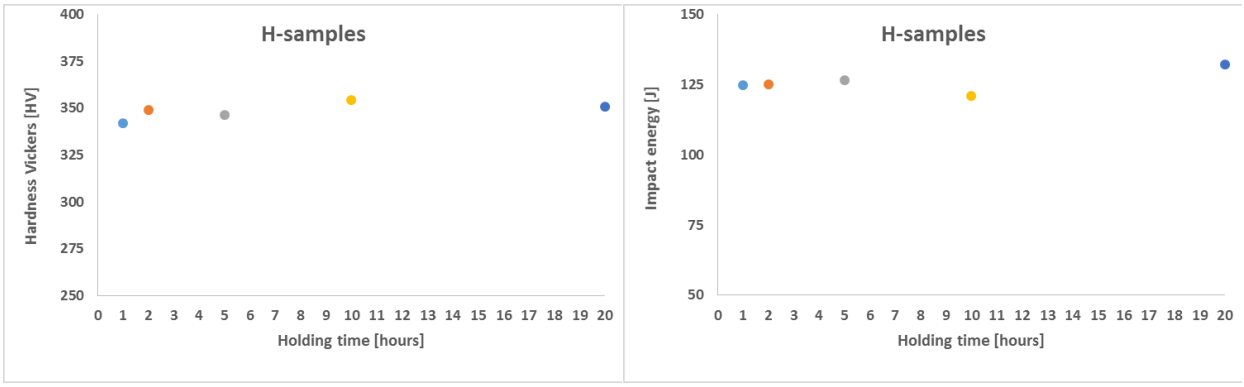

(a)

(b)

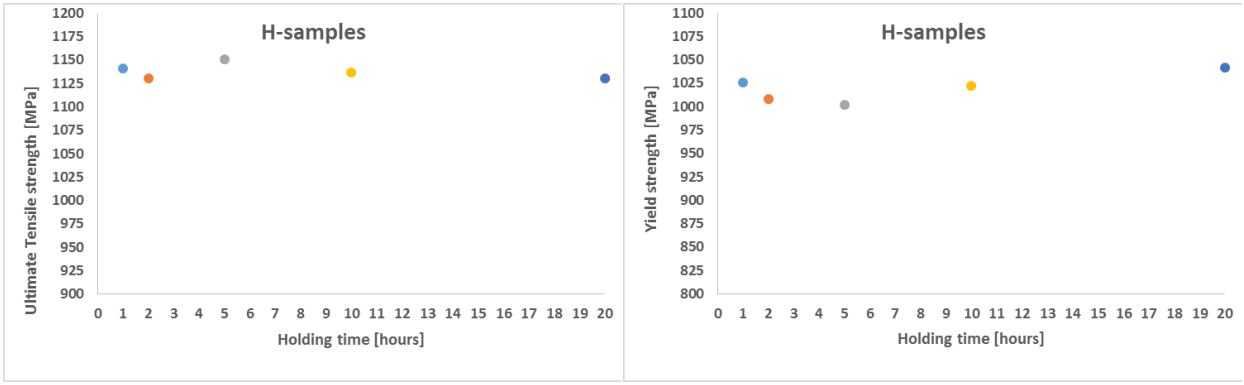

(c)

(d)

Correlation of soaking times and (a) hardness, (b) impact energy, (c) ultimate tensile strength and (d) yield strength for H-samples

E.3 – HT-samples

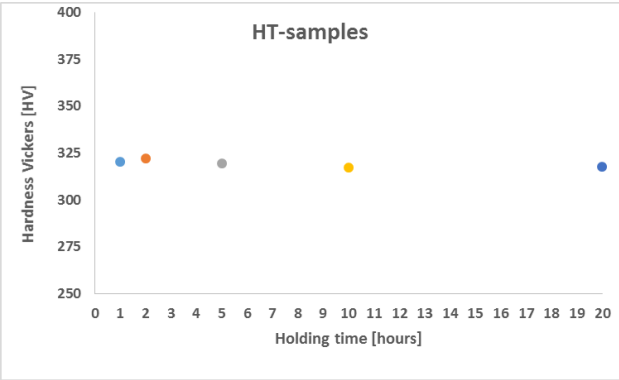

(a)

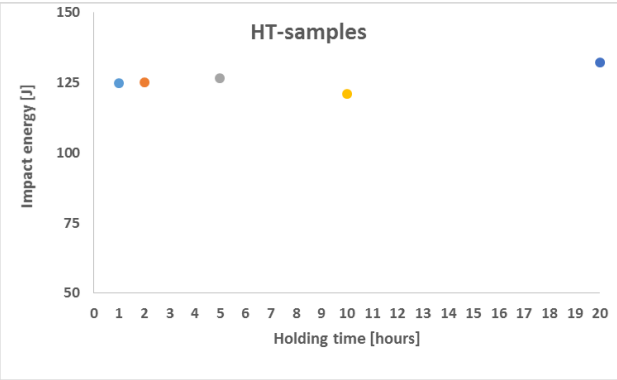

(b)

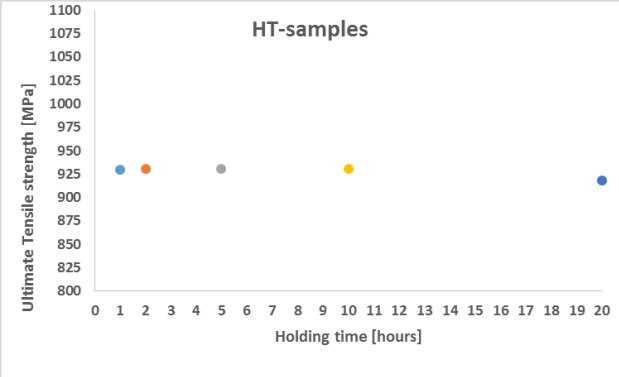

(c)

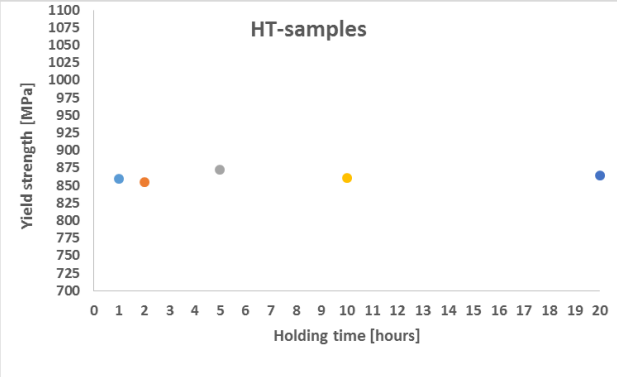

(d)

Correlation of soaking times and (a) hardness, (b) impact energy, (c) ultimate tensile strength and (d) yield strength for HT-samples

Appendix F – Reliability of experimental/analytical methods

F.1 EBSD

EBSD is a widely popular and used analysis tool. However, the statistical reliability of EBSD based results is open for discussion, since typical volumes analyzed using such methods are significantly smaller than those analyzed using other techniques (for example XRD). If a material with a fine microstructure is to be examined, there is a wide tendency to use smaller step sizes. This limits the investigation to relatively small areas in order to be able to complete the measurements within a reasonable amount of time. This raises the problem where generalized conclusions regarding global material information are drawn based on information collected from a very small material volume.

The reliability of EBSD as a conclusion tool is limited. Different techniques have been tested in order to determine phase fractions in TRIP steels. Those studies have proven to show a rather large variance in the results, indicating that possibly false conclusions regarding the material macrostructure are drawn from utilizing techniques incorrectly (Jacques, et al., 2009). However, if allowed an adequate sampling size, the EBSD scan points can be estimated to be statistically accurate for determinations regarding the general material structure. The EBSD scans in this thesis focused on producing results gained from scans using relatively small step sizes (i.e. a high number of sampling points). Therefore, it is believed that the EBSD scan results obtained in this thesis are reliable.

F.2 Threaded tensile stress test connectors

The tensile stress test specimens were post-machining too short to be correctly inserted into the testing device. Therefore, an elongation-connector had to be manufactured, using threads to connect and disconnect it from the different tensile stress test specimens. Given the nature of threaded connections, it is useful to examine if whether the threaded connection had a noticeable impact on the tensile stress testing results.

The connector was constructed using St-37 structural steel, using an outer diameter sufficiently large enough to not be affected by the tensile stress testing. A center bore, measuring 14 mm in diameter, was drilled 45 mm from one end. An M16 x 2 internal thread with tolerance 6G was machined in the connector, which corresponded to the external M16 x 2 threads on the tensile stress test specimens, machined with tolerance 6g.

Threaded connections should normally be designed so that the female (i.e. internal) threads break prior to the male threads experiencing stripping. However, given the nature of the tensile stress test, the connector could not fail under tension prior to the actual test specimen, as this would not enable the specimen to fail. This is why the large thread dimension and corresponding tolerance classes were used. There was also the issue with the bolt material (i.e. the test specimen) exhibiting far greater material properties in terms of yield strength. Material theory of threads dictate that if the bolt material is stronger than the nut material (as in this case), the bolt threads would tear out the nut threads in case of failure (ASTM, 2014). The failure would occur at the root of the nut threads. Also, in order to prevent yield in the weaker threads, the length of the thread must be sufficient to provide an adequate surface contact area between the male and the female threads. For M16 x 2 threads that are 40 mm long, a factor of yield should not be a problem.

One test occurred, where a suspected yield and/or slight failure of the threads affected the results in terms of elongation on sample H5. See the figure for an illustration on how this affected the stress/strain curve. This was corrected for when calculating the yield and ultimate tensile strengths of the material. The threaded connectors were deemed to be sufficiently dimensioned, and is not believed to have affected the test results.

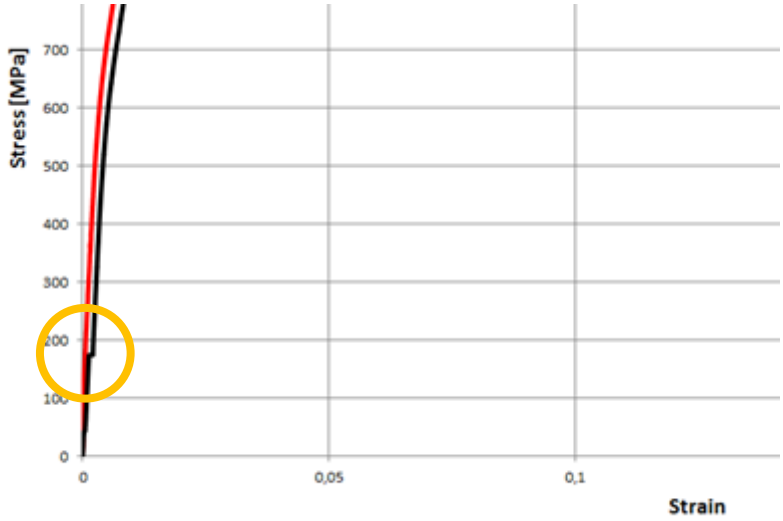

Excerpt of stress/strain curve for sample H5. The noticed strain effect is marked in the figure

F.3 Consequences of varying heating durations (pre-hardening)

As explained in section X, a dummy set of samples were inserted in the furnace chamber simultaneously with all 20 heat treatments. This dummy set recorded the time it took for the samples to reach a stable core temperature equal to the relevant hardening temperature. The dummy set consisted of one rod measuring approximately 20 mm x 20 mm x 185 mm and one rod measuring approximately 12 mm x 12 mm x 185 mm, both with air-sealed thermocouples attached. The larger dummy sample used – as expected – longer time to reach a stable core temperature than its smaller counterpart. The core heating times for the large sample varied from 13 min 20 s up to 14 min 50 s, averaging at 14 m 0 s. The core heating time for the smaller sample varied from 8 min 30 s up to 9 min 50 s, averaging at 9 min 10 s.

The temperature loggers did not provide live data output. Therefore, it was not possible to adjust the soaking time according to the core heating times, i.e. a sample hardened for 1 hour with an average heating time of 11 minutes was not located in the furnace chamber for a total of 1 hour and 11 minutes, only 1 hour. The soaking times at hardening temperatures thus *include the core heating times*. Smaller soaking times were more affected by this variation, seeing that subtracting 10 – 12 minutes from a total of 60 minutes (i.e. 1 hour) makes a greater relative difference than subtracting the same amount from 1200 minutes (i.e. 20 hours). Therefore, if the purpose is to replicate the experiments, these heating times must be taken into account.

It is not believed that the varying core heating times had any noticeable effect on the resulting mechanical properties and/or microstructural analysis performed in this thesis. However, there are possible factors that may have resulted in an increased level of inaccuracy in the reported core heating times. The primary error causes are mechanical. The spot-welded air seal may in reality not have been air-sealed, causing the pre-warmed air in the furnace chamber to affect the thermocouple. Also, the hole drilled in the dummy samples had to be drilled with a clearance allowance for insertion of the thermocouple. The consequence of this was that the thermocouples were surrounded by air within the dummy samples, which may have been more easily affected by the surrounding heat (seeing that the conduction of thermal energy is far greater in steel than in air).

As noted in section 5.1, it is assumed that the reported temperature values from the furnace chamber and the dummy samples to be the true temperature values.

Appendix G – Hardness Brinell values

Brinell Hardness was measured at NOMAC. One indentation per sample was performed and measured. The diameter of the steel ball was Ø10 mm. The applied load was 3000 kg. The load was held for 20 seconds. The diameter of the indentation was measured visually with the aid of a measuring rod.

Sample	Hardness Brinell [HB]
A1	321
A2	353
A5	353
A10	353
A20	353
A1T	302
A2T	302
A5T	302
A10T	302
A20T	302
H1	353
H2	353
H5	341
H10	341
H20	341
H1T	302
H2T	302
H5T	302
H10T	302
H20T	302

The samples show consistent HV values, except for sample A1. This anomaly is believed to be a combination of (a) measurement error and (b) uncertainty due to only a single applied indentation. A larger number of indentations would possibly yield more consistent data. However, the size of the indentation VS. the specimen sample made this impossible.

Appendix H – Schematics of test piece preparation